University of Mississippi

eGrove

2016

Multi-Scale Nanoindentation For Characterization Of Oil Shales

Zachary N. Miller
University of Mississippi

Follow this and additional works at: https://egrove.olemiss.edu/etd

Part of the Nanotechnology Commons

MULTI-SCALE NANOINDENTATION FOR CHARACTERIZATION OF OIL SHALES

A Thesis
presented in partial fulfillment of requirements
for the degree of Master of Science in Engineering Science
The University of Mississippi

by
Zachary Miller
May 2016

ABSTRACT

Studies of the effects of polishing techniques, scale of nanoindentation, and petrophysical

properties were conducted on both Woodford and Tuscaloosa Marine Shale. Polishing

procedures include both an in-house developed, mechanical sample preparation protocol as well

as ion beam milling. The elastic modulus and hardness of each mechanically polished sample

was found to have larger value than those that were ion-milled. Additionally, at low loads, the

samples resulted in having high standard deviation. This high deviation was found to be

significantly reduced by testing at higher loads. The variations in results between mechanically

polished and ion beam milled samples is believed to occur due to a higher "peel-out" rate during

mechanical polishing that is not a significant factor within the ion beam milling procedure. The

level of polishing was analyzed in order to determine the effect of surface roughness on

indentation results within both a standard nanoindentation practice as well as atomic force

microscope indentation. Nanoindentation tests were conducted on six Woodford Shale samples

(each cut from a single core), as well as thirty Tuscaloosa Marine Shale samples (retrieved from

drilling mud). For the Woodford Shale, an average of twenty-five indentations was considered.

Likewise, for the Tuscaloosa Marine Shale, eighty indentation tests were completed for each

sample depth for an end result of 1,200 indentation tests for determining average mechanical

properties of the shale play as a whole. In both cases, maximum loads of 350 mN were used in

order to negate deviations due to heterogeneity and obtain average mechanical properties of the

samples. Thermogravimetric analysis (TGA) is used to correlate mechanical properties to the amount of total organic content as well as composition and shale maturity. For both shale plays, decomposition of light and heavy fractions occurs in the range of 200-300 °C and 420-520 °C respectively. By this process of analyses, it is determined that nanoindentation and atomic force microscopy technologies can be successfully used in the determination of mechanical properties for both core plug samples and drill cuttings alike.

DEDICATION

To my family, friends, and colleagues for whom without, completion of this work would have

never been possible.

NOMENCLATURE

NIRG = Nano Infrastructure Research Group

TMS = Tuscaloosa Marine Shale

TOC = Total Organic Carbon (%wt, unless noted otherwise)

TGA = Thermal Gravimetric Analysis

XRD = X-Ray Diffraction

TEM = Tunneling Electron Microscope

SEM = Scanning Electron Microscope

ϕ = Porosity (%)

E = Young's Modulus (GPa)

E_i = Young's Modulus of Indenter Tip (GPa)

H = Hardness (GPa)

S = Elastic Contact Stiffness or Unloading Stiffness (dependent of use)

Φ = Half-included Angle of Indenter Tip (degrees)

ν = Poisson's Ratio of Material

ν_i = Poisson's Ratio of Indenter Tip

SPM = Scanning Probe Microscope

TABLE OF CONTENTS

LIST OF TABLES

LIST OF FIGURES

CHAPTER 1: INTRODUCTION

1.1 Synopsis

To best capture the aggregate of this research, this document has been divided into four chapters. Chapter 1 provides the reader an introduction to the Tuscaloosa Marine and Woodford oil shale reservoirs, as well as the need for the research presented herein. It also reviews the theory necessary to understand nanoindentation practices, shale characteristics and how the two affect one another. Chapter 2 encapsulates all experimental processes used in characterizing the aforementioned shale specimens. Chapter 3 gives summary to relevant results obtained through the processes discussed in Chapter 2. In closing, Chapter 4 contains all concluding remarks pertinent to this research.

1.2 Theoretical Background and Literature Review

1.2.1 Oil Shale

1.2.1.1 Shale Characterization

Shale has been estimated to be the most common of sedimentary rock formations as they form roughly fifty percent of all sedimentary rocks on Earth (Bennett, Berla, Nix, & Borja, 2015; Sayers, 2012). Shale is typically known as rock formation composed of fine grained, mud-sized, siliclastic particles most commonly associated with silts and clays. Although general classification of shale is based on particle size instead of composition, it is typically separated into categories which allows for better classifications. Commonly, the term shale itself is used to

refer only to fissile rock formations composed primarily of mud-sized particles while mudstone entails non-fissle formations of the same mud-sized particles. Siltstone is also a common reference within the mudstone group and is used to define the non-fissle formations with mud-sized particles; however, they are found to have low clay fractions (Mavko, 2013).

Due to the variety of shale formations, the percentages of any given shales' components fall within a wide range and can vary sample to sample. These components are most often categorized into hard materials (i.e. quartz, feldspar, pyrite) (Bennett, Berla, Nix, & Borja, 2015), intermediately hard materials (i.e. calcite), and soft materials (i.e. silts and clays).

1.2.1.2 Total Organic Carbon

What has made shale exploration such an advantageous study is that shales contain varying amounts of organic materials which can be harvested as hydrocarbon. Through a process of diagenesis (Dow, 2011), kerogen is formed. According to Dow (2011), oil source rocks generate approximately 60 bbls per acre foot for each one percent of TOC contained. Because expulsion efficiencies are typically low, the majority of this content stays trapped within the source rock in turn making it an attractive and mature, unconventional oil and gas reservoir. TOC is generally used in determining the potential of source rocks for the generation of hydrocarbon. The main component of the organic compounds found within shales is the convertible carbon present in kerogen which can be successfully converted into hydrocarbons when temperature and pressure stresses are applied. Previous studies have been conducted on shales (other than Tuscaloosa Marine Shale) through analyses such as TGA and XRD. The results are shown in Table 1 and 2.

Table 1: Average TOC and clay contents of Woodford shale as determined by ARMA (Aoudia, Miskimins, Harris, & Mnich, 2010).

Woodford Zone	Core Depth (ft)	TOC (wt%)	Clay Content (wt%)
Upper	12759.75-12786.75	3.8	6.33
Middle	12786.75-12980.40	5.4	13.27
Lower	12980.40-13038.68	4.6	28
	13038.68-13097.98	2.9	4.4

Table 2: Various shale TOC and Mineralogy (Kumar, Sondergeld, & Rai, 2015).

Formation name	No. of samples	TOC (wt%)	Mineralogy description	Reference
Woodford	70	0.5–13	Clay, quartz, carbonate	Gupta (2012)
Barnett	37	0.6–7	Clay, quartz, carbonate	Kale (2009)
Haynesville	16	0.4–8	Clay, carbonate	Kumar (2012)
Eagle Ford	13	0.4–5	Carbonate, clay	Sondhi (2011)
Kimmeridge	5	1–55	Carbonate, clay	Sarkar (2008)
Ordovician	3	—	Carbonate, clay	Kumar (2012)

1.2.1.3 Woodford and Tuscaloosa Marine Shale Reservoirs

Woodford shale is very rich in clay and quartz compositions and has been found to have a total organic carbon (TOC) content of 0.5 to 13 percent by weight and a porosity, ϕ, ranging from 2 to 7 percent by volume (Kumar, Sondergeld, & Rai, 2015). According to the State of Louisiana Department of Natural Resources (Louisiana Department of Natural Resources, 2016), Tuscaloosa Marine Shale is one of the oldest shale plays next to the Eagle Ford play in Texas. Though much research has been done with the majority of the shale plays listed previously (as discussed in Chapter 2), Tuscaloosa Marine Shale has just began to peak interests as preliminary

evaluations show it may contain a potential reserve of about seven billion barrels of oil (John, Jones, Moncrief, Bourgeoiss, & Harder).

Figure 1 shows the locations of each shale play located in the United States. Not included in the identification of shale play locations is Tuscaloosa Marine shale. Figure 2 shows a generalized region of focus for Tuscaloosa Marine shale.
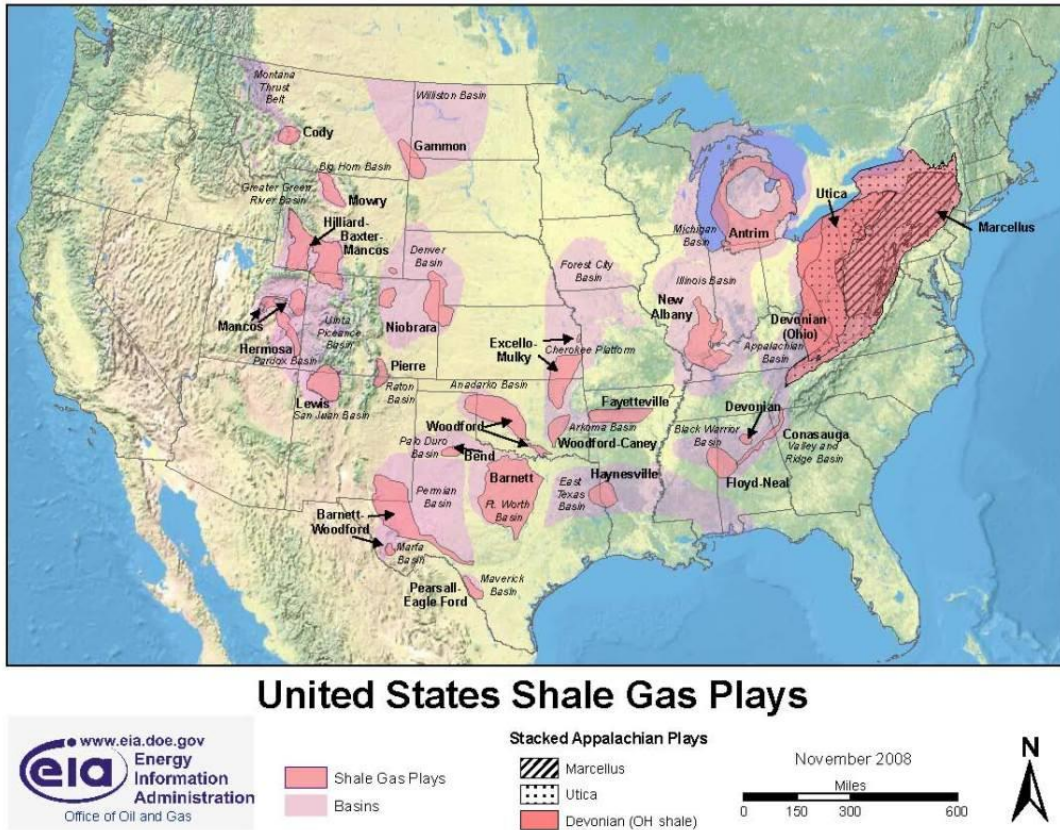
Figure 1: United States shale play locations. Note Woodford shale locations (Oklahoma and SW Texas). Also note that TMS has not been labeled in this figure (Oil & Natural Gas Field, 2014).
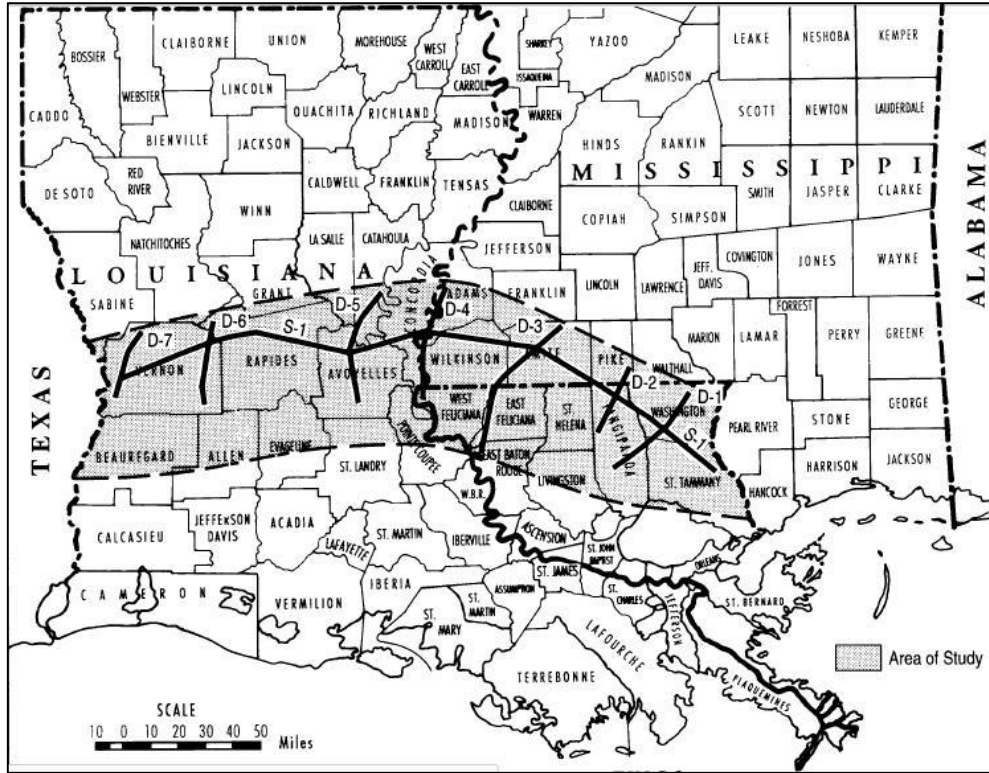
Figure 2: Generalized location of Tuscaloosa Marine Shale play in central Louisiana (Florida parishes) and Southwest Mississippi counties (Tuscaloosa Marine Shale (TMS)).

1.2.2 Nanoindentation Theory

1.2.2.1 Indentation Methodology

Throughout the past few decades, researchers have been consistently delving deeper and deeper into sub-micro and nano-scale testing methods to further understand material properties and behaviors. Such interests lie in the determination of a materials' elastic modulus, hardness, strain-hardening, cracking, phase transformations, creep and relaxation effects, fracture toughness and energy absorption to name a few (Fischer-Cripps, 2004; Ramirez, 2010). Among these properties, nanoindentation testing (NIT) is most commonly used in order to determine the elastic modulus, E, and hardness, H. This is done through the process of controlling and actively monitoring loads and displacements of an indentation tip, of known geometry and composition,

5

as it penetrates a material of unknown properties with high resolution electronic equipment. The aforementioned properties can then be found through functions of the tip geometry and residual impressions during (Hay, 2009) and also after the indentation process is complete. These functions will be further defined and discussed in Section 1.2.2.2.

Nanoindentation testing has gained significant attention for the testing of homogeneous materials such as metals, ceramics, some polymeric and even biological materials (Fischer-Cripps, 2004; Schuh, 2006; Hay, 2009). Such attention has been given to this method of testing as it is a non-destructive test operated at low force (typ. mN) ranges and depth penetrations in the order of microns with resolutions of a few nanonewtons and less than a nanometer respectively. Sample sizes also impact the significance of testing as nanoindentation requires only a very small sample volume whereas conventional testing of mechanical properties require large sample quantities which often is not possible. It is for this reason that nanoindentation of oil shale is a great topic of interest and the main focus of this research.

Throughout this research the main focus of indentation practices is to successfully quantify the elastic modulus and hardness of the Tuscaloosa Marine Shale through the analysis of load-displacement curves. Elastic modulus, also called Young's modulus, in general is a measure of elasticity of a material which is equal to the ratio of the stress applied on the material to the resulting strain (Hay, 2009); or mathematically expressed as:

$$E = \frac{\sigma}{\varepsilon} = \frac{stress}{strain} \quad . \tag{1.1}$$

Likewise, hardness is a very important and highly sought after value during indentation testing and can be described as the resistance to deformation of a material under stress as is typically expressed as:

$$H = \frac{P}{A_c} = \frac{Applied\ Load}{Contact\ Area} \quad . \tag{1.2}$$

As previously mentioned, nanoindentation has become a highly popular technique for acquiring these properties as it only requires testing small specimens at very low loads and displacements whereas more conventional hardness testing requires testing large specimens at high loads. Typically to determine these properties a tip sized in the order of microns (typically Berkovich is preferred) is used to penetrate the specimen allowing for the measurements of maximum depth of penetration as well as residual impression in the material. However, these values are not directly obtained from the indent itself; but is calculated through means of measuring the elastic contact stiffness, S, as explained in Section 1.2.2.2. It should be noted that Section 1.2.2.2 will give a detailed summary of the Oliver and Pharr method; however, for a deeper understanding the reader should review Oliver and Pharr's 1992 and 2004 publications (Oliver & Pharr, 2004) as well as many other publications that discuss how the method has been broadly applied to studies lying outside of this research's primary focus area (Hay, 2009; 2013; Hay & Sondergeld, 2010; Jauberteau, Nadal, & Jaubertau, 2008; CSM Instruments, 2007). Nanoindentation is a type of hardness testing that falls within the micro hardness category and differs from macro hardness testing such as Brinell and Mohr's test where residual impression areas must be imaged in order to determine the contact area which is in turn used to obtain hardness and moduli values. Though both methods tend to only have negligible differences, highly elastic materials should be considered for nanoindentation procedures as they will leave very small residual impressions in comparison to the deflected area under the load.

1.2.2.2 Oliver and Pharr Method

The initial idea of a new method for obtaining mechanical properties on a nano-to-micro scale came about when Oliver and Pharr devised a method which provided a way to know the size of a hardness indentation without having to image the residual impression after the

indentation process itself (Hay, 2013). This "landmark" (Hay, 2009) method is primarily an

indentation test which consists of applying an increasing load onto the surface of a material until

reaching a desired, user input, load value and then the withdrawal of the indenter from the

material (Figure 4). It is important to note that through this method, the referenced indenter tip is

a Berkovich diamond tip. The Berkovich tip is a three sided pyramidal indenter as can be seen in

Figure 3 below.
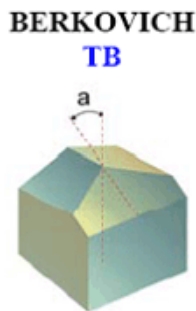
Figure 3: Typical Berkovich indenter tip geometry (Micro Star Technologies).

The Berkovich indenter tip is commonly chosen for a wide variety of reasons (i.e. well

known mechanical properties, durable, easily manufactured with negligible flaws, etc.), however

it's capability to induce both elastic and plastic reactions within a single analysis under very

small loads makes it favorable. Because of this capability, Oliver and Pharr were able to capture

these reactions through geometric functions. It is important, though, to note that this method

assumes only elastic displacements are recovered during unloading (Oliver & Pharr, 2004; Hay,

2009; 2013; Jauberteau, Nadal, & Jaubertau, 2008) as shown in Figure 4. It is for this reason the

method presented by Oliver and Pharr is not applicable to materials which demonstrate reverse

plasticity during the unloading phases. However, through finite element analysis it has been

proven that in almost all cases, reverse plastic deformations are negligible (Oliver & Pharr, 2004).
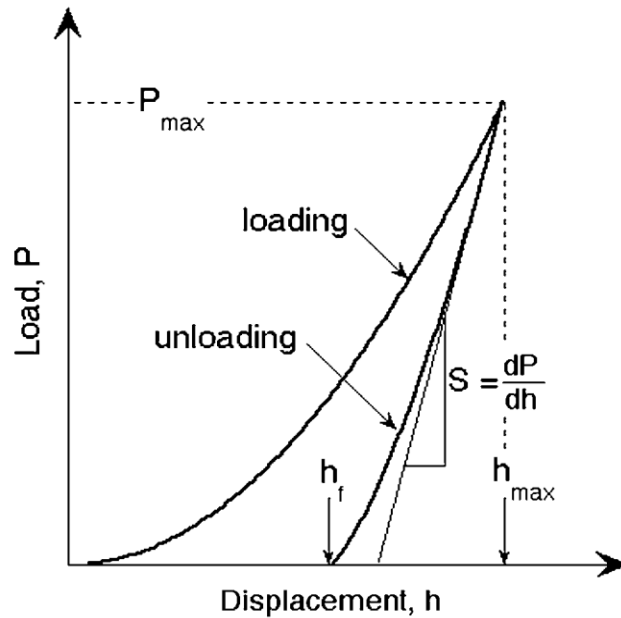
Figure 4: Typical load-displacement curve obtained during load application and after retraction. Shows critical parameters of contact geometry used in calculation of desired values (Oliver & Pharr, 2004).

The Oliver and Pharr method follows a series of steps in the determination of a materials' mechanical properties. The first phase of analysis begins with the physical indenting of a material as illustrated in Figure 5, in order to obtain load-displacement curves as previously discussed and depicted in Figure 4.
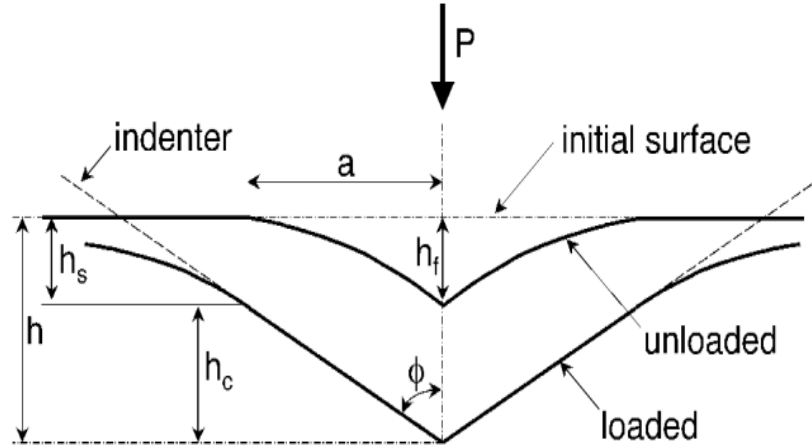
Figure 5: Profile view of indenter tip during load application and after retraction. Shows critical parameters of contact geometry used in calculation of desired values (Oliver & Pharr, 2004).

Once a load-displacement curve has been obtained, approximation of the unloading curves by the power law relation:

$$P = \alpha(h - h_f)^m \qquad (1.3)$$

where P is the applied load, α and m are power fitting constants, and h and h_f are the resulting maximum and residual displacements respectively. Table 3 shows typical values of the power fitting constants for a variety of materials as found through use of the Berkovich indenter.

Table 3: Values of power fitting constants as determined through experiments with the Berkovich indenter (Oliver & Pharr, 2004).

Material	α (mN/nm^m)	m	Correlation coefficient, R
Aluminum	0.265	1.38	0.999938
Soda-lime glass	0.0279	1.37	0.999997
Sapphire	0.0435	1.47	0.999998
Fused silica	0.0500	1.25	0.999997
Tungsten	0.141	1.51	0.999986
Silica	0.0215	1.43	0.999985

This is an improved approximation method over the one Doerner and Nix (1986) created as when using a flat punch, the contact area remains the same throughout the withdrawal of the indenter which causes the unloading curve to become linear. Though this proved Oliver and Pharr's method to be more efficient, it also led to the assumption that the behavior of Berkovich indeneters can sufficiently be modeled as a conical indenter with a half-included angle, Φ, which results in comparable depth-to-area relationships noted as $\Phi = 70.3°$ (Fischer-Cripps, 2004; Oliver & Pharr, 2004). Next, equation (1.3) can be analytically differentiated to determine the elastic contact stiffness resulting as:

$$S = \left.\frac{dP}{dh}\right|_{h=h_{max}} = \alpha m (h_{maz} - h_f)^{m-1} \tag{1.4}$$

One assumption made by Oliver and Pharr is that pile-up of materials around the contact periphery is negligible. However, the effect of pile up using AFM imaging techniques in comparison to the results obtained through the nanoindentation process has been studied (Jauberteau, Nadal, & Jaubertau, 2008) and show that the Oliver and Pharr method of determining elastic modulus and hardness should be used with caution. With that said, Oliver and Pharr did account for a sink-in factor, h_s, given by the equation:

$$h_s = \varepsilon \frac{P_{max}}{S} \tag{1.5}$$

and displayed in Figure 5. Where ε is a constant directly related to the geometry of the indenter being used. For Berkovich indenter, $\varepsilon = 0.75$ (Oliver & Pharr, 2004). Additionally, the remaining depth along which contact is made between indenter and specimen h_c, is expressed as:

$$h_c = h_{max} - \varepsilon \frac{P_{max}}{S} \tag{1.6}$$

Once displacement depths are calculated, an empirically calculated area function relating the projected area of the indenter to the contact depth as

$$A = f(h_c) \tag{1.7}$$

can be formed. This area function, which is also commonly referred to as the indenter shape

function, should always be calibrated as to compensate for any imperfections in the indenters

geometry. The most common of these imperfections is that of a certain rounding that inevitably

occurs during the grinding process. Table 4 shows the variations of standard area functions used

for their corresponding tip types.

Table 4: Area functions for various indenter geometries (Hay, 2009; Jauberteau, Nadal, &

Jaubertau, 2008).

TIP TYPE	AREA FUNCTION	COMMENTS
Ideal Berkovich	$A = 24.56 h_c^2$	Used when $h_c > 2$ microns
Real Berkovich	$A = 24.56 h_c^2 + C h_c$	C is determined by indenting a known material and is about 150 nm.
Real cube-corner	$A = 2.60 h_c^2 + C h_c$	C is determined by indenting a known material and is about 150 nm.
Sphere	$A = 2\pi R h_c$	R is tip radius; value may be known or determined by indenting a known material.
Cone	$A = \pi \tan^2 \psi h_c^2$	ψ is the half-included angle of the cone as illustrated in Fig. 1.
Sphere-tipped cone	$A = \pi \tan^2 \psi h_c^2 + 2\pi R h_c$	Superposition of the area functions for a sphere and a cone.
Flat-ended cylinder	$A = \pi a^2$	A is the punch radius; A is constant (independent of indentation depth).

From materials theory, once the contact area is established the hardness of the material can be

determined by:

$$H = \frac{P_{max}}{A_c}. \tag{1.8}$$

Lastly, measurement of elastic modulus is found from the relationship to contact area and the

measured unloading stiffness (Fischer-Cripps, 2004; Oliver & Pharr, 2004; Hay, 2009;

Jauberteau, Nadal, & Jaubertau, 2008; Zeszotarski, et al., 2004) through the equation:

$$S = \beta \frac{2}{\sqrt{\pi}} E_{eff} \sqrt{A}$$
(1.9)

where E_{eff} is noted as the effective elastic modulus and is defined as (Fischer-Cripps, 2004;

Oliver & Pharr, 2004; Hay, 2009; Jauberteau, Nadal, & Jaubertau, 2008; Doerner & Nix, 1986;

Zeszotarski, et al., 2004):

$$\frac{1}{E_{eff}} = \frac{1-v^2}{E} + \frac{1-v_i^2}{E_i} \quad .$$
(1.10)

Effective elastic modulus is considered as it allows for elastic displacements to occur in both the

sample, E and v, and the indenter, E_i and v_i. Most materials show less than ten percent

difference in elastic moduli by varying the range of Poisson's ratio values from 0.1-0.4; therefor,

using of Poisson's ratio in equation (1.10) to solve for elastic modulus is acceptable. Figure 6

displays this relation for a randomly selected, Tuscaloosa Marine Shale sample.
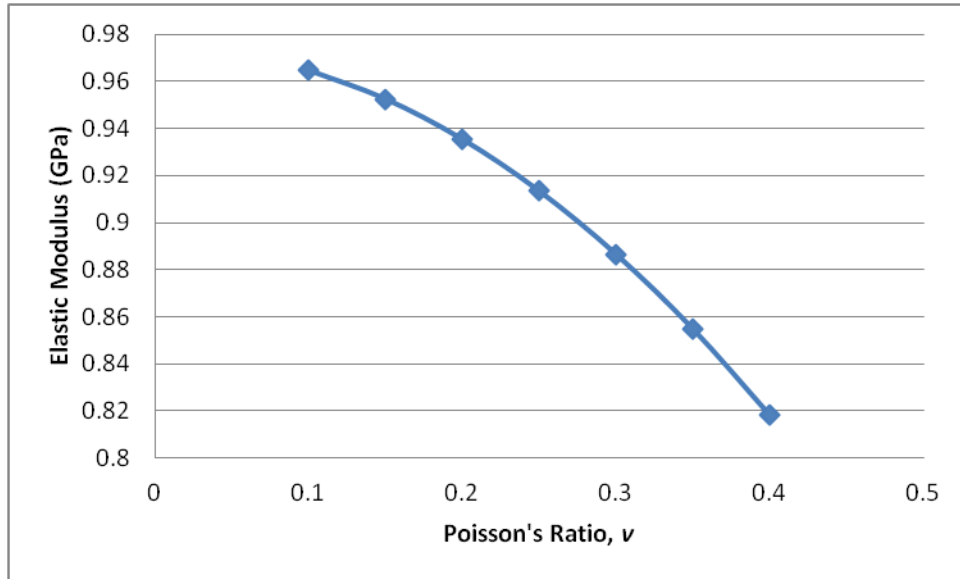
Figure 6: Comparison of variation in elastic modulus, E, with change in Poisson's ratio, ν, for

TMS sample.

1.2.3 Previous Research

1.2.3.1 Mechanical Properties of Shale Composition Using Nanoindentation

Because of the success from shale-gas development within the intercontinental U.S.

(Aoudia, Miskimins, Harris, & Mnich, 2010), improvements to the fracking process is under

constant review. This is because successful retrieval of shale materials is based primarily on the

designs of horizontal drilling and hydraulic fracturing. But, in order to optimize these design

phases, proper understanding of shale mechanical properties is needed. In order to gain insight

of these properties in attempt to maximize the fracking potential and reduce expended resourses,

multiple indentation and imaging techniques have been employed to a wide variety of shale

formations (Kumar, Sondergeld, & Rai, 2015; Aoudia, Miskimins, Harris, & Mnich, 2010;

Bennett, Berla, Nix, & Borja, 2015; Mavko, 2013; Zeszotarski, et al., 2004). Using an AFM-

nanoindentation technique based on the Oliver and Pharr method, Zeoszotarky (2004) was able

to distinguish and test kerogen alone within the Woodford shale. In order to fully understand the effect on the mechanical properties, testing was performed both homologous and orthogonally to the bedding planes which resulted in values as shown in Table 5.

Table 5: Indentation results for hardenss and indentation modulus of kerogen found in Woodford shale (Zeszotarski, et al., 2004).

	No. of Indents	Hardness (GPa)	Indentation Modulus $(GPa/(1-v^2))$
Sample 1 Indentation Perpendicular to Bedding Plane	40	0.57 ± 0.03	10.5 ± 0.7
Sample 2 Indentation Parallel to Bedding Plane	29	0.55 ± 0.02	10.5 ± 1.0
Sample 3 Indentation Parallel to Bedding Plane	49	0.56 ± 0.03	11.1 ± 0.6

Combining these values from indentation with atomic force microscope imaging techniques, division of material phases became possible as hard mineral, soft mineral and kerogen phases represented by hardness values of H>6, 1<H>6, and H<1 respectively (Zeszotarski, et al., 2004). When further evaluated, similar procedures (Aoudia, Miskimins, Harris, & Mnich, 2010) found the relationship of Young's modulus to major contributing components of shale as:

$$E= -613337(TOC)- 58989(Illite)+ 217593(Apatite)+ 2235605(Calcite)- 146070(Magnesite) \qquad (2.11)$$

where E is calculated in psi and mineral contents are in percent weight. Although there were no significant coefficients of determination (R^2), trends in the data sets were found to be quite insightful as will be seen in Chapter 3.

1.3 Need for Research

There has been much success in recent years within the field of hydrocarbon exploitation of shale plays such as Barnett, Bakken, Haynesville, Woodford, Eagle Ford Shales, etc., throughout North America (Kumar, Sondergeld, & Rai, 2015; Aoudia, Miskimins, Harris, & Mnich, 2010). Due to this success, drilling and production companies are consistently searching for ways to improve the process of determining, drilling, and processing successful wells within each of these shale play areas. Through this research, mechanical properties of Woodford and Tuscaloosa Marine Shales (with primary focus on TMS) can be related to initial and cumulative production, as well as well log data to determine trends within the shale play's properties and behaviors. This, however, requires tedious procedures that are financially significant such as hydraulic fracturing. Within hydraulic fracturing, there are many precautions and procedures to take into consideration when extracting shale. One key area that quite heavily affects the design and analysis phases of the 'fracking' process that is not heavily addressed in depth in literature, is the influence of the mineral composition and TOC of each type of shale on the specimen's mechanical properties as well as how said mechanical properties, in time, effect the hydraulic fracture growth process (Aoudia, Miskimins, Harris, & Mnich, 2010). Very little has been done for the characterization of Tuscaloosa Marine Shale in comparison to other shale plays which is why following issues need to be investigated.

- Determination of how the orientation of the bedding plane with respect to the direction of indentation affects results.
- Analyze the level of polishing effects upon nanoindentation results.
- Relate the properties obtained from testing drill cuttings to testing of core plug samples.
- Analyze whether nanoindentation testing can produce viable results for mechanical

properties through the testing of drill-cuttings.

- Correlate mechanical properties obtained through nanoindentation testing directly to the amount of kerogen within a specimen.

- Study whether a shale's mineral composition affects the mechanical properties obtained.

- Establish a link between the size and scale of testing and determine the effects on results.

1.4 Objectives

The overall objective of this study is to statistically evaluate factors that affect mechanical properties of Tuscaloosa Marine Shale obtained through indentation techniques and to correlate that to its nanostructure. More specifically this study focuses on

1. Correlating oil shale mineralogy and organic content to mechanical properties (e.g. hardness and modulus),

2. Correlating surface morphology to measured mechanical properties,

3. Studying effect of bedding plane orientations, with respect to the direction of indentation, on abtained results, and

4. Establishing a link between the size/ scale of testing regions on measured local properties (e.g. local to global correlation).

CHAPTER 2: EXPERIMENTAL PROBLEM

2.1 Nanoindentation

2.1.1 Importance of Sample Preparation

Sample preparation is the first step to analyzing mechanical properties of shale materials and is very important to ensure the quality of testing results. As mentioned in Section 1.2.2, hardness and modulus values are derived from the contact area between the indenter and the sample. The values derived through the analysis is based on the assumption that the surface is flat, when in reality, obtaining a perfectly flat surface can be quite the challenge itself. For this reason, the surface roughness plays a major part in the validation of testing results. However, the importance of surface roughness has an inverse relationship with increased loading. Figure 7 shows two separate scenarios of indenting a sample of normalized roughness.
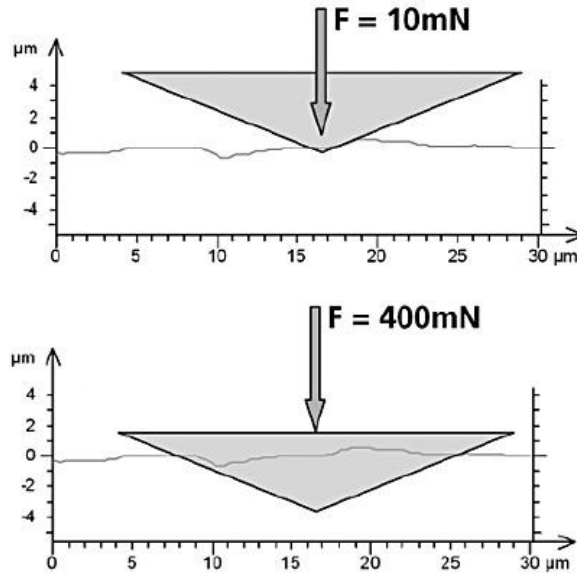
Figure 7: Generalized profile of specimen with rough surface and representation of indenter for load controlled tests of 10 mN and 400 mN maximum loads (CSM Instruments, 2007).

In the case of the 10mN max load, it is quite clear that the samples surface roughness cannot be ignored as the residual impression left within the surface will not bare accurate results. The case of the 400mN max load illustrates that because the residual impression will be comparatively significant to that of a low load, the surface roughness can be considered as 'flat', appeasing the Oliver and Pharr method as well as ASTM Standard E2546 (Ramirez, 2010). Use of very low load forces as in the first scenario is typically sought after when ion-milling of samples is performed to obtain a near-perfectly flat surface, in order to test the components of shale (i.e. quartz, clay, kerogen, etc.) individually. When using higher loads during testing such as the second scenario, hardness values covering many components can give average hardness values of the sample close to the macro scale. Sample preparation procedures can vary quite drastically from formation to formation as the quality of polishing differs dependent of the specimen's composition. Because of shale's heterogeneous nature, prior exploration of the formation in raw form can help to determine the level of polishing required. This is so as harder

20

phases can be polished very easily whereas intermediate and soft phases will often have scratches and even peel-out during the stages of fine polishing. Again, this will directly affect the hardness and modulus values obtained during testing and can be checked for significant impact through the analysis of standard deviations for each respective property.

2.1.2 Sample Polishing Procedure

The Tuscaloosa Shale chips being studied were collected from drill cuttings and are not large enough to be cut and handled solely. To alleviate this issue, a special epoxy resin system was used to encapsulate individual chips as seen in Figure 8.

Figure 8: Chips of Tuscaloosa Marine Shale encapsulated in epoxy.

This epoxy system (epoxy set resin #145-2005, hardener #145-20010, 100:12 mixing ratio by weight) was purchased from Allied High Tech Products INC. The epoxy system used is ideal as it cures at room temperature, reducing any negative effects on the shale as it is heat sensitive. During polishing, the sample is placed in a stainless steel jig (Figure 9) so that the top surface, or face, of the sample is in contact with the emery paper attached to the lapping wheel.

Figure 9: Polishing jig used to mechanically polish the specimen.

The inner cylinder of the jig is free to move vertically between user set depths allowing the user to control the amount of material removal during polishing. The following polishing procedure as recommended by Paul Allison of ERDC has been slightly modified to account for shale polishing.

1. Use Ethylene glycol, Ethanol (50:50) by weight as lapping lubricant.

2. Grind – use 240 silicon carbide grit paper (52.0 micron particle size) until Sharpie line is removed

3. Flush the surface with ethanol in a squeeze

4. Grind – use 600 silicon carbide grit paper (15.0 micron particle size)

5. Flush the surface with ethanol in a squeeze

6. Grind – use silicon carbide 1200 grit paper (5.0 micron particle size)

7. Flush the surface with ethanol in a squeeze

8. Grind – use aluminum oxide paper (3.0 micron particle size)

9. Flush the surface with ethanol in a squeeze

10. Grind – use aluminum oxide paper (1.0 micron particle size)

11. Flush the surface with ethanol in a squeeze

12. Grind – use aluminum oxide paper (0.3 micron particle size)

13. Flush the surface with ethanol in a squeeze

Through analysis of polishing procedures (detailed in Section 3.3) comparable to surface roughness for both Tuscaloosa Marine and Woodford shale; it was determined that heavily polishing the Tuscaloosa Marine Shale induced significant damage as well as caused a peel-out effect of soft materials for both shale types. This was proven true even for specimens which underwent both TEM (Tunneling Electron Microscope) and SEM (Scanning Electron Microscope) ion-milling processes. For this reason, only steps 1-3 in the previous polishing procedure has been followed as to allow for the retaining of softer and possibly organic materials found within the specimen. Additionally, it is for this reason nanoindentation was performed at a relatively high load rate as detailed in Section 2.1.6.

2.1.3 Description of Equipment

Nanoindentation analysis is performed on a Nanovea M1 Hardness Tester with an optical microscope add on. The equipment can be seen in Figure 10-12.

Figure 10: Nanovea M1 Hardness Tester with microscope, full set-up. Equipment is located

within an isolation cabinet for the reduction of background noise. The cabinet is attached to the

frame of an anti-vibration (air stayed) table which dampens any vibrations present within the

interior or exterior of the cabinet itself.
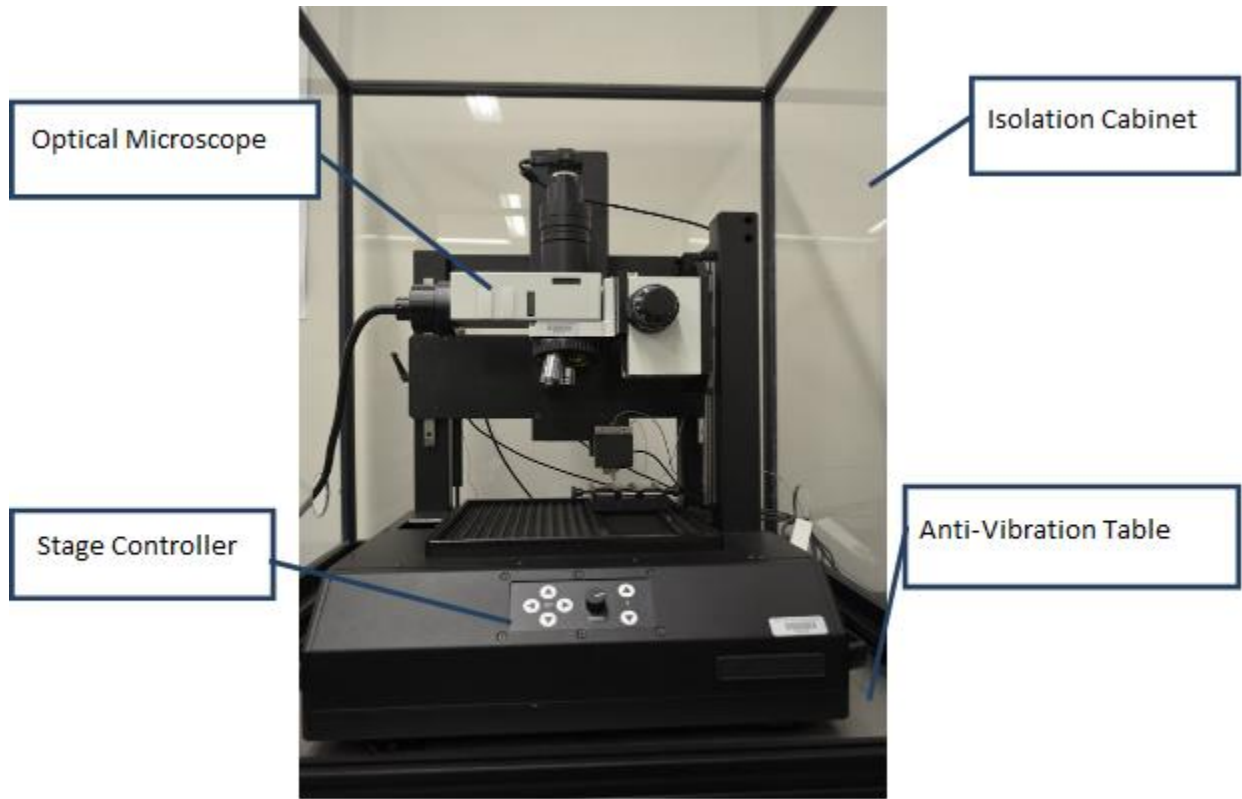
Figure 11: Close up view of Nanovea M1 Hardness Tester with microscope set up.
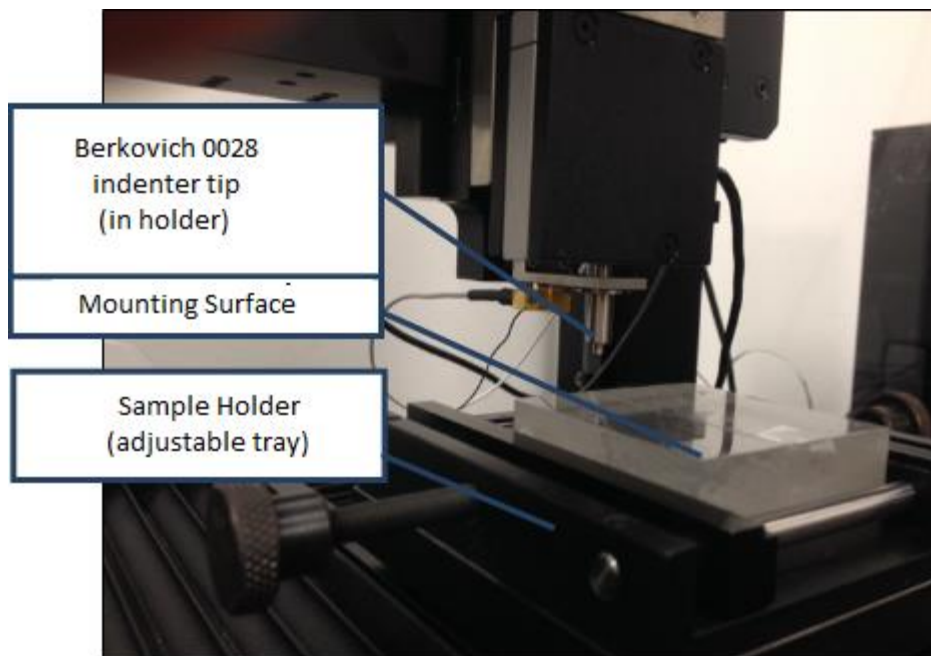
Figure 12: Close-up view of Nanovea M1 Hardness Tester indenter tip and sample holder.

Out of view in Figure 10 and Figure 11 is the light-box (left) which provides the light

source to the optical microscope, power systems and station computer (right) for controlling the

indenter and data acquisition during testing. In order to determine the desired testing location

among the surface of a specimen, the optical microscope is used through a feature of the

Nanovea Hardness Tester software v1.6.1. In order to accurately indent the locale desired, the

automated 150 mm XY motorized table should be checked for calibration.

Based on the theory set forth by Doerner and Nix (1986), force is applied onto the

indenter by passing a measured current through a coil wrapped against a circular magnet. The

applied force is then determined as it is indirectly proportional to the current passed through the

coil. To determine the displacement, a sensing system consisting of three circular capacitor

plates are arranged as can be seen in Figure 13.
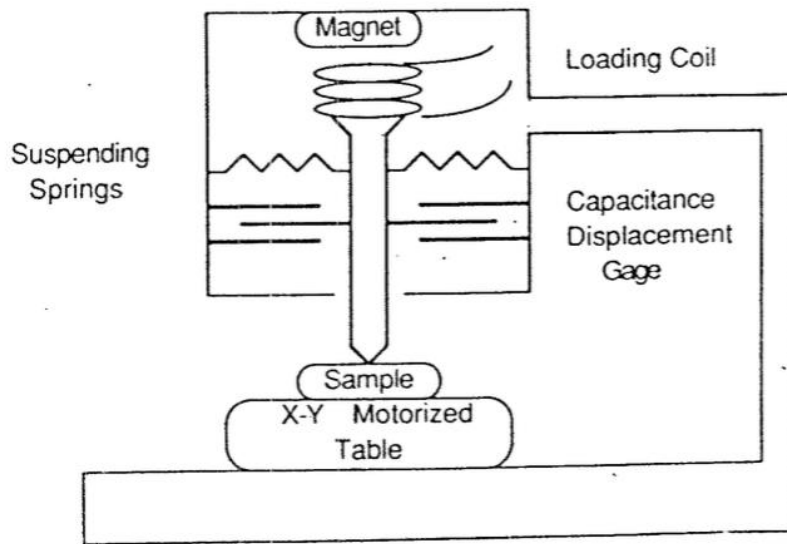
Figure 13: Typical nanoindenter schematic (Doerner & Nix, 1986).

As can be seen, the middle of the three plates is physically attached to the indenter shaft and can

move freely between the top and bottom plates. From this, the displacement of the indenter shaft

is determined by the change in voltage between middle and outside plates. This system is supported by the two suspending springs, which can be located directly above the capacitor plates, which have very high and low horizontal and vertical stiffness respectively.

2.1.4 Source of Error

A main cause of error outside of improper calibration comes primarily from vibrations, both acoustic and mechanical. To avoid these errors, the testing system should be placed in a quiet, solid foundation environment and mounted on a vibration-isolation system (Hay, 2009). In order to adhere to this, the University of Mississippi Nano Infrastructure Research Group has isolated the indenter (Figure 10) into secluded room with both an isolation cabinet and an air-stayed, anti-vibration table. Thermal drift can also play role in errors during indentation and can be corrected by analyzing the hold period (creep measurement) in the load-displacement curve. While thermal drift is something that should always be considered, corrections are generally miniscule and can be omitted if very low impact of thermal drift is expected relative to the overall penetration (Hay, 2009). Generally, in an environment controlled setting (such as the one used during this research) thermal drift does not make any significant impact as long as tests are performed shortly after enclosing the equipment. Extensive studies have been performed to determine the effect of thermal drift on computed elastic modulus values and was determined that if t_h in

$$t_h = \frac{S}{|\dot{P}|}h_c \tag{3.1}$$

is the total time taken from beginning of any given test to the beginning of the unloading curve, it is shown that the thermal drift has minimum effect on the computation of elastic modulus and can be considered negligible in most cases (Fischer-Cripps, 2004; Hay, 2009). Where S is the contact stiffness and $\dot{P}$ is the unloading rate.

2.1.5 Equipment Calibration

Whenever changing indenter tips, it is important that the user performs a stage calibration. This is done by creating a pattern of indents on a clearly visible surface (metals are preferred and comes with most equipment) and aligning the transition between optical microscope and indents repeatedly until a center-to-center alignment is acquired. To calibrate the equipment's compliance and depth sensors, multiple indents on fused-silica are made. It is generally good practice to make at least five indents before running the calibration process. This process is done prior to all testing of shale materials to ensure accuracy during testing. Further testing of materials with known values (i.e. brass, copper, aluminum, etc.) can be carried out and compared to literature if needed. Published elastic modulus values of some materials are shown in the following Table 6.

Table 6: Measured nanoindentation Young's modulus for common materials.

Material	Literature E (GPa)	Source
Fused-Silica	74	Agilent Technologies (2009)
Copper	90-155	Simmons and Wang (1971)
Aluminum	69-75	Agilent Technologies (2009)

2.1.6 Testing Procedure

To begin, polished specimens should be dry and free of loose debris. Ideally, latex gloves are to be worn as to prevent the transfer of contaminants to the specimen. Using a glass block as a base for the specimen to sit (Figure 12), the sample is adhered to the base. When the bond is secure, the mounting base and sample can be inserted into the tray atop the automated table and fastened into place. Move the sample under the indenter tip, leaving sufficient clearance, at

approximately center of the sample. For larger samples, one can move the indenter tip

approximately over the area of interest if known. Using the Nanovea Hardness Tester software,

transition the sample from beneath the indenter to beneath the microscope. Scan the sample's

surface for a preferred locale for indentation. Transition the sample back to underneath the

indenter tip and lower the tip until close to the samples surface. Using *auto-contact* mode, the

indenter will approach the surface at a user specified rate until a specified contact force is met.

The values used for this research are found in Table 7. Once indenter tip is just near (not in

contact with) the surface, all compliance and depth values should be zero (no force should be

acting on the tip prior to indentation). Using a load-controlled option, the indenter tip is then

displaced into the sample's surface at a specified loading rate until reaching the maximum load,

followed by an unloading rate.

Table 7: Parameters used for testing TMS and Woodford shale samples.

Sample Name	Oil Shale	
Approach Speed	2	μm/min
Contact Load	0.05	mN
Indenter	Berkovich	
Load	350	mN
Loading Rate	700	mN/min
Unloading Rate	700	mN/min

In some instances, creep measurements are necessary and will take place at maximum loading,

before unloading, for a specified amount of time. For the purposes of this analysis creep was not

monitored. Once this process is complete, the indenter tip should be free of the sample surface

and a load-displacement curve should have been generated as shown in Figure 14.
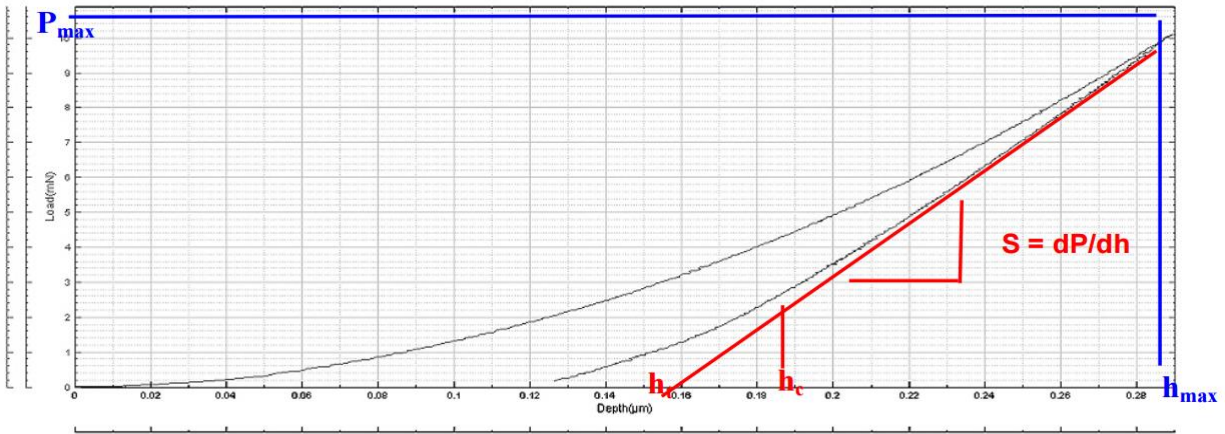
Figure 14: Typical output from Nanovea MicroHardness Tester software with overlay of variable determinations for Oliver and Pharr method of calculating E and H (Ramirez, 2010).

From the unloading curve, the hardness and elastic modulus value for each respective indent can be determined and exported for future use. This process is repeated until sufficient data is collected for the specimen. It is important to note that the distance between successive indents should be at least 10-30 times the maximum depth of indentation (Kumar, Sondergeld, & Rai, 2015; Hay, 2009). In this research, the top 40 tests were taken from two separate specimens for a combined total of 80 indentations per drilling length. This was carried out for incremental drill lengths of 500 feet ranging from 14300 to 21300 feet. Once all load-displacement curves are collected for each measured depth (depth corresponding to its' position in the drilling process) an average of the values are taken to obtain the mean value of hardness and elastic modulus corresponding to that depth. This mean value is taken to be considered representative of the shale sample as a whole. By averaging the values obtained from two separate samples corresponding to the same depth, the bias in measurements caused by different phase distributions are minimized.

2.2 Atomic Force Microscopy

2.2.1 Importance of Sample Preparation

Sample preparation for both AFM imaging and indentation is the same as completed for nanoindentation as discussed in Sections 2.1.1 and 2.1.2. However, the one exception is that for testing with the AFM, the sample must comply to height limitations associated with the AFM equipment used. Unlike analysis performed by nanoindentation, the surface roughness of a sample has greater impact on the results of AFM analysis which calls for greater attention when preparing samples. Rough surfaces can cause artifacts in the images, such as streaking which is caused by particle pullout. Also, as AFM tips are very small and meant for use on flat surfaces, rapid dulling or even breaking of the tip when testing rough surfaced samples may occur. Beneficially, though, AFM techniques only require a small surface area to be imaged or indented. This allows for smaller images and grid patterns to be applied across rough samples in order to obtain smoother images as well as indentation data with less standard deviations. However, using smaller image sizes and indentation is not always representative of the sample as a whole.

2.2.2 Description of Equipment

Atomic force microscopy is performed on a Nanoscope IIIa from Bruker Nano Inc., as seen in Figure 15. A J-scanner along with a TAP150AL-G silicon probe with an aluminum reflex coating is used to produce AFM imaging results. Additionally, an E-scanner along with a DNISP nanoindentation probe produced by Bruker Nano Inc. is used during AFM indentation analyses.
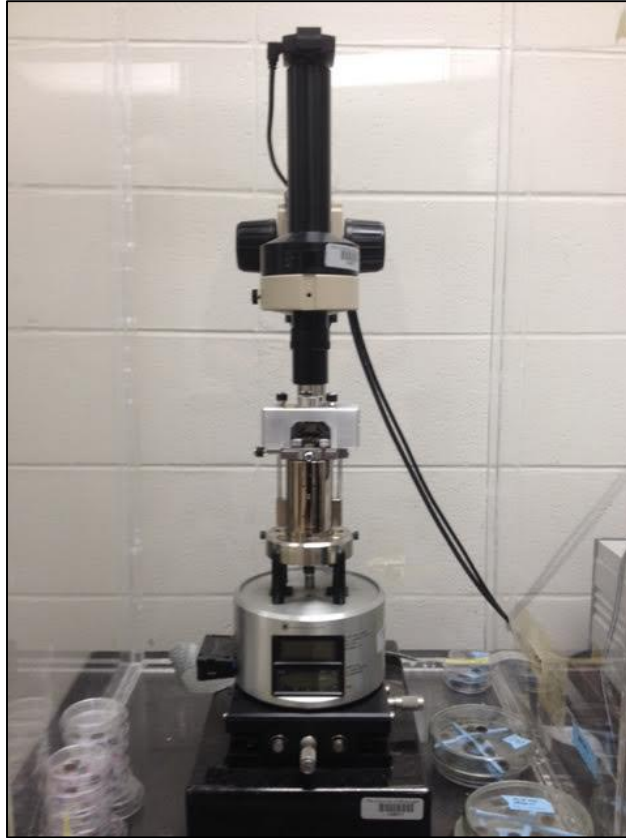
Figure 15: Nanoscope IIIa equipped with J and E scanners. Not seen in figure: compressed air tank for anti-vibration tables (left) and station computer for running programs and data acquisition (right).

2.2.3 Source of Error

With all of the same sources of error discussed in Section 2.1.4 for nanoindentation, AFM analyses are highly sensitive to an overabundance of light. With this in mind, in addition to isolating the equipment into a secluded area free of mechanical and noise vibrations, the amount of lighting should always be limited to minimal. This is typically countered by placing the equipment in an isolation cabinet which can prevent transference of light, noise, and mechanical vibrations. Additionally, like nanoindentation equipment, the AFM should be located on an anti-vibration table.

2.2.4 Equipment Calibration

To begin, the tip is first cleaned by indenting a gold calibration sample. Then by indentation of a sapphire calibration sample using the procedure outlined in the "Calibrate and Deflection Sensitivity" section of the help menu, the tip's deflection sensitivity is calibrated. Next, a trigger threshold should be set to 0.05 mV. By setting a low threshold value the force applied during indentation of the sapphire sample is controlled so that the induced damage upon the surface is kept minimal. As specified by the manufacturer, the spring constant should be set to 242.38 N/m. Once these parameters are in place, a calibration curve can be created as seen in Figure 16.
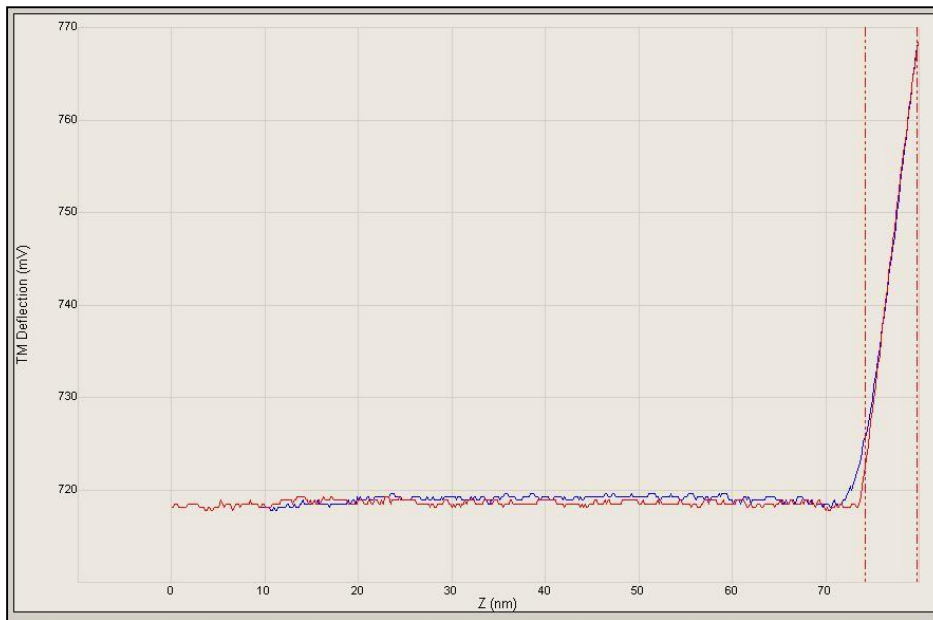
Figure 16: Calibration diagram obtained through AFM calibration.

Within the calibration curve the two vertical lines encapsulating the areas of high slope for the loading and unloading curves are user-set markers used to calibrate the sensitivity of the scanner head. In this image, as well as all AFM indentation output plots, the blue and red curves represent loading and unloading respectively. Once the sensitivity has been calibrated, changing

of the probe holder alone should be avoided. To best preserve the sensitivity calibration, the entire scanner head should be removed when changing the samples.

2.2.5 Testing Procedure

Upon completion of the polishing procedure discussed in Section 2.1.3, the sample is mounted on a 12 mm stainless steel sample disk using double sided tape or adhesives. The disk is then mounted in the AFM scanner head and held stable by magnets located within. For purposes of AFM imaging analysis, a tip is then mounted in the probe holder which is placed in the scanner head. The tip is then manually lowered close to the sample surface. Then, the laser is to be aligned. The laser is aligned by adjusting the sum and difference so that the reflected laser is detected by the photodiode detector. Through software functions, the tip is fine-tuned to its' resonant frequency. The scan location, size, and other initial parameters such as the desired resolution and integral and proportional gains are input by the user. The tip is then lowered to the appropriate distance in relation to the sample surface, beginning the imaging process. Gains and amplitudes may need to be adjusted at this point depending on the resulting image quality. Once the image quality desired is obtained, the image can then be captured for analysis via software of the users' choice.   For AFM indentation analysis, post mounting the sample within the scanner head, a special probe is mounted into the probe holder by the manufacturer. The area of interest must then be centered in the scan. Similar to the imaging tip, the indenter tip is lowered to an appropriate distance from the sample's surface allowing for scanning to begin. To perform an indent, the scan is stopped in the desired location and a ramp is performed. For this step it is important the trigger threshold is set with caution so that the tip is not damaged. For the tip used in this analysis, it is not recommended the threshold not be larger than 1 V. Once the ramp has been completed, the scan area is re-analyzed so that the indent can be seen. To

properly retrieve force-displacement curves (loading and unloading), the appropriate spring

constant and deflection sensitivity must be input as parameters which can be done before initial

indentation of a material or during post-image processing.

2.3 Thermogravimetric Analysis

Thermogravimetric Analysis (TGA) is a method of thermal analysis that monitors

changes in mass caused by physical and/or chemical processes with respect to temperature or

time within a controlled atmosphere (i.e. oxygen, nitrogen, argon). Through TGA the rate and

quantities at which organic constituents of a specimen evolve can serve as an age distribution

index. Also, the detection and analysis of moisture content, decomposition rates, and reactions

such as pyrolysis is possible.

2.3.1 Sample Preparation

Due to the nature of TGA testing, specimens in their raw forms are typically preferred.

However, the main preparation point for this analysis is for the equipment in use, small sample

sizes are required (8 - 20mg). Therefore before beginning testing, specimens should be

"chipped" into smaller pieces. Being cautious not to crush the sample, the preservative mineral

oil should be dried as thoroughly as possible from the exterior of the sample as it will give false

readings if there is an abundance of mineral oil along with the sample. To dry the samples

without inflicting damage or temperature fluctuations prior to testing, clean absorbent cloth can

be used to gently remove the oil from the sample surface.

2.3.2 Description of Equipment

TA Instruments TGA Q500 model is a high performance thermogravimetric analyzer that

utilizes a responsive low-mass furnace, sensitive thermobalance, and an efficient horizontal

purge gas system (Kadine Mohomed). The furnace equipped is a standard furnace used for high resolution runs with an average cool down time of twenty minutes, although this may vary dependent on maximum temperature and duration of testing. The balance (for tare function described in Section 2.3.3) operates on the null-balance principle. This principle states that at zero, or "null", the amount of light shining upon the two photodiodes will be equal. When the balance moves out of this position, unequal amounts of light will be detected allowing a current to be applied to the meter movement and return to the balanced position. The weight loss experienced during a test is proportional to the amount of current applied.
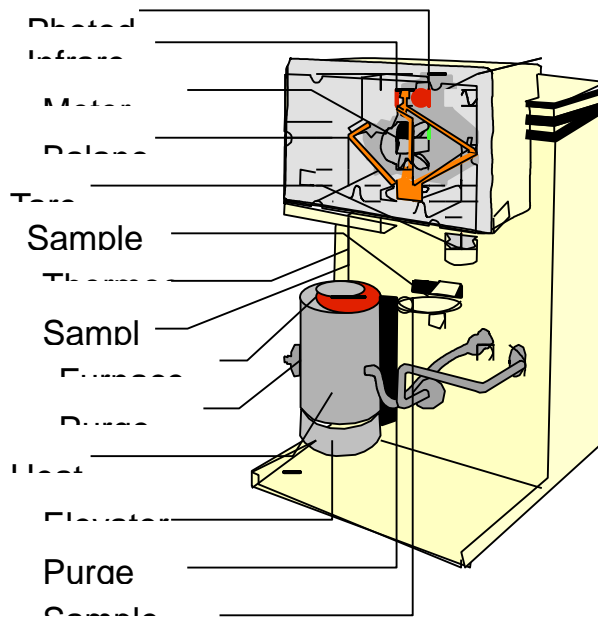

Figure 17: Typical schematic for TA Instruments Q500 TGA (Kadine Mohomed).

Figure 17 displays a typical cross section of the features found within TA Instruments Q500 TGA. Figure 18 and 19 show the same model as set up and used by the University of Mississippi NIRG. Out of sight includes an individual computer for collecting and analyzing data obtained throughout testing (left) and nitrogen gas tank (right) which is connected to the purge gas inlet.
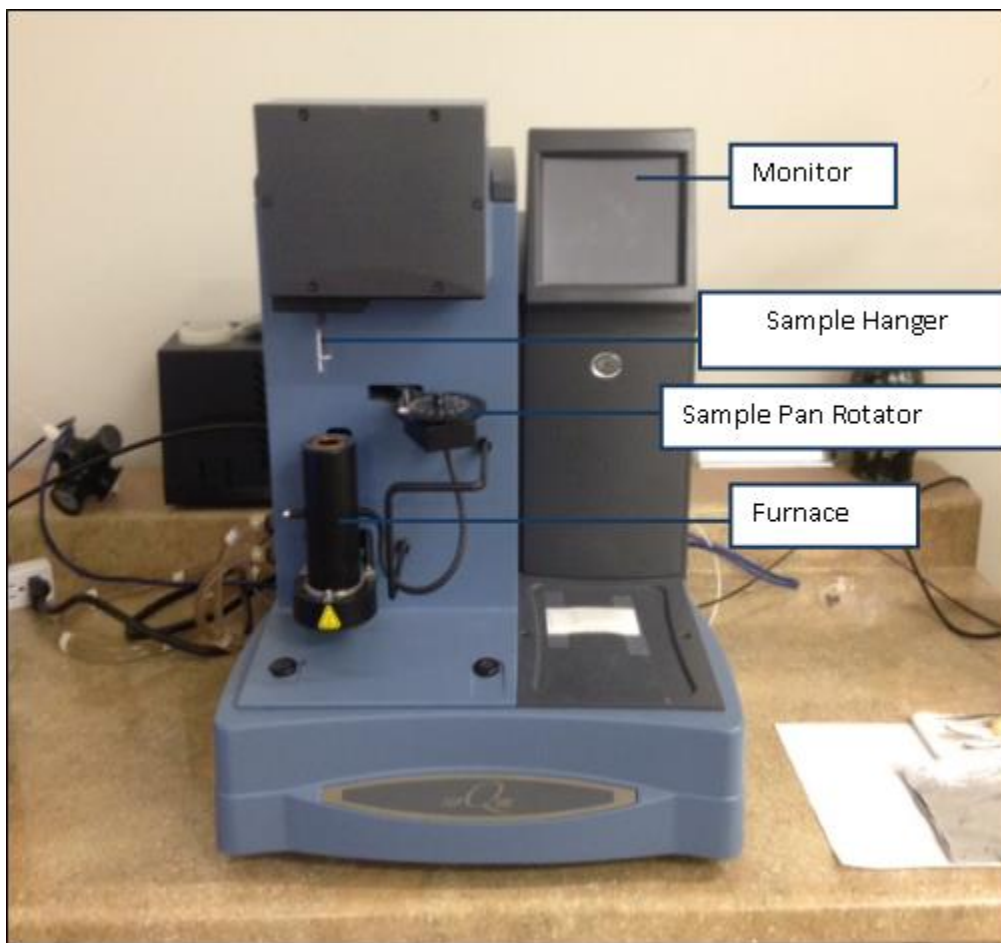
Figure 18: TA Instruments TGA Q500 as used by NIRG, University of Mississippi.
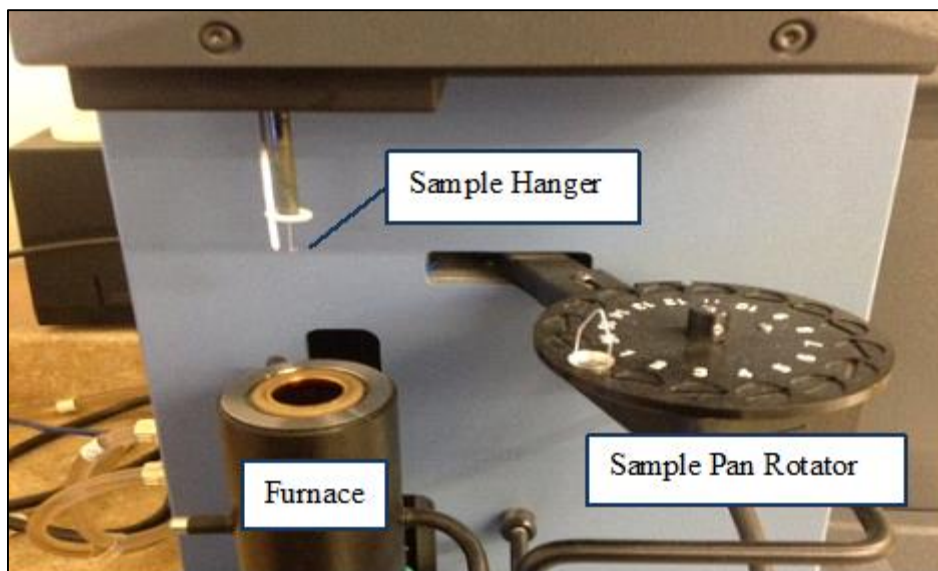
Figure 19: Close-up view of TA Instruments TGA Q500 as used by NIRG, University of

Mississippi.

2.3.3 Testing Procedure

To begin, a clean, platinum pan should be used for testing. While pan is in the testing
position (on the hook) and stable, close the furnace. Then, the pan should be tarred to balance
out the self-weight of the pan. Once tare is complete, open the furnace, remove the pan from the
hook and place in a contaminant free area. Place the prepared sample into the center of the pan.
Then, gently replace the pan with the sample in it, back onto the hook. It is important that the
sample be loaded off the hook to prevent altering the calibration of or damage to the weighing
apparatus. Once the sample and pan are stable, close the furnace and begin the test.

For this research, a temperature ramp of 10°C per minute was performed for each sample
depth until reaching a maximum temperature of 700°C. For better understanding of how the
mineral oil in which the specimens are preserved in effects the material properties, similar tests
were also performed. In order to determine the rate of decomposition of the organic contents, an

additional temperature ramp of 2°C was performed until reaching a maximum of 700°C, and

then compared with the results of the 10°C ramp rate.

2.4 X-ray Diffraction Analysis

XRD methods are used primarily for the quantification of inorganic contents within a

sample. Organic, non-crystalline materials and volcanic glass of large concentrations may be

detected through XRD analysis, however cannot successfully be quantified (Talbot, 2012;

Weatherford Laboratories, 2012). Quantification of the inorganic contents of a sample is done

through weight percentage data collected from testing and is considered to be a semi-quantitative

method of analysis. Due to the detection limitations of XRD (1-5 %weight), many factors can

influence the results. Minerals such as feldspars and clays are especially problematic as they

undergo solid solution and have a wide range of crystallinities (Talbot, 2012). Because the data

collected is in the form of weight percentages, but commonly reported as weight fractions, each

of the components within a sample equates to 100%. This creates opportunities for error during

quantification as if one component is underestimated or not detected altogether, the remaining

components will be overestimated. Typically, errors of this nature are easily overcome with

multiple analyses and extreme care of the samples tested.

2.4.1 Sample Preparation

Woodford shale samples were sent for testing to two separate companies, K-T

GeoServices Inc. and Weatherford Laboratories. The sample procedures were provided courtesy

of James Talbot and Angela Schwartz (K-T GeoServices and Weatherford Laboratories

respectively) and have been broken down as follows.

Sample preparation for specimens to be tested for whole rock and clay mineral XRD

analyses as performed by K-T GeoServices (Talbot, 2012):

1. Removal and cleaning of obvious contaminants from approximately 2-5 grams of sample.

2. Disaggregate sample by use of a steel mortar and pestle.

3. Split disaggregated sample in two. One half will be transferred into distilled water for clay fraction analysis and the other is to be pulverized using a McCrone micronizing mill (approximately 8 minutes) for whole rock analysis.

4. For clay fraction analysis, a sample split of each sample is dispersed by use of a sonic probe.

5. Samples with clay suspensions are placed in a centrifuge and ran for 5 minutes at 600 rpm.

6. The suspensions are then size fractionated with a centrifuge to isolate clay-size (< 4 μm spherical diameter) materials for clay mounting.

7. Suspended deposits are then vacuum deposited on nylon membrane filters to produce oriented clay mineral mounts which are then attached to glass slides, placed in vacuum oven at 40°C and exposed to ethylene glycol vapor for approximately 12 hours. Afterwards, the sample can be removed from the oven and is ready to be tested.

8. For bulk (whole rock) analysis, once milling is completed, the resulting slurry is placed in an oven to dry.

9. Disaggregate dried powder sample and place into sample holder. Once this is done the sample is ready to be tested in diffractometer.

Although similar, sample preparation for specimens to be tested for whole rock and clay mineral XRD analyses as performed by Weatherford Laboratories (Weatherford Laboratories, 2012) is as follows.

1. A representative portion (approximately 2 grams) of each sample is cleaned utilizing a mixture of chloroform and methyl alcohol (70:30 %volume respectively). Chloroform is used for the removal of any oils whereas the methyl alcohol is used to remove any salt deposits associated within the mud system. If indigenous salt is to be retained, methyl alcohol should be omitted completely.

2. Cleaned samples are then dried in a laboratory oven at 110°C for a minimum of 1 hour.

3. Once dried, the samples are ground in a Retsch MM-400 ball mill to a fine powder (1-5 μm spherical diameter). For bulk (whole rock) analysis, sample preparation is complete.

4. For clay fraction analysis, a split of the powder samples will be taken and checked for carbonate minerals using 10% HCl. Treating the samples with this will remove all carbonate materials present within the samples.

5. Samples are then washed using a sodium hexa-meta-phosphate (deflocculating agent) and distilled water mix.

6. Samples are then dismembrated using a Fisher Scientific Ultra Sonifier to produce suspension of the clay material.

7. Clay materials are then further fractionated by placing samples into a centrifuge to separate the size fractions between 1-15 μm.

8. The sample is then passed through a filter membrane apparatus which collects the

solids on a cellulose metrucel membrane filter.

9. Solids are transferred to glass slides and is glycolated using 99.9% ethylene glycol for 12 hours at 110°C. Once complete, the sample is ready to be tested in diffractometer.

2.4.2 Description of Equipment

In general, X-ray diffractometers are composed of a source of monochromatic radiation and an X-ray detection apparatus located amongst the circumference of a graduated circle centered on the powder specimen as seen in Figure 20. Divergent and receiving slits located between the X-ray source, sample, and X-ray detector, limit the scatter of radiation, reduce the effects of background noise, as well as collimate the radiation. To allow for consistency in measurements during testing, the detection apparatus and the sample holder is mechanically coupled with a goniometer so that the rotation of the detector and the specimen retain a fixed 2:1 rotation ratio respectively (Talbot, 2012).
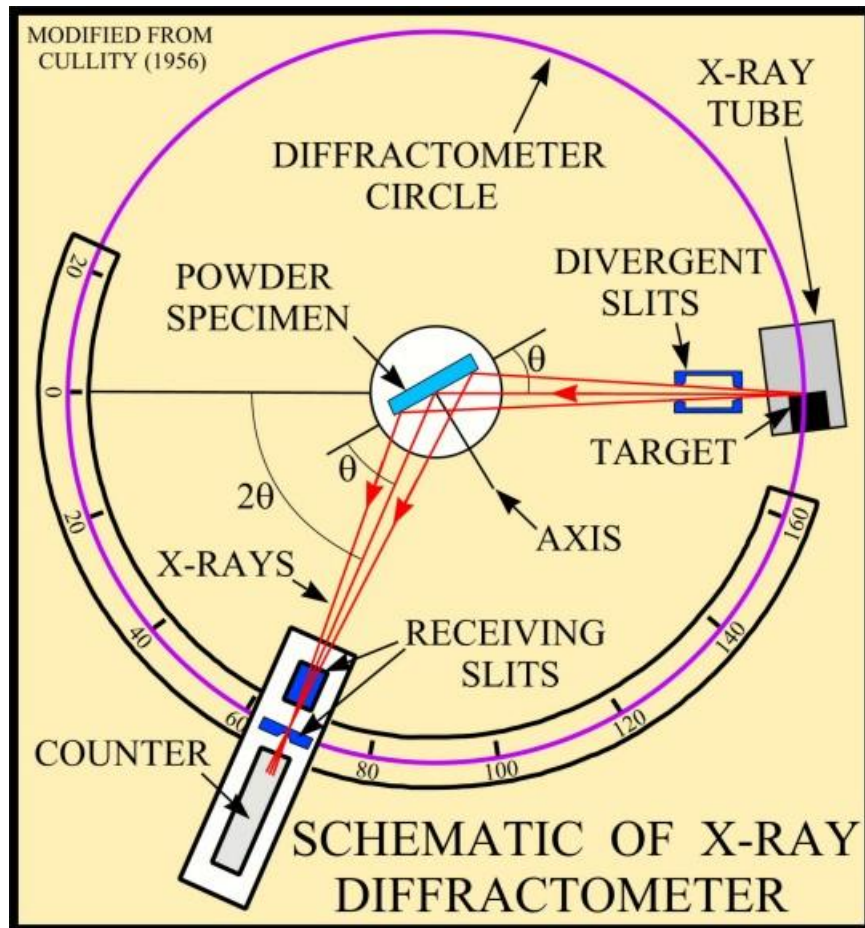
Figure 20: (TYP) Schematic of X-ray diffractometer (Talbot, 2012).

K-T GeoServices Inc. uses a Siemes D500 automated powder, X-ray diffractometer equipped with a copper X-ray source (40kV, 30mA) and a scintillation X-ray detector displayed in Figure 21.

Figure 21: Siemens D500 automated powder X-ray diffractometer as used by K-T GeoServices (courtesy James Talbot, K-T GeoServices Inc.) (Talbot, 2012).

Alternatively, Weatherford Laboratories use a Bruker AXS D4 Endeavor series X-ray diffractometer (Figure 22) which makes use of copper K-alpha radiation. Within this setup, a nickel filter slit is in place to eliminate K-beta peaks as well as an air scatter screen to reduce the effects of background noise.
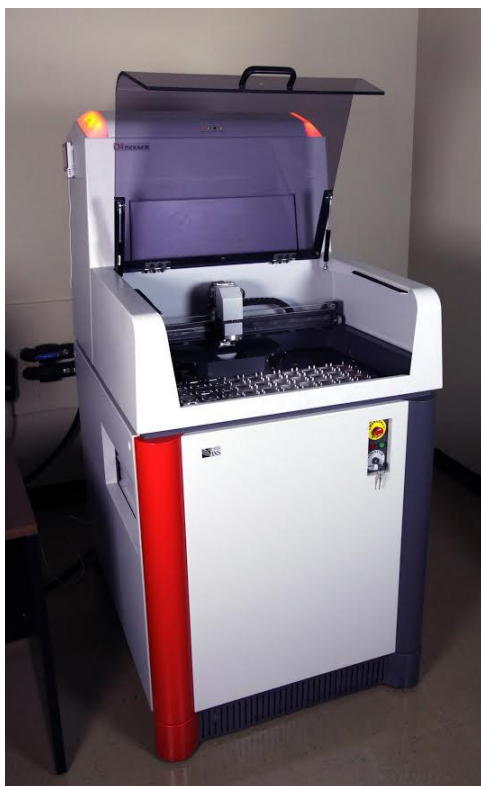
Figure 22: Bruker AXS D4 Endeavor X-ray diffractometer as used by Weatherford Laboratories (courtesy Angela Schwartz, Weatherford Laboratories) (Weatherford Laboratories, 2012).

2.4.3 Testing Procedure

As two separate companies were utilized for testing, each of their respective testing procedures will be outlined. These testing procedures follow directly from the sample preparation practices utilized by each company. To begin, K-T GeoServices Inc. analyses the whole rock samples over an angular range of 5° 2-theta to 60° 2-theta at a scan rate of 1°/minute. Likewise, the glycol solvated, clay mounts are analyzed over an angular range of 2° 2-theta to 36° 2-theta at a scan rate of 1°/minute. XRD patterns from air-dried and glycol solvated, clay-fraction samples are qualitatively analyzed to determine the types of clays present in the samples (Talbot, 2012). Semi-quantitative determination of whole rock mineralogy is done using Jade Software from *Materials Data Inc.*, utilizing the whole pattern fitting (WPF) option. Diffraction

models are then fit to the measured pattern by non-linear least-square optimization allowing for variation of parameters to improve the fit of the model to the actual, observed data. The results of this analysis are seen in Figure 83 and 78.

Weatherford laboratories, after sample preparation has been completed, carefully hand-loads the slides containing the samples and tests the clay separates at 2°2-theta to 30°2-theta at a step rate of 0.025° per step corresponding to a dwell time of 0.15 seconds at each step in order to identify expandable, water sensitive minerals. The slide is then heat-treated at a temperature of 565°C and rescanned to further aid in distinguishing kaolinite and chorite. Once the clay is heated and the kaolinite and smectite peaks collapse, the chorite peak becomes more prominent and the descrete illite plus the illite associated with the mixed-layer illite/smectite is rendered. Utilizing the Jade Software from *Materials Data Inc.*, mineral phases can be obtained at the maximum peak heights using d-line spacing functions. Once bulk data analysis is complete, the total clays obtained are reduced into their species and values are assigned to each mineral phase.

CHAPTER 3: RESULTS AND DISCUSSION

3.1 Overview

Woodford shale was tested in both core and chip form to determine if testing chips (relatable to drill cuttings) can be representative to tests performed on a core sample. Various procedures and studies were performed such as nanoindentation of single and multi-layers, effects of polishing procedures, atomic force microscopy (surface imaging and indentation), thermal gravimetric analysis, as well as X-ray diffraction. Similarly, testing of Tuscaloosa Marine shale was performed so that quantification of its mechanical properties is possible for comparison to other shale plays such as the Woodford shale. For the Tuscaloosa Marine shale, two samples from fifteen distinct measured depths were tested for a total of 30 samples. The correlations between mechanical and petrophysical properties are explored and discussed throughout this chapter.

3.2 Factors Influencing Nanoindentation Results

3.2.1 Effects of Anisotropy

There are many factors that can influence the results obtained from nanoindentation testing such as anisotropy, thermal drift patterns, polishing and applied loading affects. Anisotropy refers to a physical property of materials in which different values are obtained when measured in different directions. As shale materials are easily recognized as layered materials, the direction of loading during nanoindentation testing is naturally a concern. Separate loading

cases have been tested to determine how greatly the orientation of the layers impacts the final

results (i.e. elastic modulus and hardness). Elastic modulus and hardness results were first

obtained through nanoindentation of a single layer of the specimen. This was done by indenting

Woodford shale, core specimens in which the layering was clearly distinguishable. Figure 23 and

24 show these results.
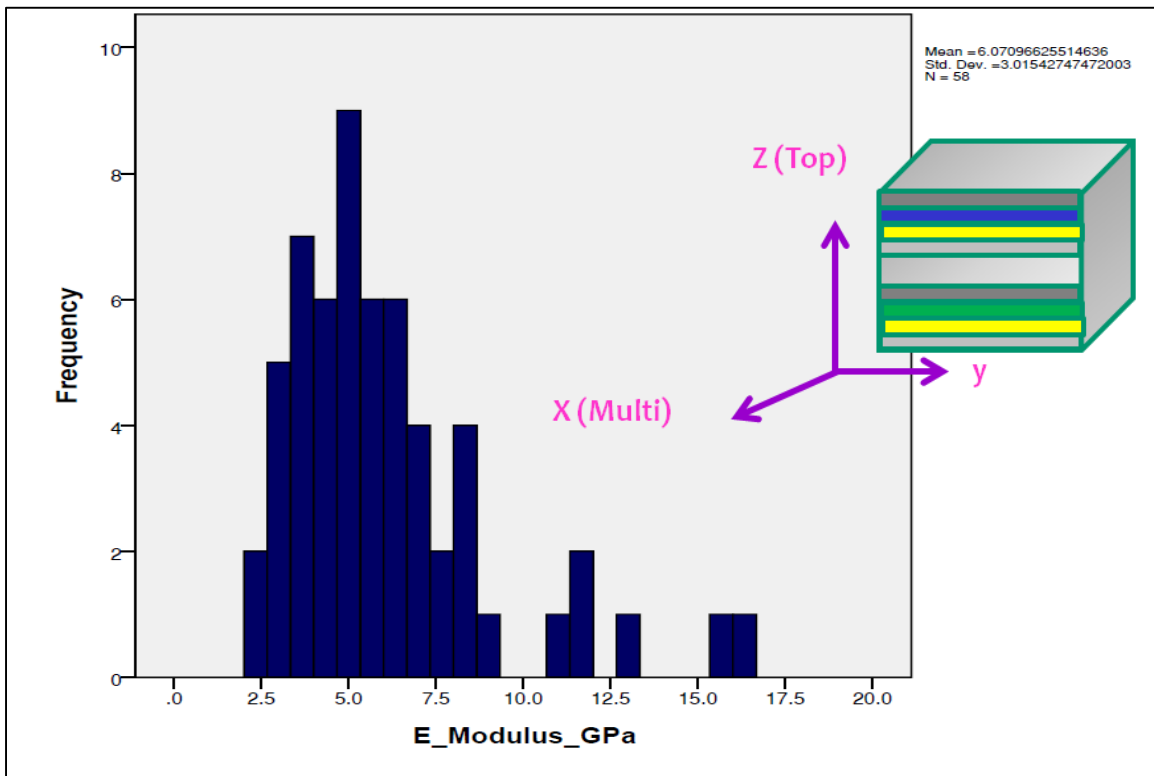
Figure 23: Elastic Modulus results of indents performed on single layer of the specimen

(perpendicular to bedding).
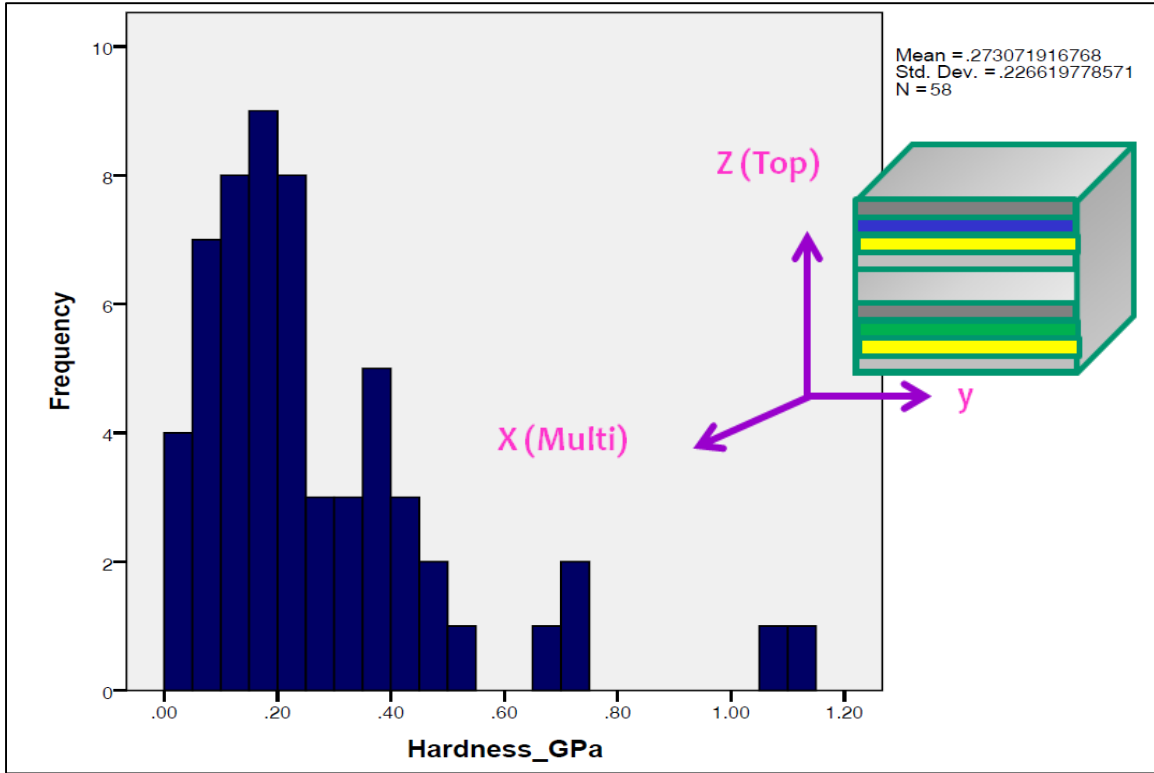
Figure 24: Hardness results of indents performed on single layer of specimen (perpendicular to bedding).

For comparison, the same core sample was then tested in the multi-layered orientation as seen in Figure 25 and 26.
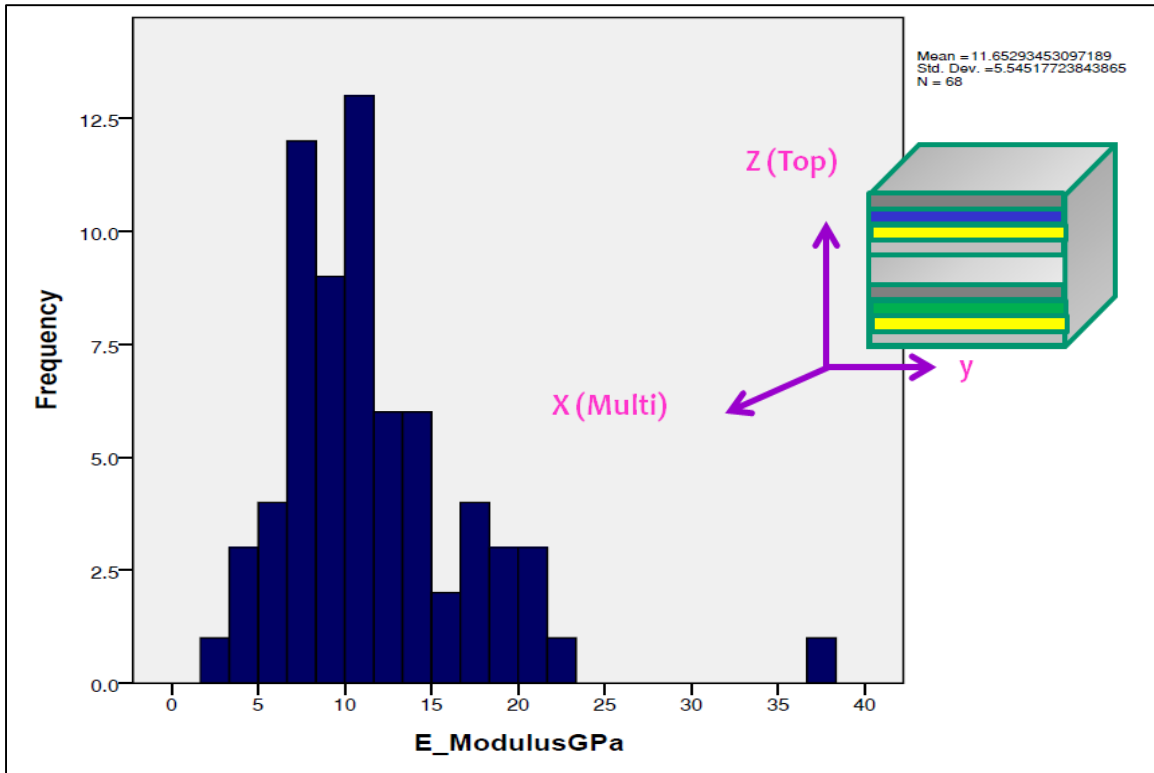
Figure 25: Elastic Modulus results of indents performed on multiple layers of specimen (parallel to bedding).
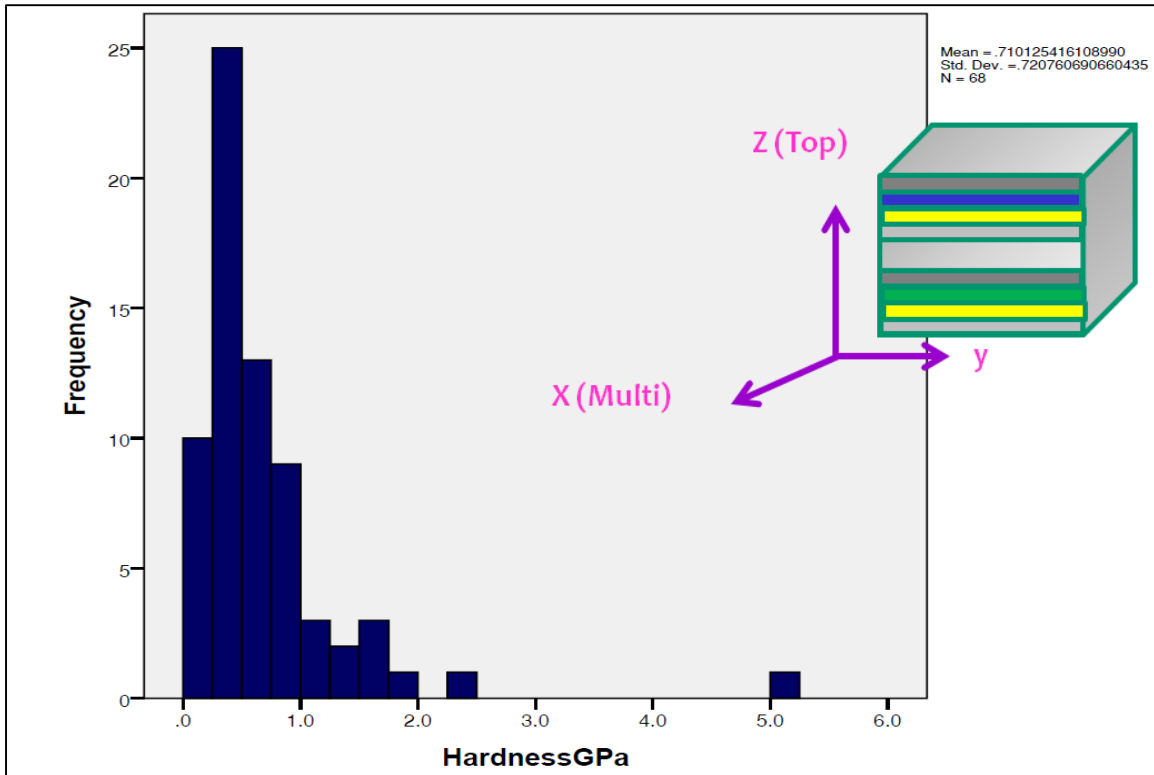
Figure 26: Hardness results of indents performed on multiple layers of specimen (parallel to bedding).

From this it can be seen that there are differences in the values obtained dependent on the direction of layering undergoing indentation. Though it would be ideal to apply this information to procedures such as the hydraulic fracturing process, the orientation of these layers are not always distinguishable in situ which can altogether eliminate the need for multi-directional nanoindentation practices for the purpose of shale extraction data.

3.2.2 Effects of Thermal Drift and Creep

Thermal drift is a factor commonly encountered within nanoindentation testing. It is one of two types of drift behavior that may be observed during testing. The other of the two drift behaviors is known as creep. Creep is a drift within the specimen itself as a result of plastic flow. Creep effects are easily identified by holding the maximum load during nanoindentation

testing constant for a duration of time (varies dependent on materials and studies being performed) and then retracting the indenter from the specimen. If creep effects are present, the displacement into the sample will continue as the load is held constant as Figure 27 shows.
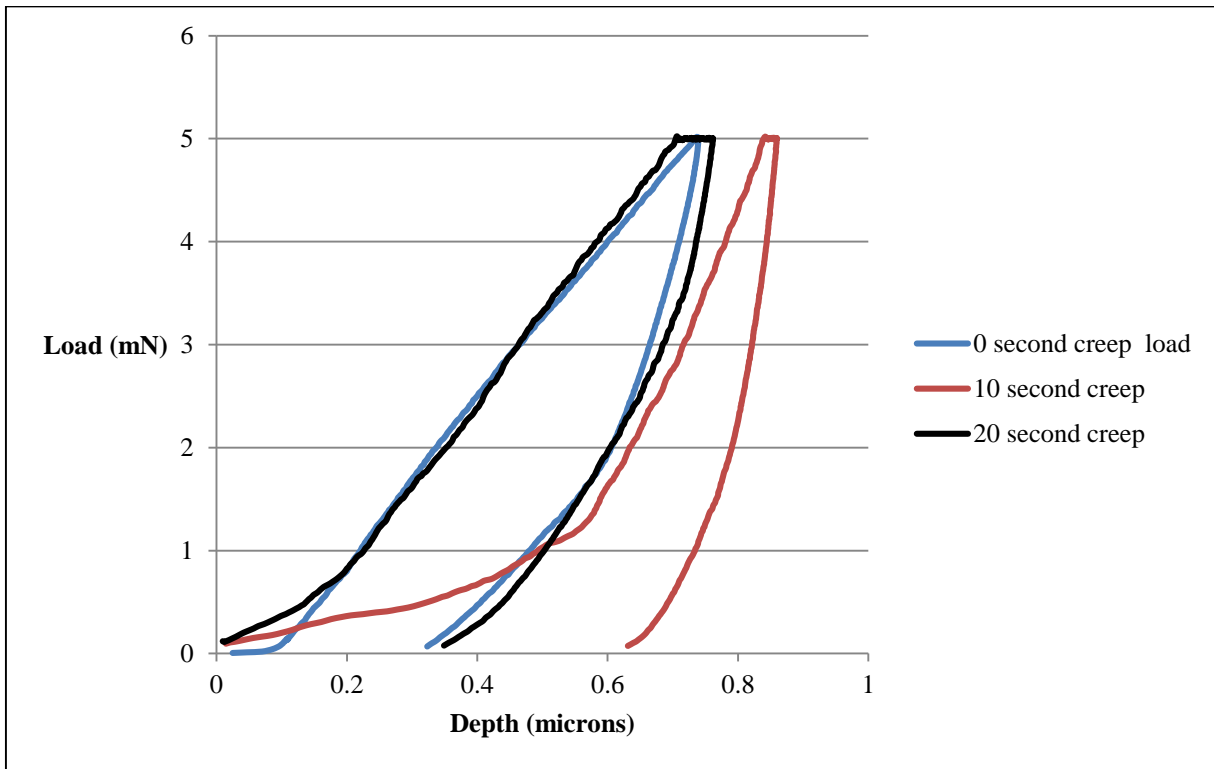
Figure 27: Effect of creep loading.

It has commonly been noted that another reason for the change in depth under a constant load is due to a thermal expansion or contraction of the apparatus, which is nearly indistinguishable from creep. However, as explained in Section 2.1.4, the effects of thermal drift are often negligible.

3.2.3 Effects due to Applied Loading

Another factor that can influence the results obtained from nanoindentation is the effects due to applied loading. As Figure 28 shows, the final depth of indentation directly corresponds

to the magnitude of the applied loading. Due to this, initial testing should be done to determine the appropriate loading required to achieve desired results.
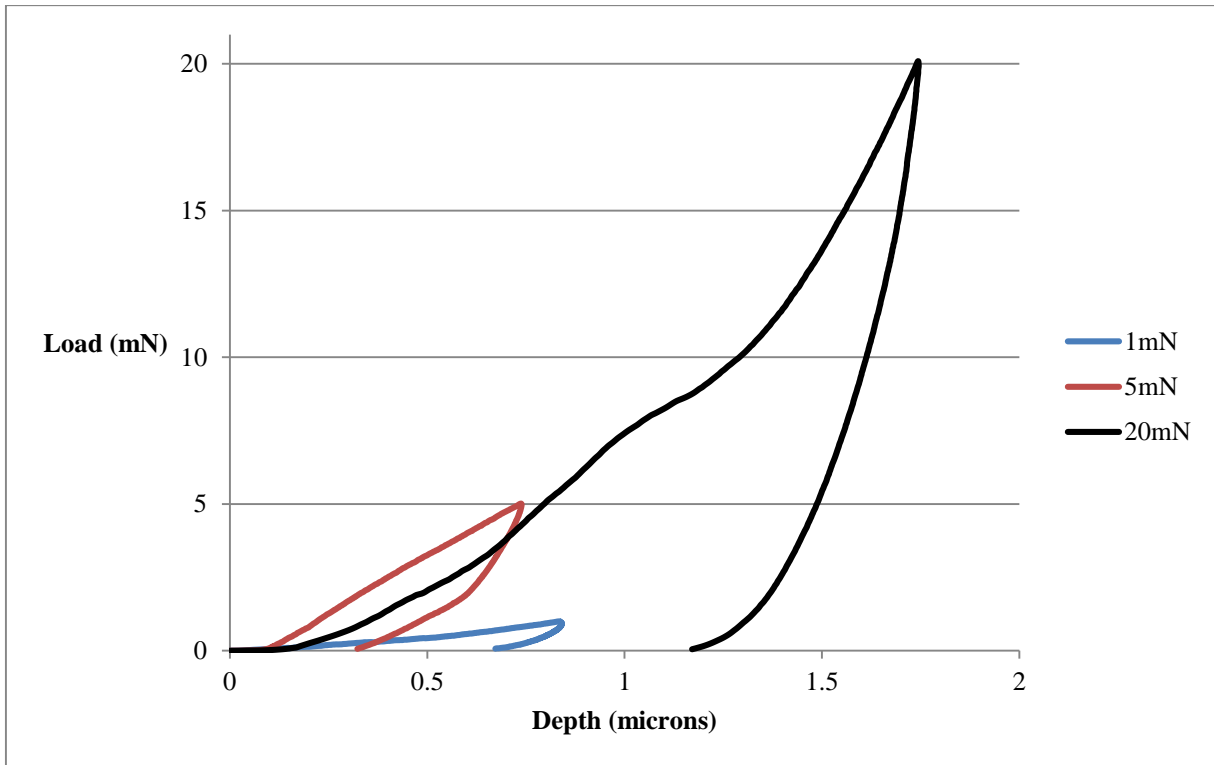
Figure 28: Variation of results dependent on the magnitude of applied loading.

This form of preliminary, initial testing is also beneficial as a means of determining the magnitude of applied loading necessary to alleviate the effects of surface roughness. Surface roughness is one of the most significant contributors of error within nanoindentation testing. These effects are discussed in detail in Section 3.3.

3.2.4 Effects of Surface Roughness

In order to determine adequate polishing procedures, an analysis of different Woodford Shale AFM scans were performed which included a comparison of the Ra (average roughness) and Rq (root mean square roughness) values across various polishing levels for 80x80 and 100x100 µm scan sizes. The Woodford Shale was selected for initial analysis as there is a

broader literature base for comparison of collected data than that of the Tuscaloosa Marine

Shale. For this reason, all results to be presented correspond to that of the Woodford Shale until

otherwise noted. The grit sizes 15, 5, 1, 0.3, 0.05 μm used during polishing will hereinafter be

referred to as Levels 1, 2, 3, 4, and 5, respectively. Samples prepared using ion beam milling

will be referred to as Level 6 polishing.

To account for variability in the topography of each sample's surface, two locations were

imaged on each sample. Figure 29 shows the two images corresponding to their respective

polishing level. Similarly, Figure 30 shows the variation in topography for the ion beam milled

samples. In the second of the two images in Figure 29, a cavity can be seen in the surface. This

is representative of the "peel-out" effect caused by too much initial, mechanical polishing. It is

apparent that this cavity heavily contributed to higher roughness values as seen in Figure 31

through Figure 34.
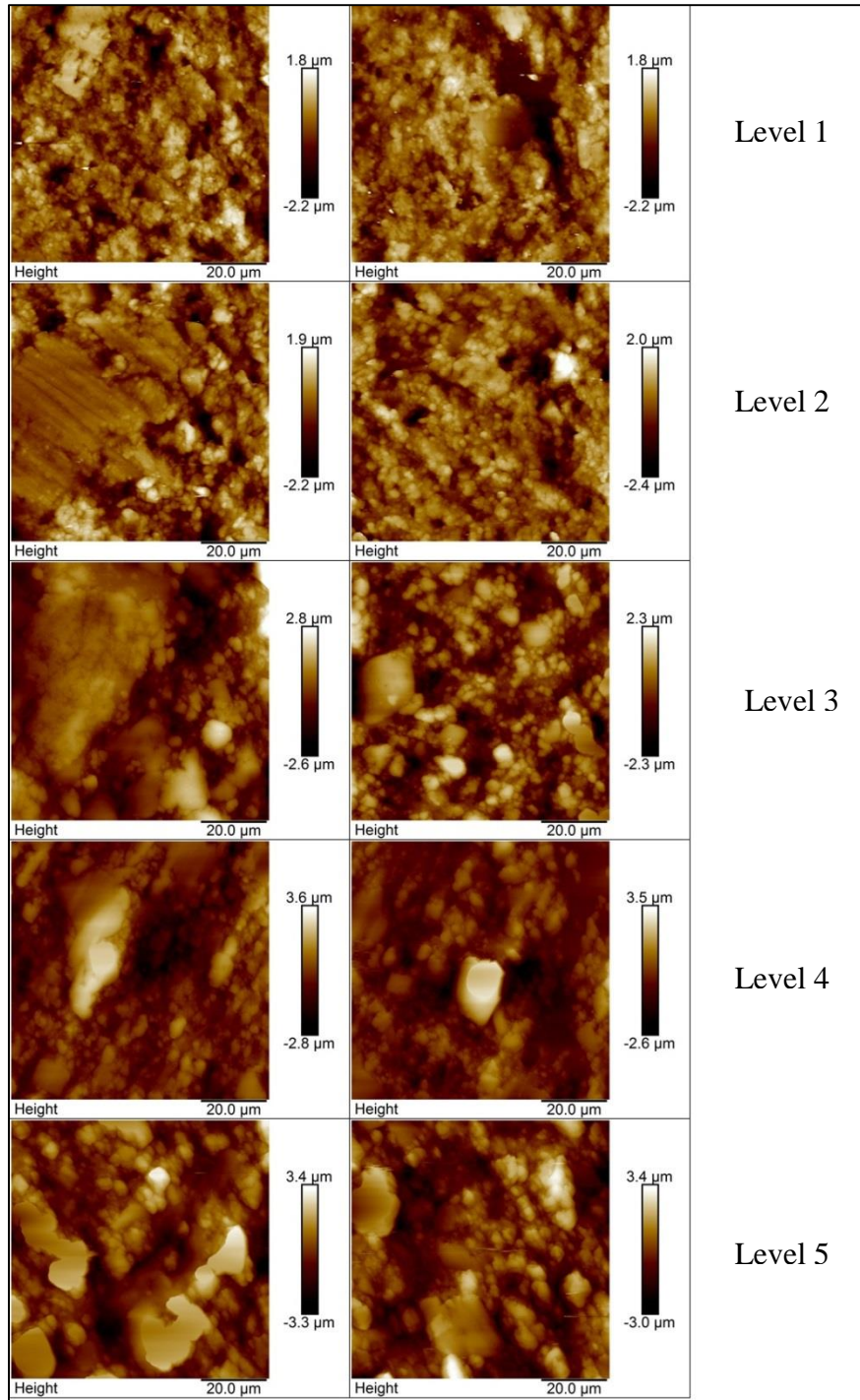
Figure 29: Variation of topography for mechanically polished Woodford samples (80x80 μm).
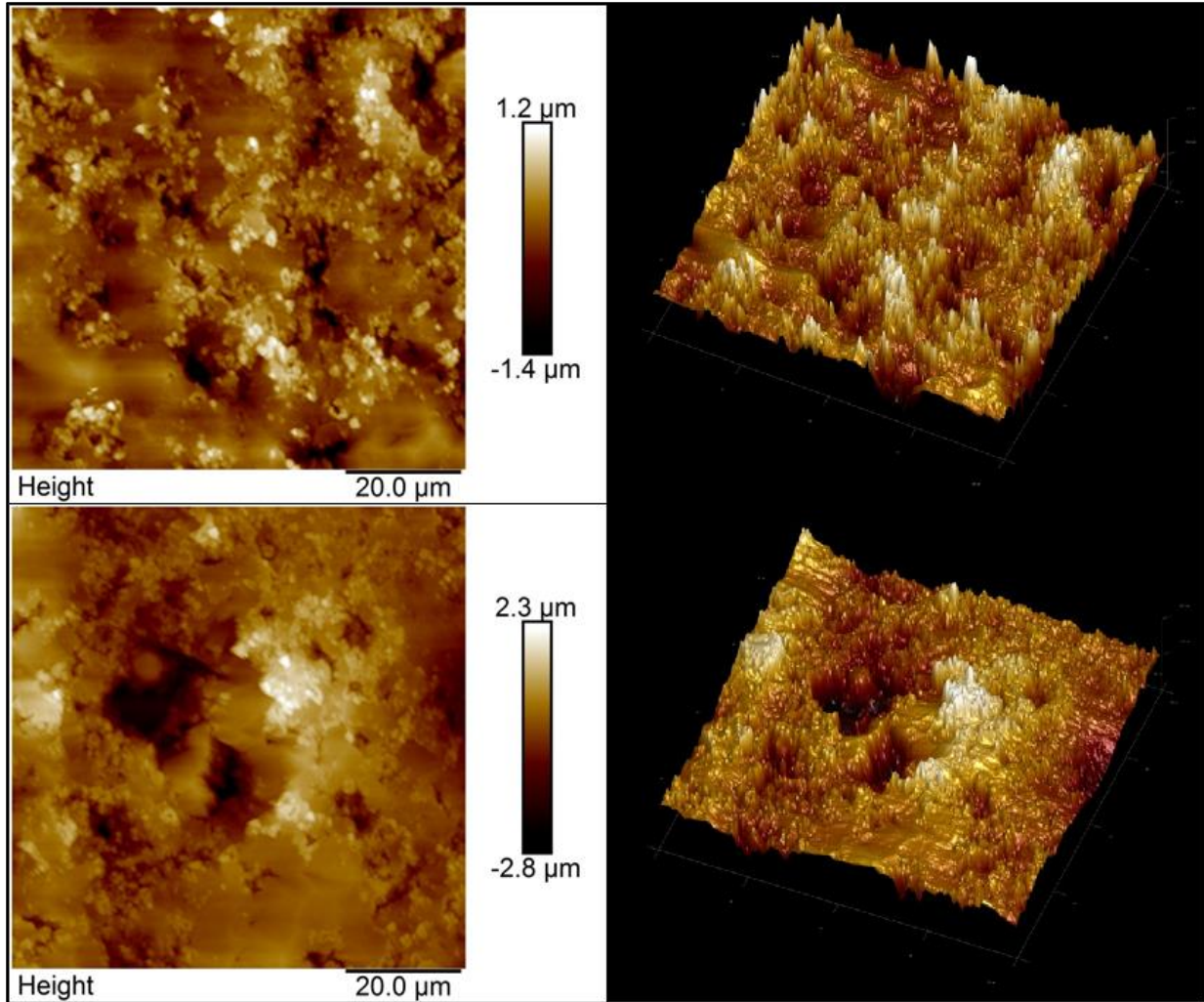
Figure 30: Variation of topography for ion beam milled Woodford samples (100x100 µm).

Figure 31 displays the roughness values for each image taken at the corresponding polishing level. As mentioned previously, the cavity encountered in the second ion milled sample does in fact cause a noticeable rise in roughness values as shown by the first, Level 6 polishing column (far left). It can be noted that, aside from imaging difficulties, roughness values of polishing Level 1 and Level 6 are very similar. Disregarding the ion milled samples, it is shown that the more polishing a sample undergoes, the greater the roughness becomes. This observation confirms the higher the level of polishing used, the greater the variation in the sample topography which directly leads to higher roughness values.
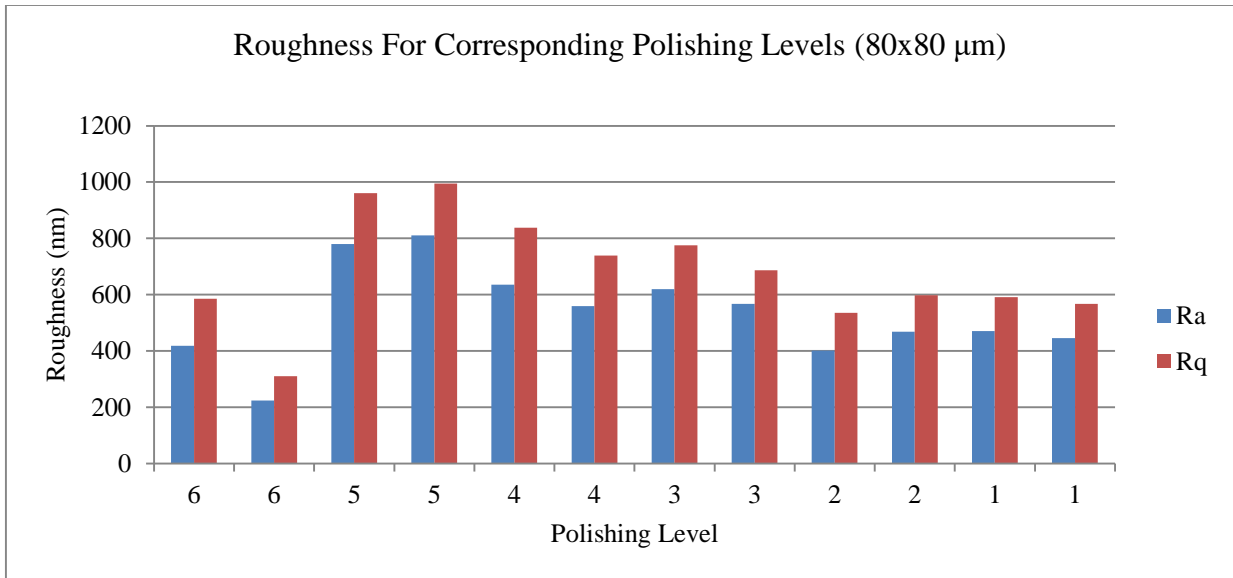
Figure 31: Roughness at different levels of polishing (80x80 μm).

To validate these results and achieve a greater understanding of the samples as a whole, the same procedure was performed on each sample with a change from an 80x80 μm to a 100x100 μm scan. This was performed for all polishing levels with the exception of the ion milled samples as shown in Figure 32. In doing this, it is revealed that although the trend is not quite as definitive in the 100x100 μm case as it is in the original 80x80 μm case, the trend of increasing roughness values with increased level of polishing still exists.
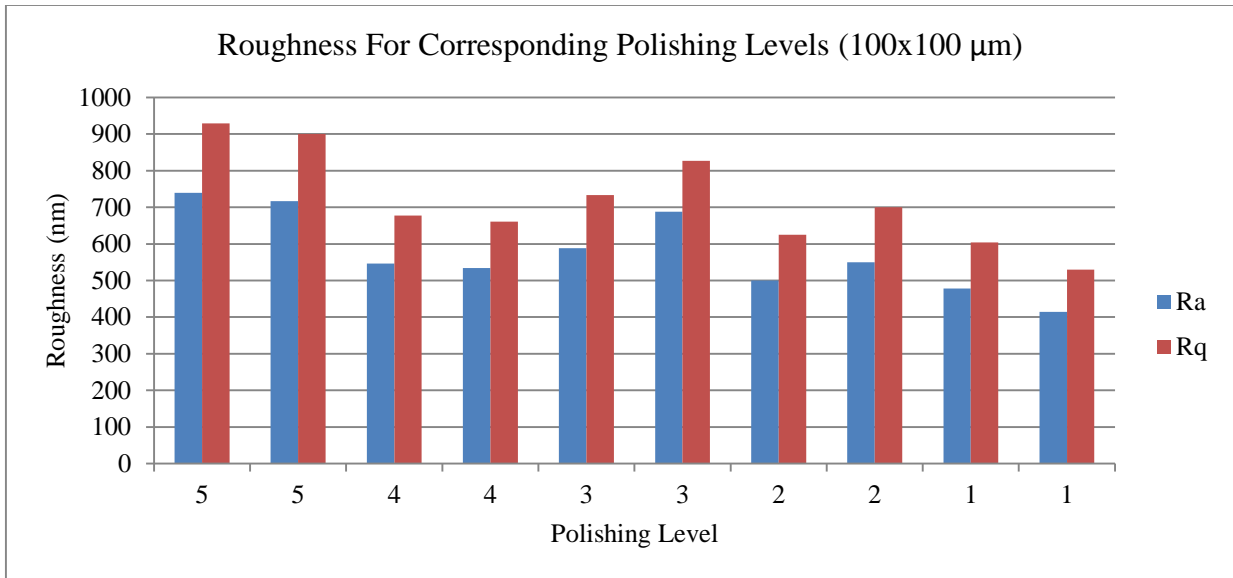
Figure 32: Roughness at different levels of polishing (100x100 μm).

Following the analysis of surface roughness differentiation between each polishing level, the next step is to observe the values relating the distance between the highest and lowest points in each scan, or R_{MAX}. As Figure 33 shows, this analysis did not provide an observable trend such as the trend found in the roughness values.
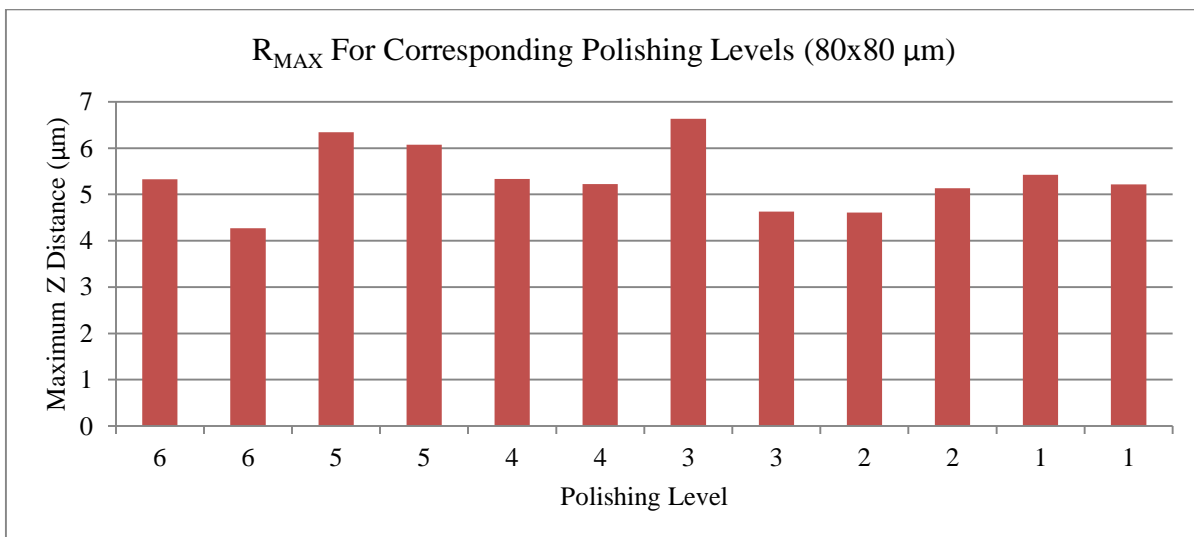
Figure 33: RMAX at different levels of polishing (80x80 μm).

Through this, it can be seen that each polishing level is closely related to one another in terms of the maximum distance between peak and valley. Interestingly, polishing Level 6 (ion milled) column two, was in fact the smoothest of each sample tested in terms of average roughness and displays behavior close to that of the lower polishing levels ($z > 4$ μm). Again, it is possible that the softer, organic material was removed during mechanical polishing prior to experiencing the ion milling procedure. Assured retaining of the organic components in the shales during the polishing procedures will decrease the amount of valleys within the specimens, in turn giving smoother, more accurate results.

Figure 34 shows a comparison of the polishing levels to the surface area difference (SAD). The same trend seen previously is also seen here.
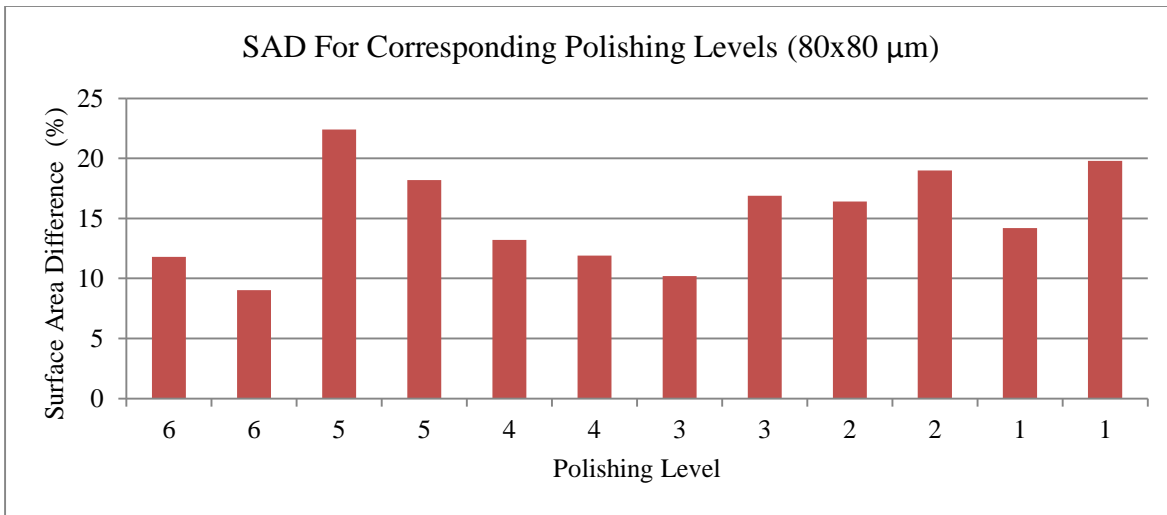
Figure 34: Percent surface area difference for different polishing levels.

The differences between any two images located within the same sample in all comparisons shown can be contributed to the heterogeneity of shale materials. Because softer content tends to experience a peel-out effect once strain-hardening occurs across the sample's surface; harder content is left typically displaying overall smoother areas whereas the softer content can create crack-like features which create an undesirable area for indentation. Though,

for this reason, careful indentation of these areas can also prove to be desirable as it will allow for the determination of average mechanical properties in which will be more representative of the shale sample as a whole.

Lastly, investigation of the impact of the scan size on the Ra and Rq values was conducted. For this analysis, the average of the two Ra and Rq values corresponding to each polishing level were taken and compared between the 80x80 μm and 100x100 μm scans. Figures # and # show these results. It should be noted that the 100x100 μm scans were not completed for the ion milled samples, but instead 60x60 scans were completed. The following plots display this with the 80x80 μm scan acting as a tool for referencing between the mechanical and ion milling polishing levels.
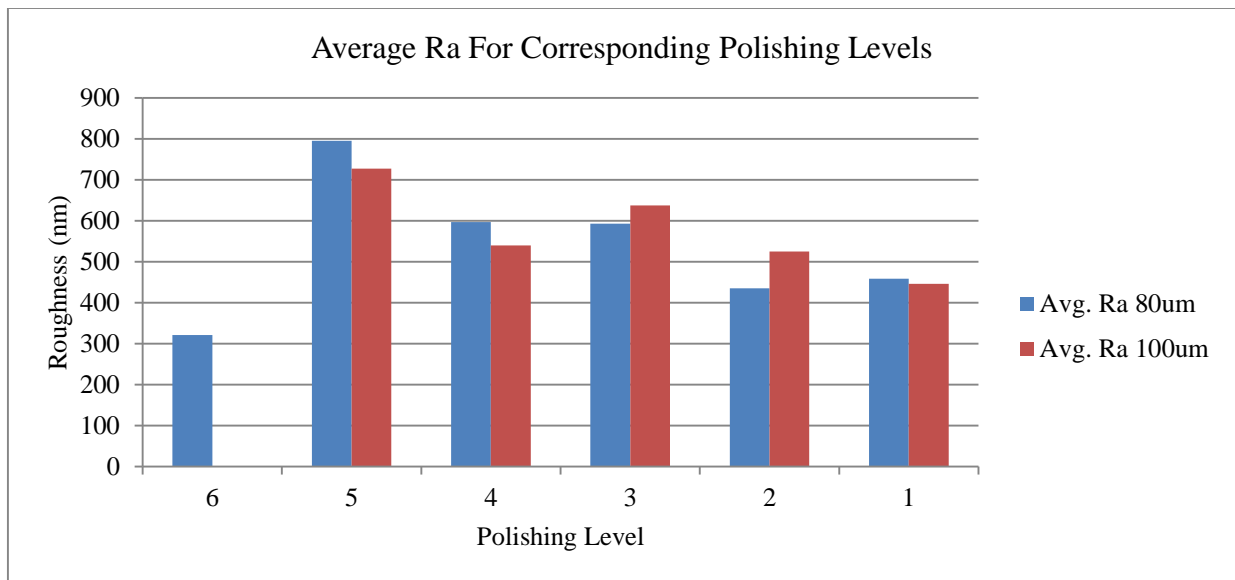
Figure 35: Comparison of average Ra values for corresponding polishing levels at different imaging scan sizes.
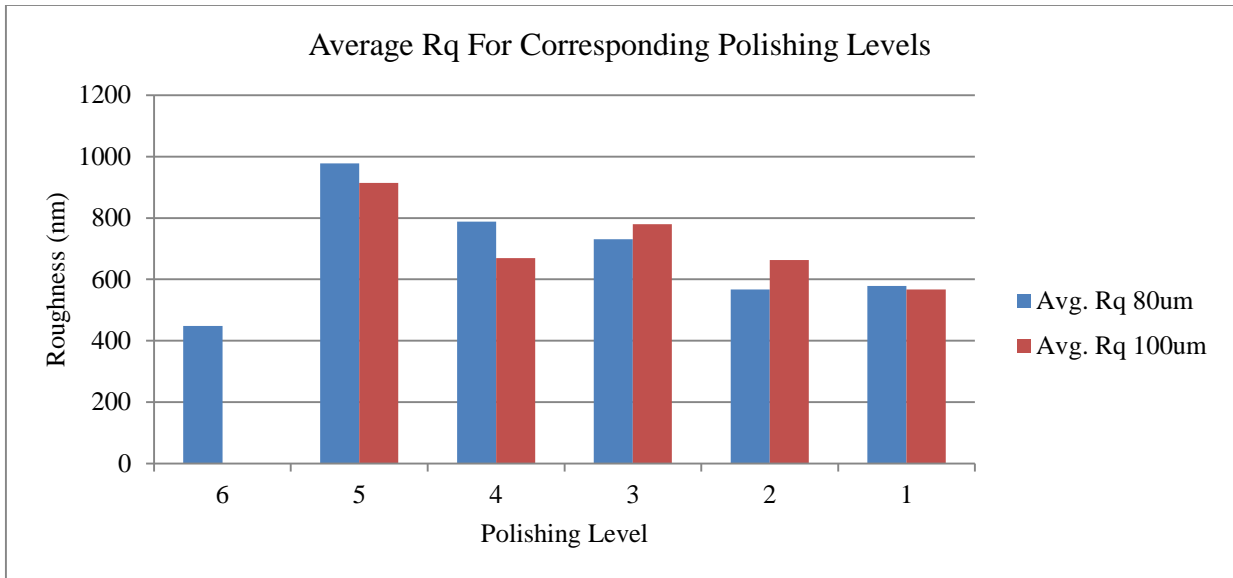
Figure 36: Comparison of average Ra values for corresponding polishing levels at different

imaging scan sizes.
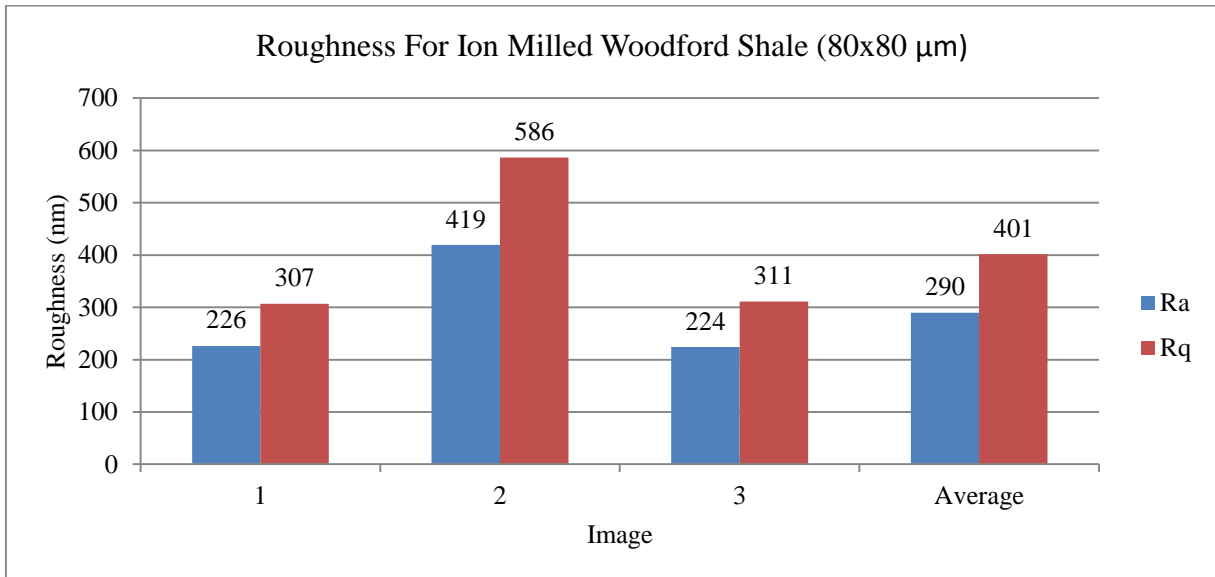
Figure 37: Comparison of roughness values for 80x80 μm scan of ion beam milled Woodford
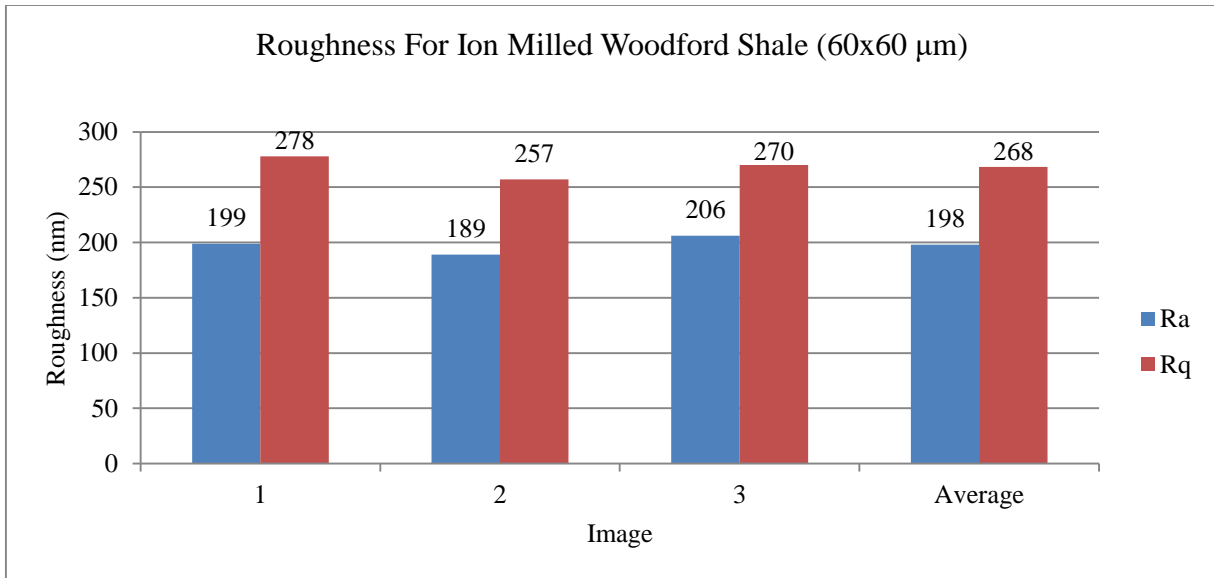
shale.

Figure 38: Comparison of roughness values for 60x60 μm scan of ion beam milled Woodford

shale.

These results show that the smaller scan sizes typically result in lower roughness values;

however, this is not the case for polishing Levels 4 and 5. This is believed to be caused due to

the fact that higher levels of polishing creates more locations where the tip is either dragged

across or loses contact with the surface of the sample. These results are to be expected as in any

likely scenario, a smaller scan may consist primarily of a large fracture in the surface of a sample

whereas in larger scans, the fracture may only appear as a small percentage. However, caution

should be taken when selecting imaging locations if possible as larger scan sizes may also

incorporate multiple fractures or peaks in the topography of the sample.

Through similar means of imaging, the following figures (Figure 39 through Figure 42)

show samples from the same measured depth polished to different levels of smoothness. 80x80

μm images were chosen to stay consistent with that of the Woodford analysis as well as to give a

more accurate representative surface for which the nanoindenter will encounter. Areas circled in

yellow indicate where the tip was elevated to the maximum z-limit of the scan head and

"dragged" across the surface, and those circled in red indicate where the contact surface's elevation lied below the minimum z-limit. Only a few areas displaying these tendencies were indicated as to give a representation of the effects.
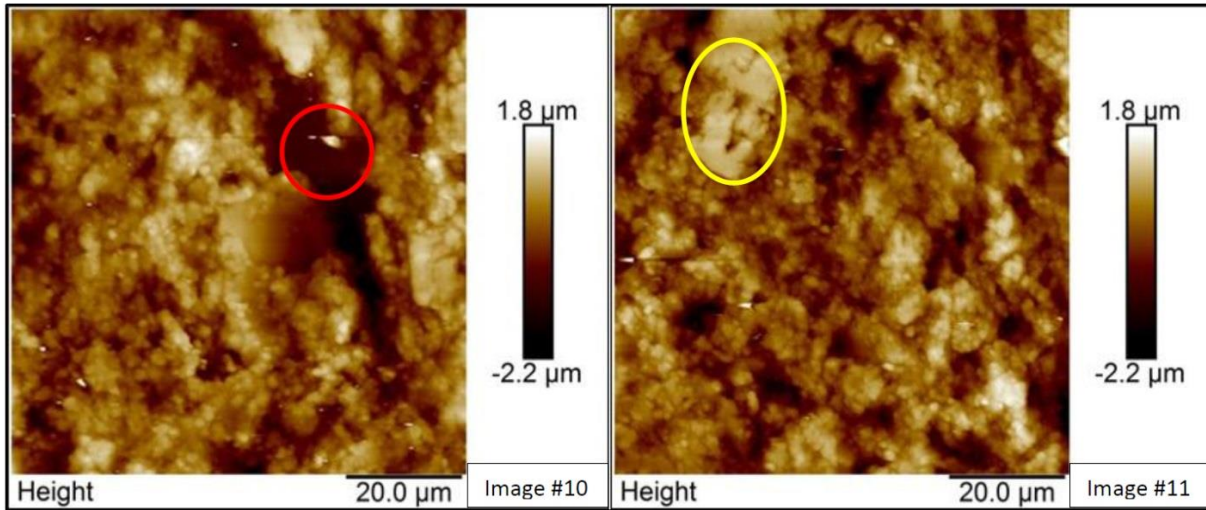
Figure 39: 80x80 μm images of TMS after Level 1 polishing.
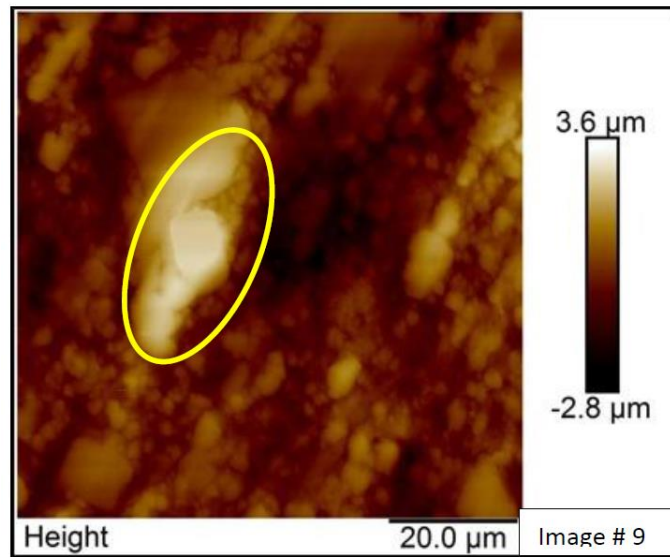
Figure 40: 80x80 μm images of TMS after Level 4 polishing.
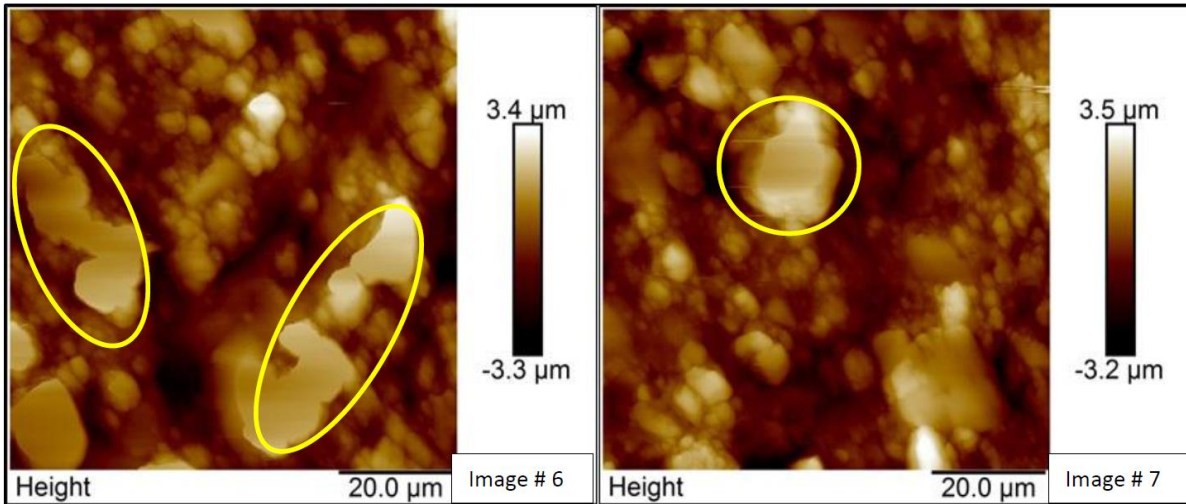
Figure 41: 80x80 μm images of TMS after Level 5 polishing.
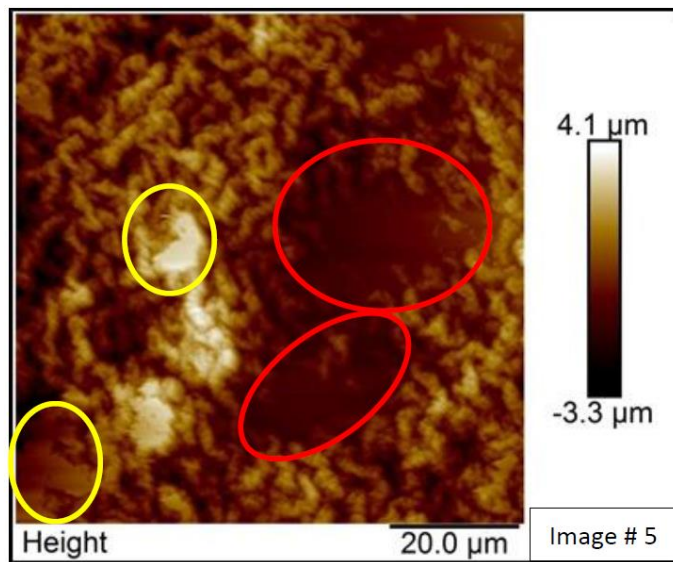
Figure 42: 80x80 μm images of TMS after ion-milling.

All images taken have areas among the surface where the minimum or maximum z-limits were exceeded. Imaging errors that are derived from the sample not being level within the holder tend to be magnified when imaging a larger area due to the distances the AFM tip must travel to complete the scan. Table 8 displays selected properties determined from the image data for comparison to the previously tested Woodford shale.

Table 8: 80x80 μm TMS AFM image data.

80 x 80 μm Scan Size			
Image # (polish pad Roughness)	**Ra (nm)**	**Rmax (μm)**	**SAD**
5 (ion milled)	783	7.543	47.20%
6 (0.05)	770	6.479	19.70%
7 (0.05)	811	6.073	18.20%
9 (0.3)	636	5.334	13.20%
10 (15)	471	5.423	14.20%
11 (15)	446	5.22	19.80%

Smaller scan sizes were performed to determine if the exceeding the z-limits in either direction could be reduced. As seen in Figure 43 through Figure 45, even the smaller image sizes result in the tip exceeding the z-limits of the scanner. Though the ion-milled samples seem to have smoother features upon examining the images, the average roughness hardly deviates from that of the least polished (Level 1) sample. A full compilation of the data collected through imaging of the Tuscaloosa Marine shale is found in Table 9.
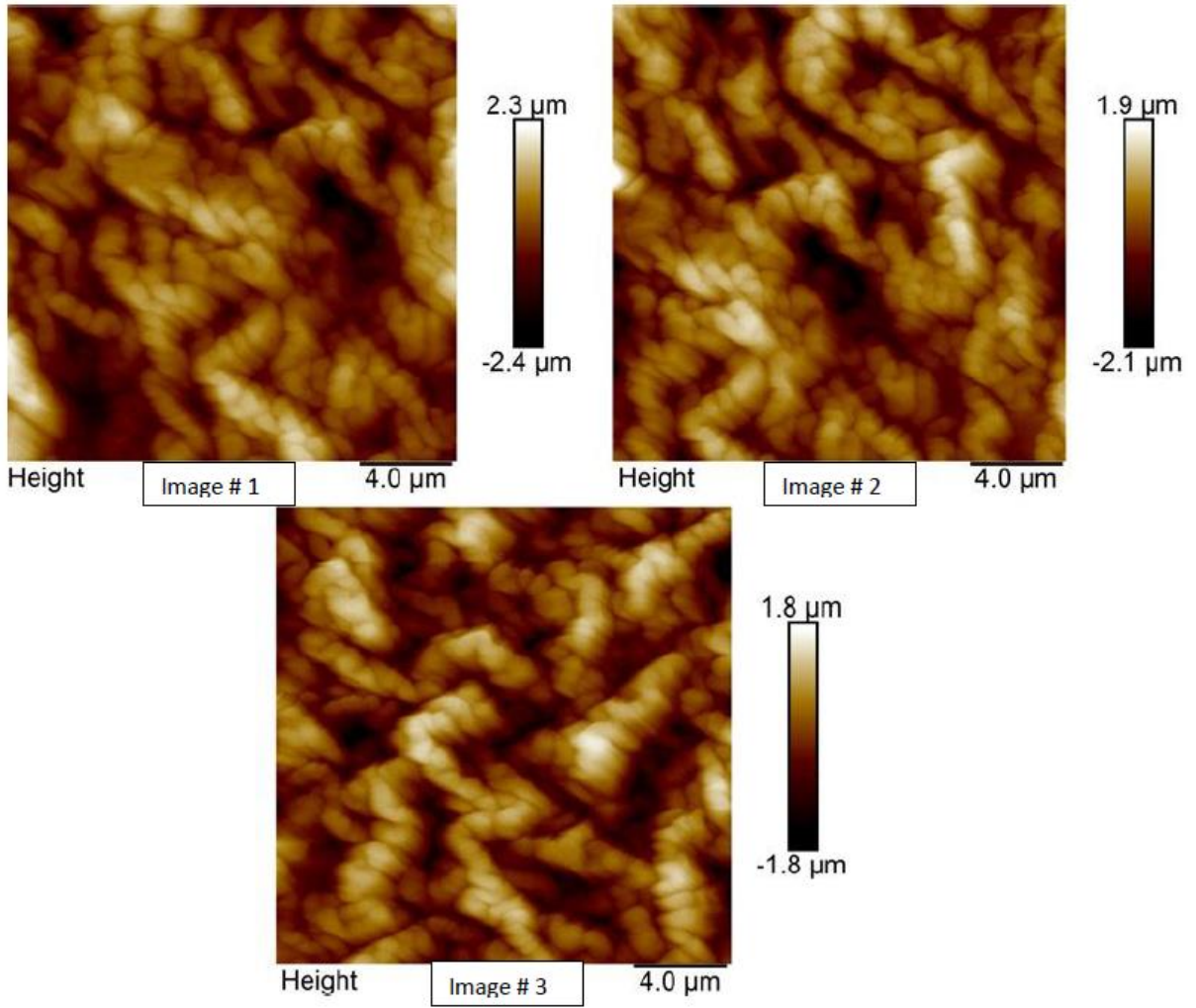
Figure 43: 20x20 μm images of TMS after ion-milling.
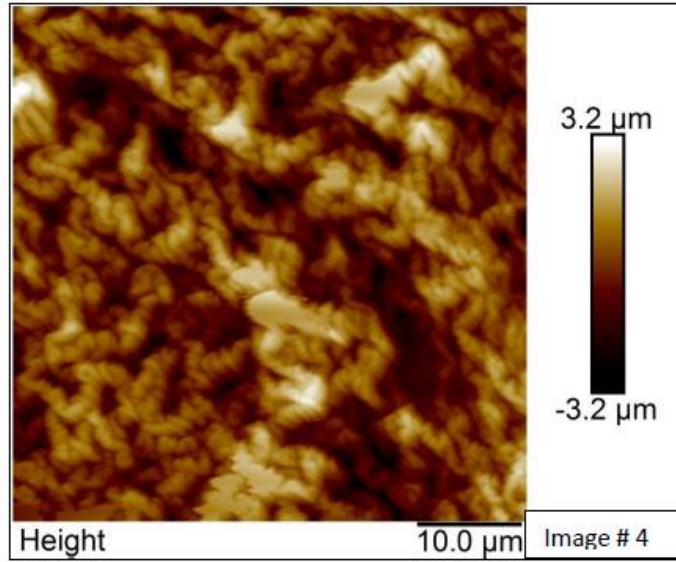
Figure 44: 50x50 μm images of TMS after ion-milling.
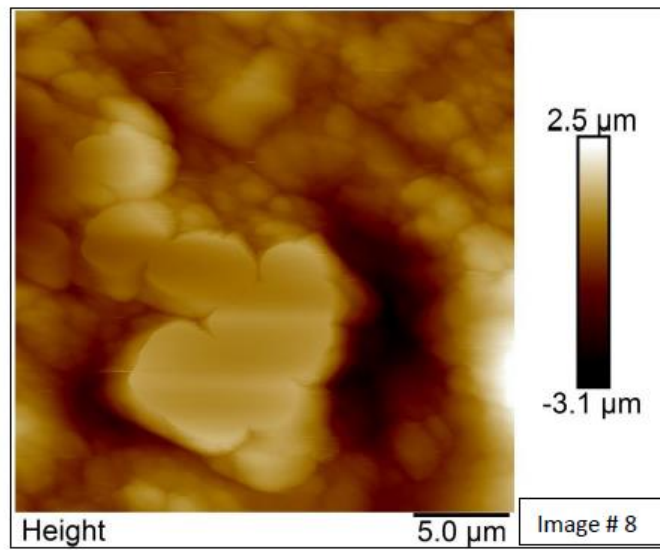
Figure 45: 26x26 μm images of TMS after Level 5 polishing

Table 9: Complete AFM image data for TMS.

Polishing technique	Ion-milled					0.05 µm pad			0.3 µm pad	15 µm pad	
Scan size (µm)	20			50	80	80		26	80	80	
Image Number	1	2	3	4	5	6	7	8	9	10	11
Ra (nm)	539	462	468	782	783	770	811	559	636	471	446
Rq (nm)	677	577	573	960	988	972	995	740	838	591	567
Surface Area	697	706	693	4320	9421	7659	7567	897	7246	7309	7669
Projected Surface Area	406	406	400	2500	6400	6400	6400	706	6400	6400	6400
Surface Area Difference	71.5	73.8	73.2	72.8	47.2	19.7	18.2	27.1	13.2	14.2	19.8
Rmax (µm)	4.555	4.554	3.648	6.263	7.543	6.479	6.073	5.211	5.334	5.423	5.22

Here it can be seen that the roughness values associated with polishing levels 1-5 are very similar between the Tuscaloosa Marine and Woodford shale plays. However, the ion-milled (level 6) samples results for the Tuscaloosa Marine shale is double that of the Woodford shale. Because the average roughness of the ion-milled samples are not significantly different from that of the Level 1 polished samples, samples for nanoindentation and AFM indentation testing will only undergo Level 1 polishing with extreme caution not to induce additional damages to the samples. This will also allow for the greater retaining of organic content and soft composites found within the shale.

3.3 Comparison of Indentation Results for Woodford and Tuscaloosa Shales

Preliminary nanoindentation testing of the Woodford shale has previously been performed by the University of Mississippi NIRG. For this testing, a 5x5 indentation grid was

established resulting in 25 indentation results. The testing parameters applied can be found in

Section 2.1.6. The results of this analysis are displayed in Figure 46 and Table 10. The reported

values are averaged values of all data collected from nanoindentation testing.
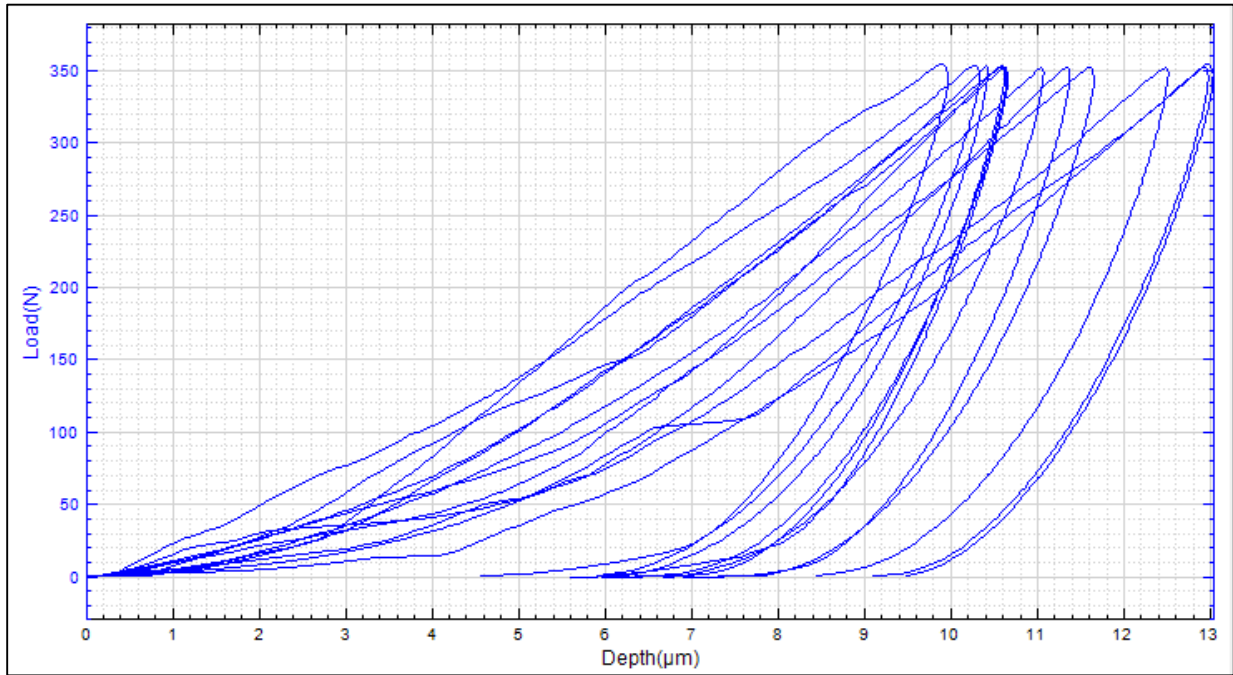
Figure 46: TYP load vs. displacement curves for Woodford shale nanoindentation testing.

Table 10: Woodford shale nanoindentation results.

Location	Max Depth (µm)	Hardness (GPa)	Hardness (HV)	Elastic Modulus (GPa)
Woodford	12.33±1.0	0.16±0.03	14.91±3.1	2.89±0.32

The results obtained from nanoindentation of the Woodford shale is noticeably lower

than previous research has determined them. However, there is sound reasoning that the

increased level of polishing performed in previous studies caused an extraction of organic and

soft material components within the shale type. Due to the low standard deviations in these

results, it can safely be assumed that the properties found are accurate for reporting and use

comparatively with Tuscaloosa Marine shale.

To begin comparison of Woodford and Tuscaloosa shale, a single indent was imaged using atomic force microscopy and then displayed side by side as Figure 47 shows.
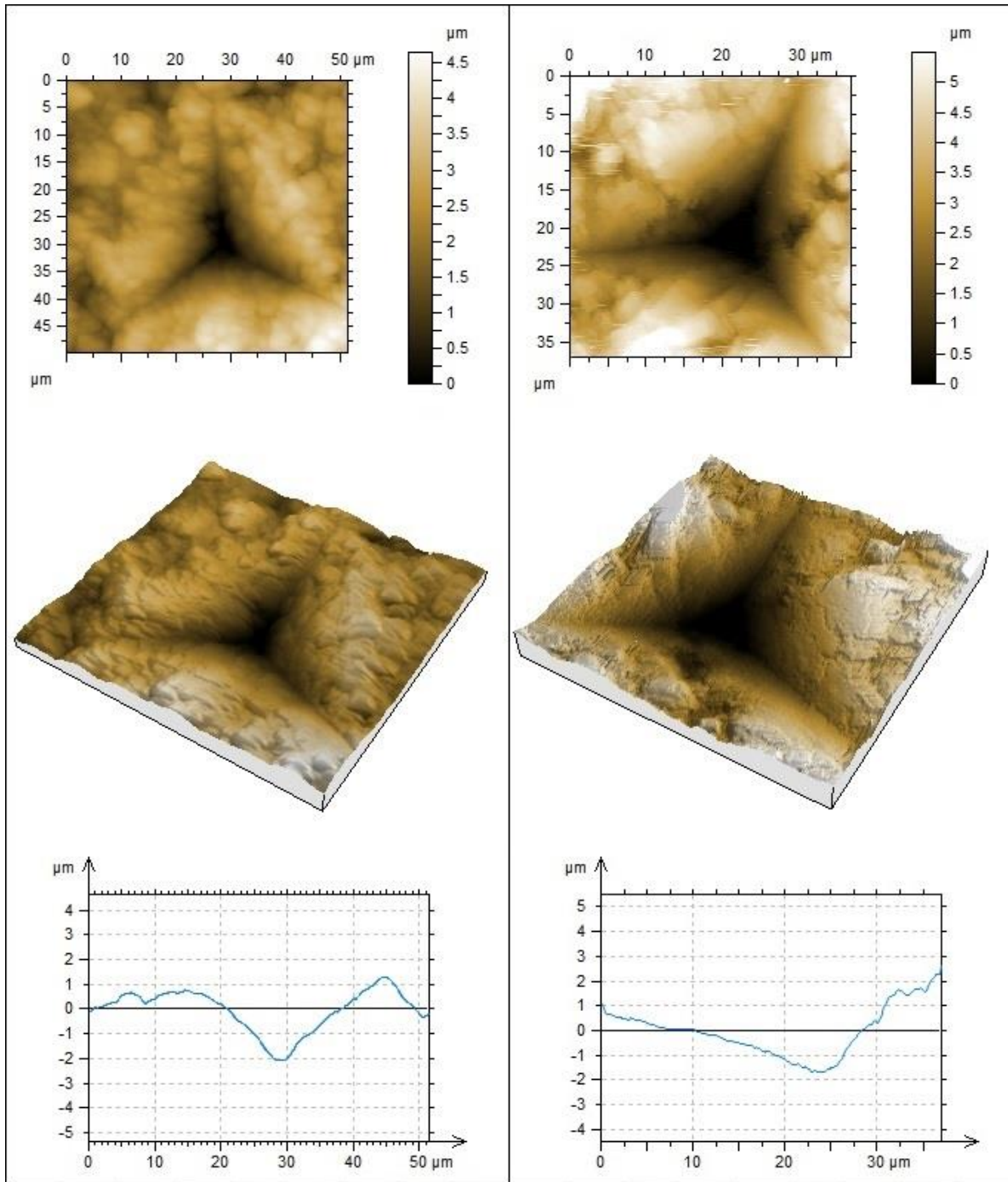
Figure 47: 2D & 3D AFM image and section profile of one nanoindent on the Woodford shale (left) and Tuscaloosa Shale (right).

Upon imaging, it can be seen that the residual impression left within the Tuscaloosa Marine shale is much larger than the one in the Woodford shale. 40 tests were taken from the testing of each sample resulting in 80 total tests analyzed per each measured depth. Combining this data, a total of 1200 values are obtained for determining the elastic modulus and hardness, along with various other properties. Figure 48 displays the elastic modulus values for each respective indent made per measured depth.
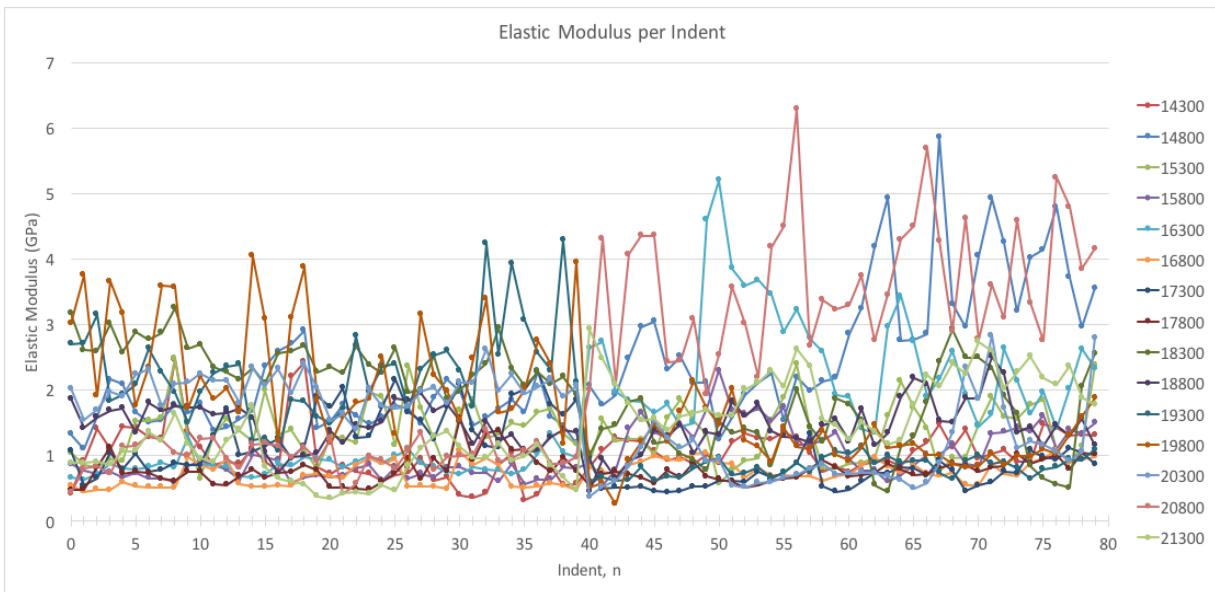
Figure 48: Elastic modulus values per indent. Representative for all 15 sample depths.

In order to reduce the amount of scatter associated in Figure 48 and create a more representative plot corresponding to each respective measured depth as a whole value, the average value of each 80 indentation sets was taken. Now that we have associated a single elastic modulus value with each measured depth, the same procedure was completed for both the hardness and maximum indentation depth (Figure 50 through Figure 53). The red base-line seen within each of these figures represents the mean value obtained from all 1200 indentations.
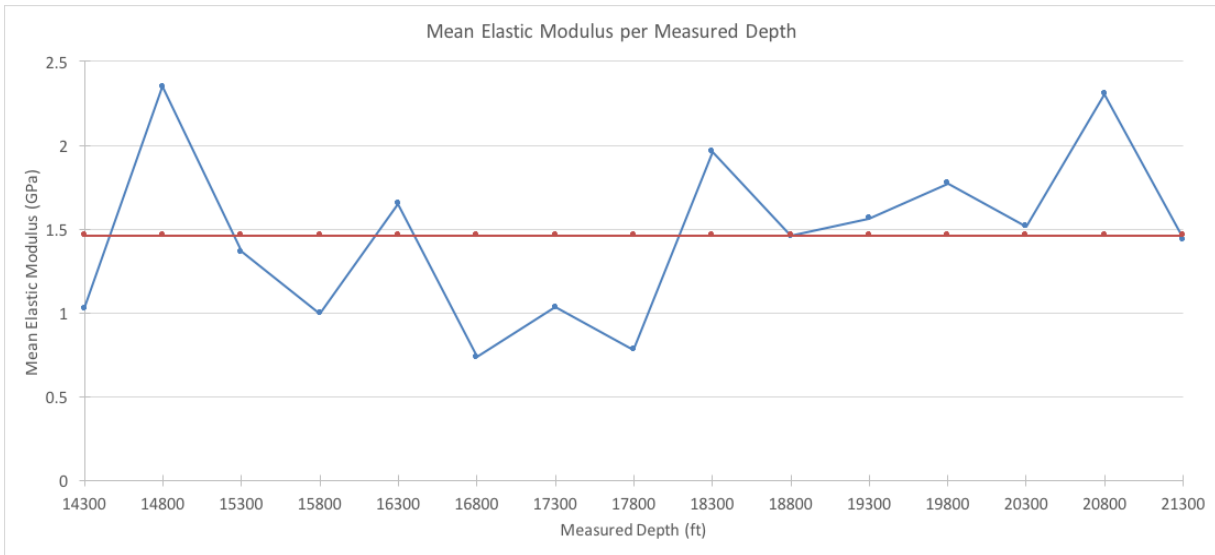
Figure 49: Mean elastic modulus values corresponding to respective measured depth.
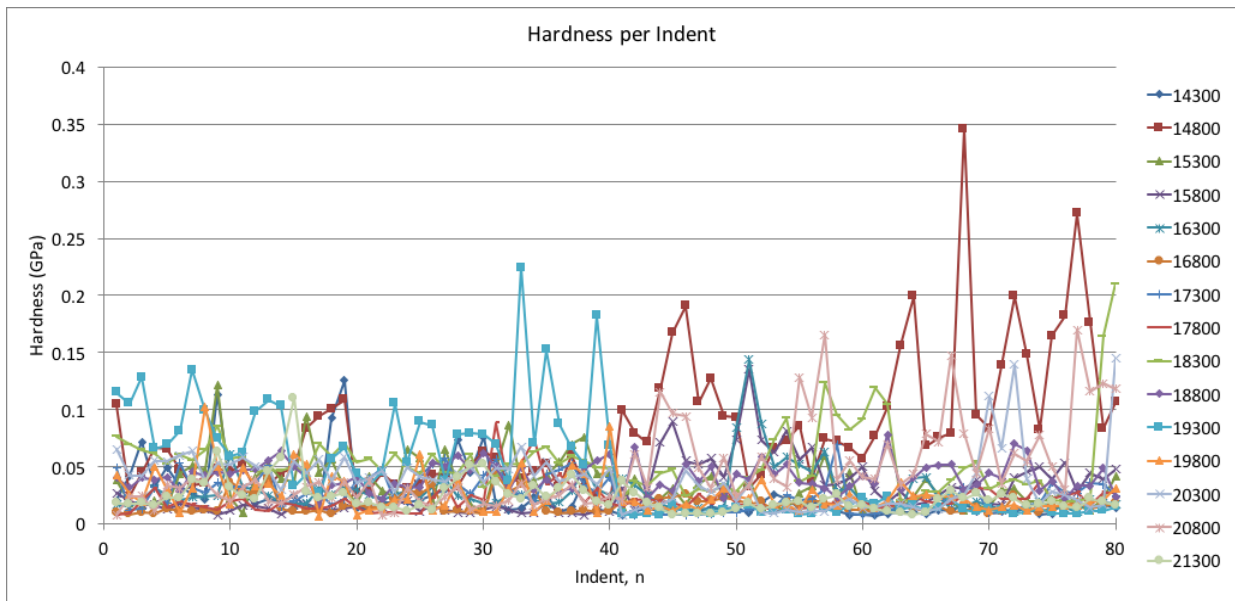
Figure 50: Hardness values per indent. Representative for all 15 sample depths.
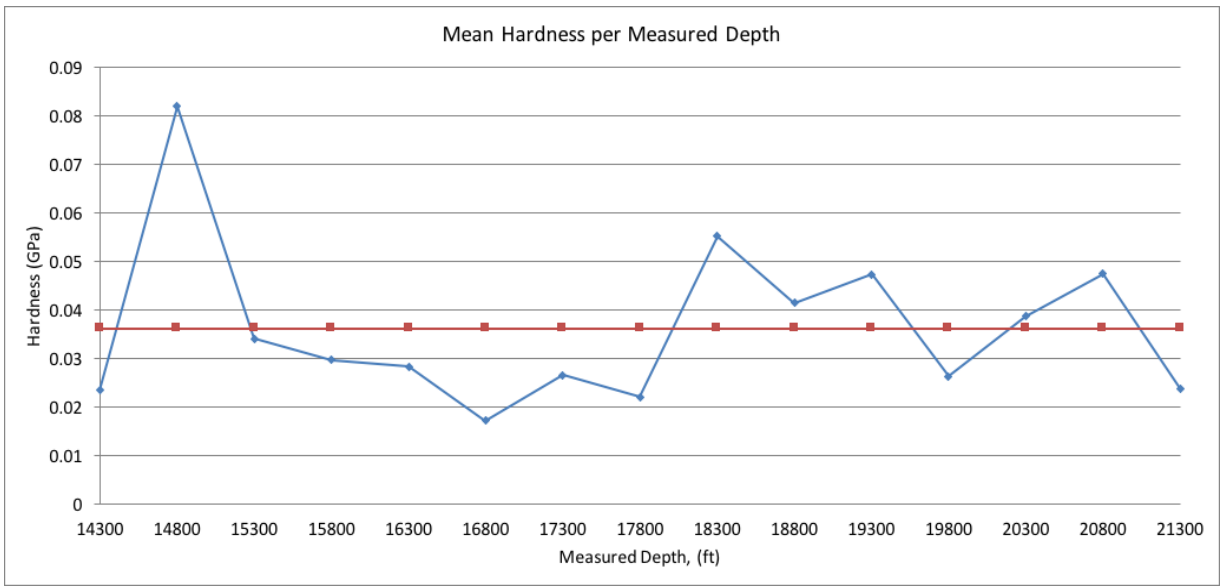
Figure 51: Mean hardness values corresponding to respective measured depth.
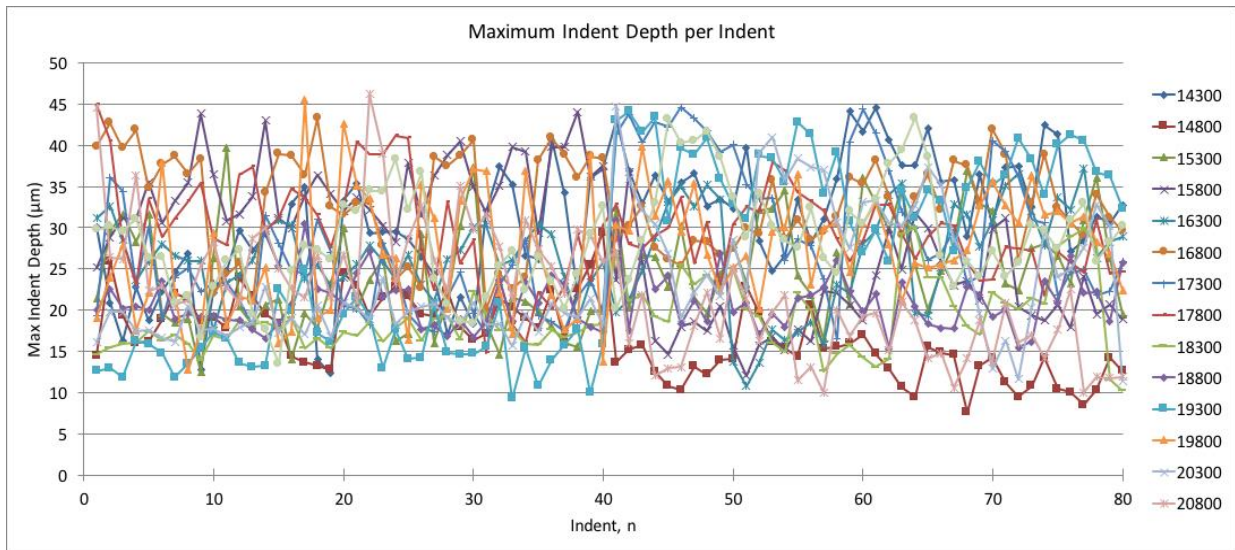
Figure 52: Max indentation depth values per indent. Representative for all 15 sample depths.
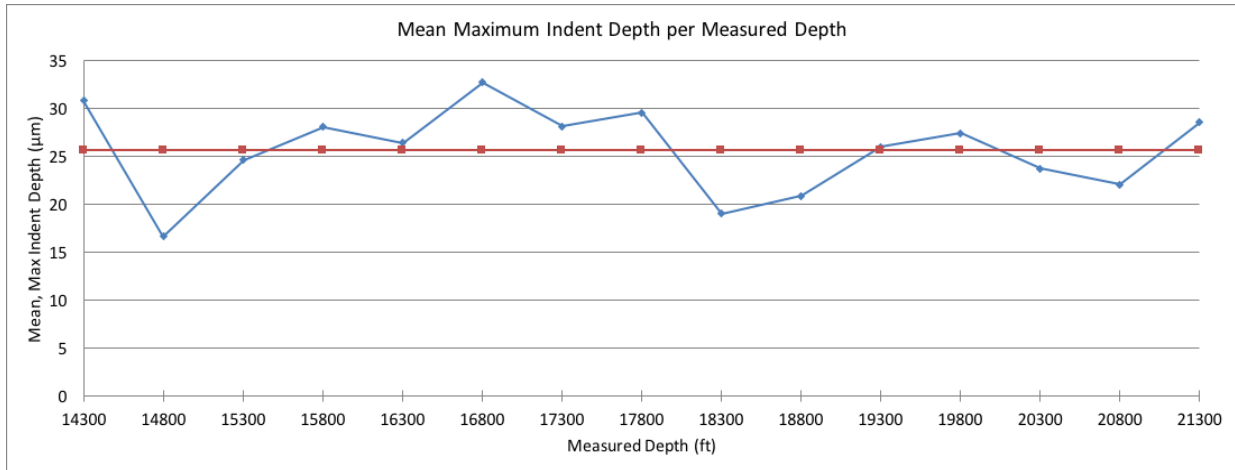
Figure 53: Mean Max indentation depth values corresponding to respective measured depth.

The relationships seen in these figures are to be expected as the maximum indent depths should increase for a sample with low hardness and modulus values and vice versa. Also, it can be seen that most specimens found within their respective measured depths along this well correspond closely to one another.

The next step is to create a means of determining the mechanical properties in relation to a given indentation depth. It is already known, though, that the relationship between material hardness and indenter displacement within a sample is based on a power function. To analyze this, Figure 54 shows a crossplot of the hardness values corresponding to indentation depth. Additionally, the frequency of obtaining a given value based on indentation depth is given. Since the relationships between hardness and elastic modulus have been previously defined and analyzed, determining values and relationships of one will allow for easy quantification of the other. For this particular portion of the study, the hardness was selected for analysis.
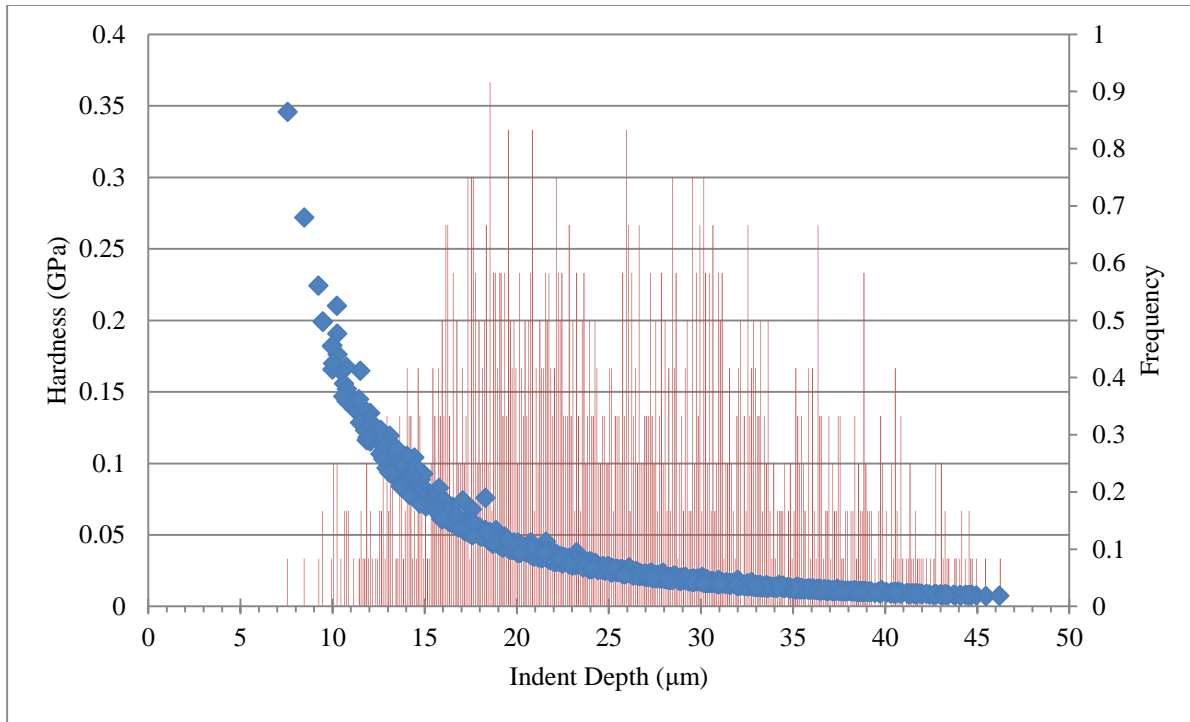
Figure 54: Hardness vs indentation depth (blue) with corresponding frequency (red) (bin size =0.1).

To determine the goodness of fit within this data set, multiple probability distribution functions were applied (Figure 55) and the corresponding coefficients are:

Table 11: Goodness of fit values for fitting hardness (GPa) values.

Distribution	Parameters			Goodness Of Fit Rank
Beta	$\alpha_1 = 2.67$		$\alpha_2 = 12.35$	2
	$a = 6.63$		$b = 82.12$	
Normal	$\sigma = 7.24$		$\mu = 20.04$	3
Gamma (3P)	$\alpha = 3.84$	$\beta = 3.75$	$\gamma = 5.64$	1
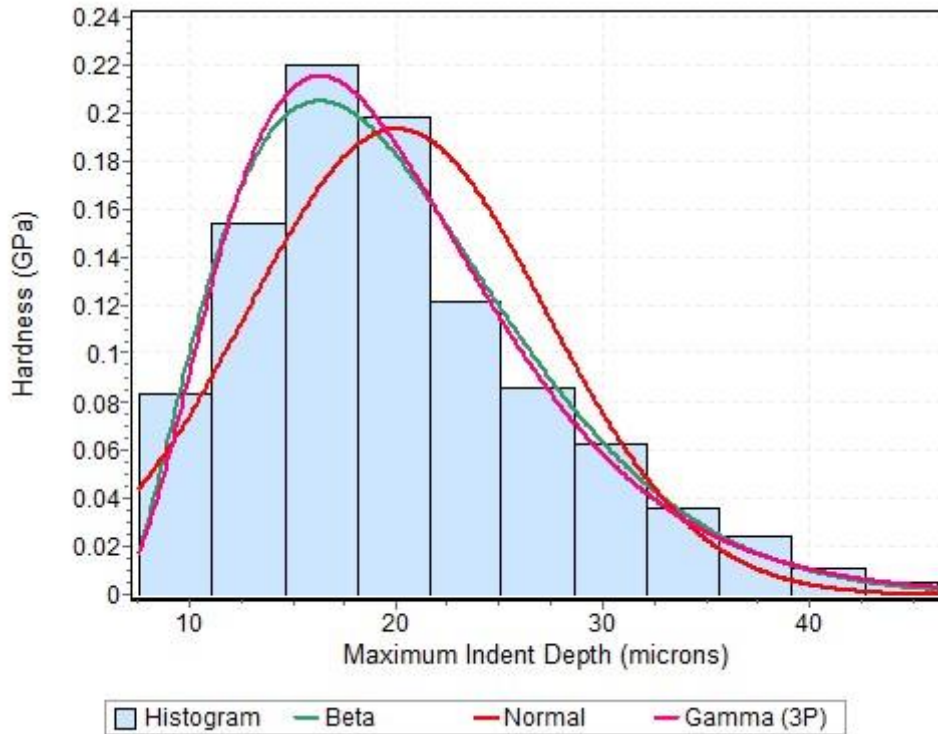
Figure 55: Probability distribution function plot to determine the goodness of fit within the data sets.

Another mode of analysis is to determine which characteristic properties affect another most significantly. This analysis is done first by crossplotting each property attained through nanoindentation testing (i.e. elastic modulus, hardness, and maximum indentation depth). The data was first analyzed by methods of linear regressions as found in Figure 56 through Figure 58 in order relate the coefficients of determination to those obtained in previous research.
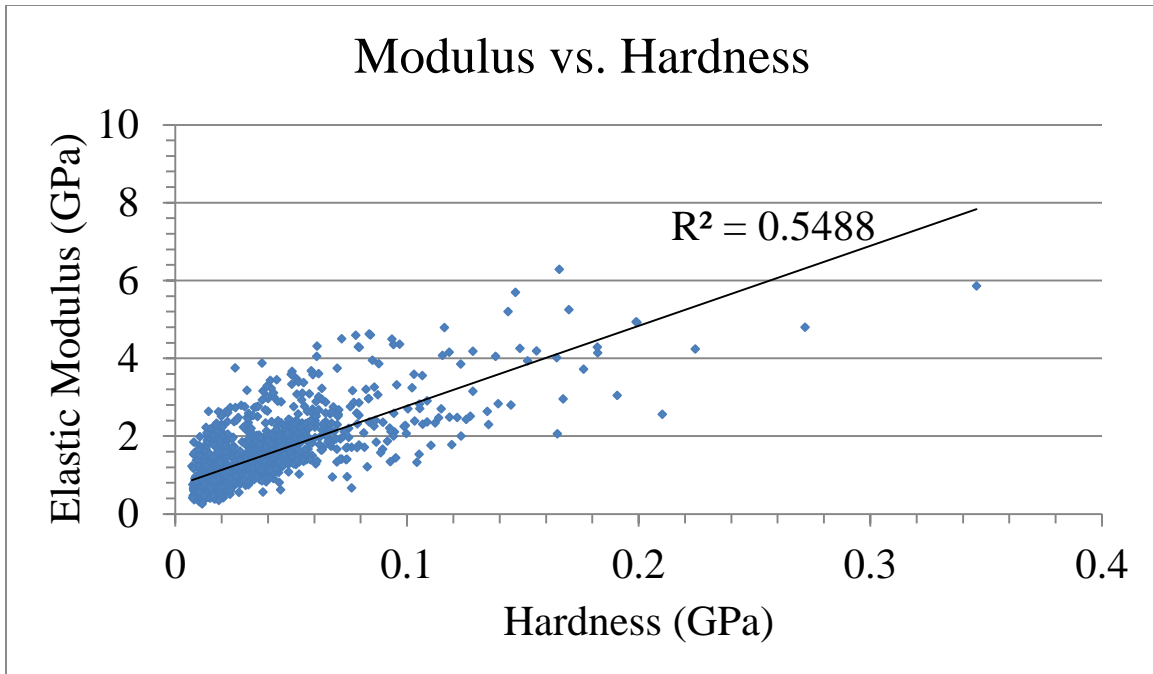
Figure 56: Linear correlation between elastic modulus and hardness values of TMS.
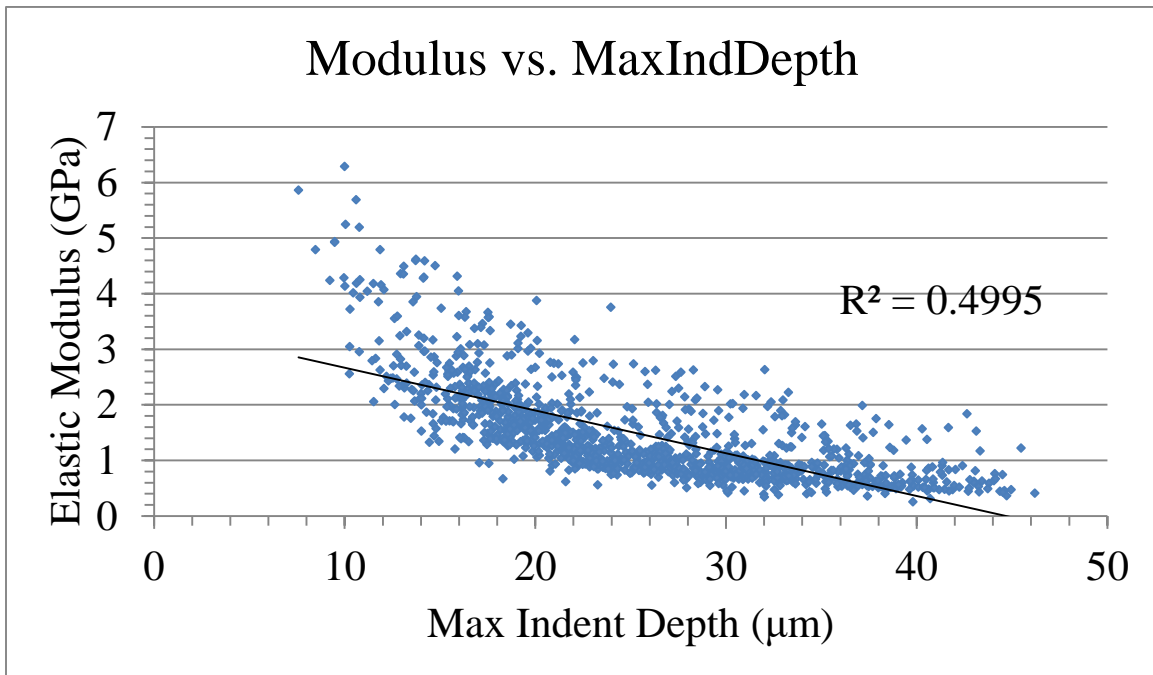
Figure 57: Linear correlation between elastic modulus and maximum indentation depth values
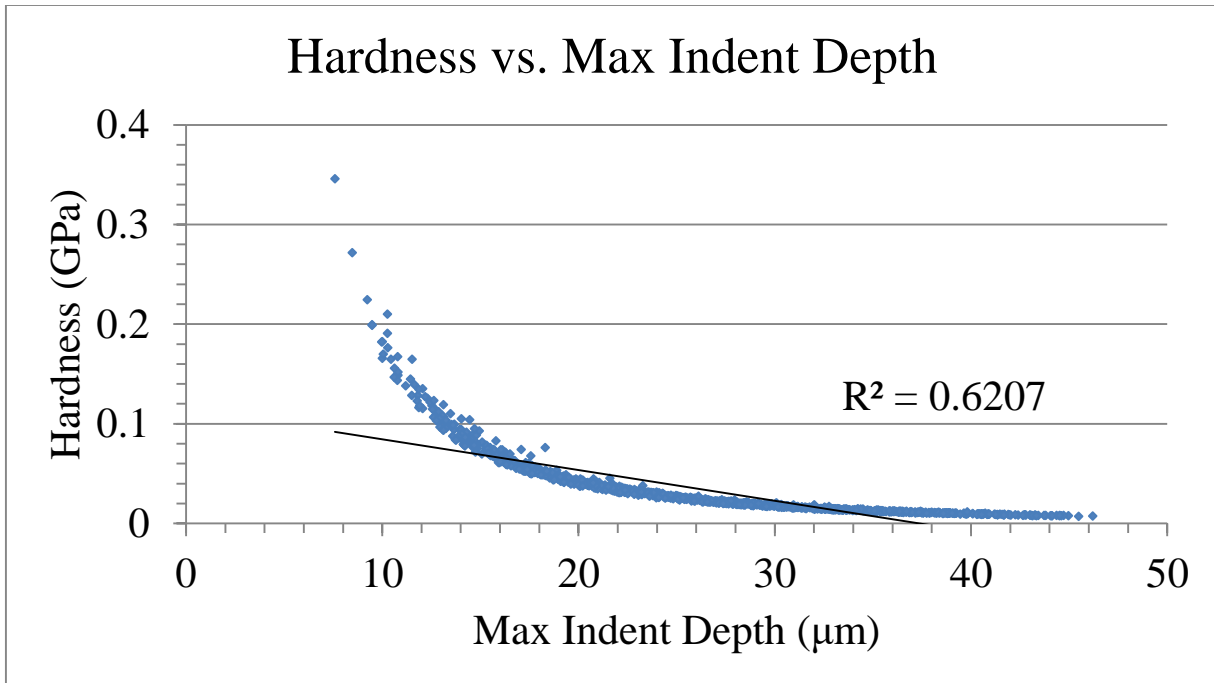
of TMS.

Figure 58: Linear correlation between hardness and maximum indentation depth values of TMS.

Much like previous studies, linear regression models result in low values. However, the Tuscaloosa Marine shale seems to result in having much higher coefficient of determination values than that of other shale types. Though this is true, the same correlations were plotted again, only this time using a power function to fit the data as the relationships are created through a series of power law functions as discussed previously. These new fits (Figure 59 and 60) can be seen to have significantly higher coefficients of determination which validates the data indeed follows a power function relationship. Hardness versus elastic modulus correlation was not re-analyzed as the relationship between the two only showed an increase of approximately 0.02.
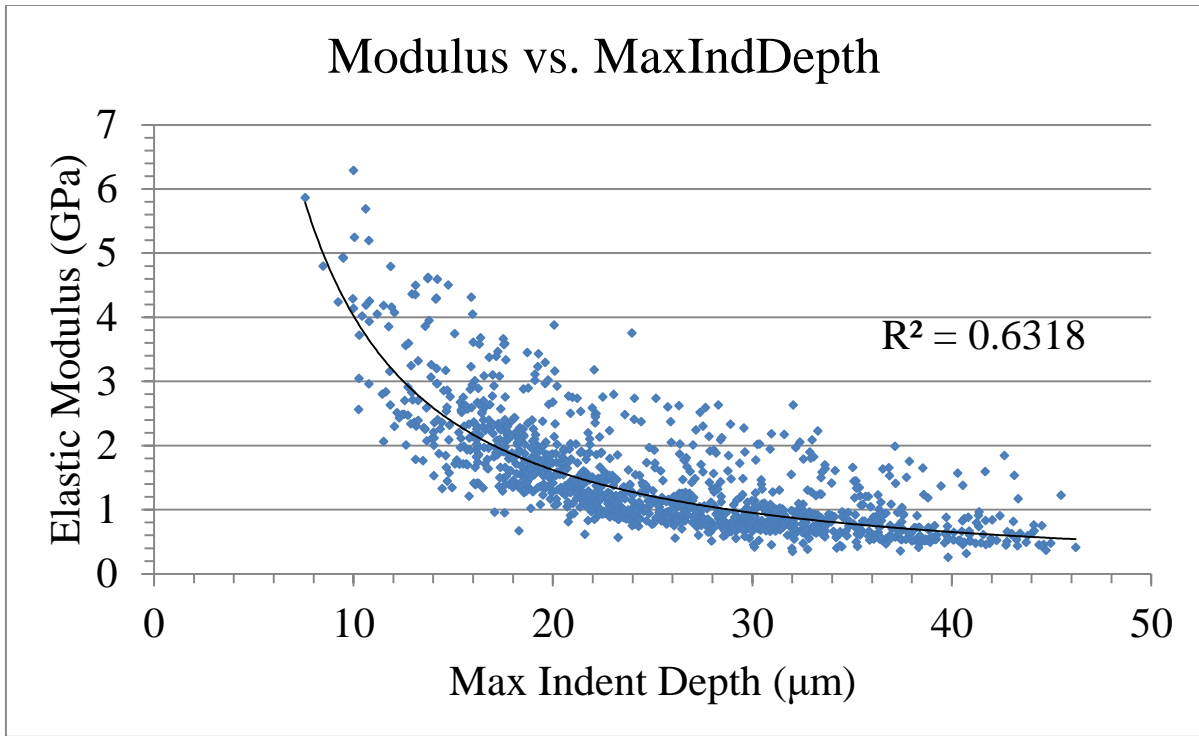
Figure 59: Power correlation between elastic modulus and maximum indentation depth values of

TMS.
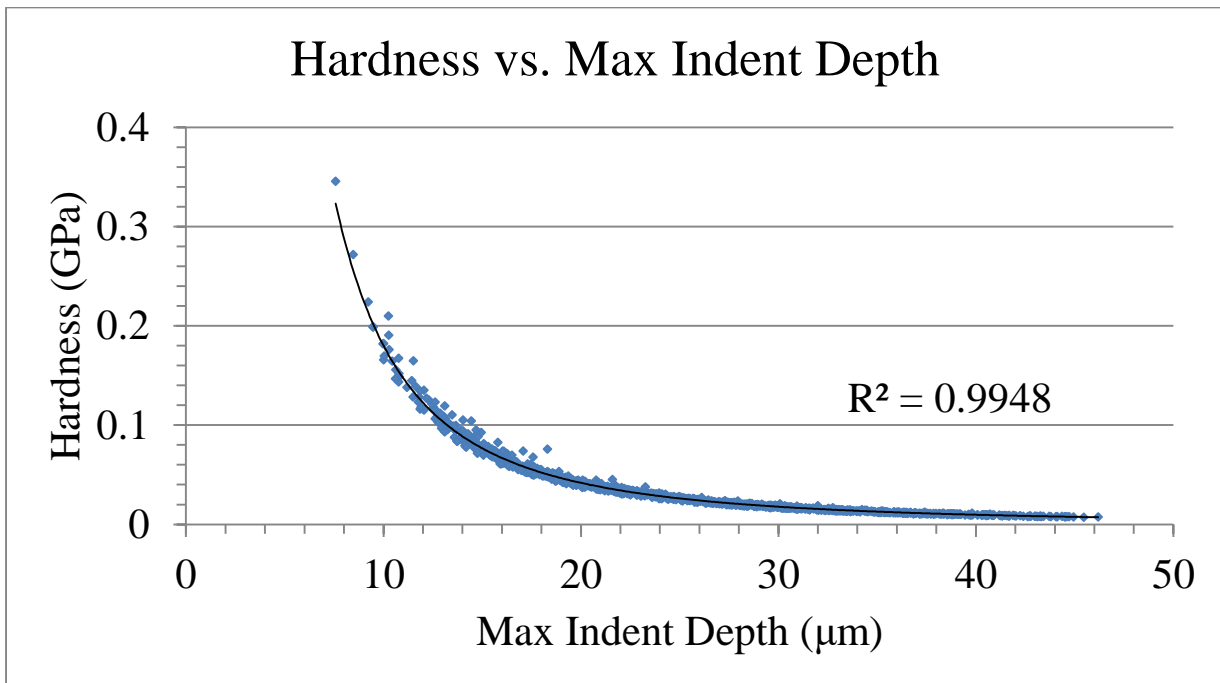
Figure 60: Power correlation between hardness and maximum indentation depth values of TMS.

The final step in determining which values affect others more significantly is to run a full correlation analysis comparing the maximum indentation depth, hardness, elastic modulus as well as measured depth. Through this method, the following annova table (Table 12) was created. This shows for the extracted properties from nanoindentation testing, there is not a strong correlation to the location among the drilling well (measured depth). Though it is noted that the elastic modulus is the only one of the three properties that shows a positive correlation to measured depth.

Table 12: Correlation analysis for TMS of maximum indentation depth (μm), hardness and elastic modulus (GPa) and measured depth (well length, ft).

	Max Depth (μm)	Hardness(GPa)	Elastic Modulus(GPa)	Measured Depth (ft)
Max Depth (μm)	1			
Hardness(GPa)	-0.787829196	1		
Elastic Modulus(GPa)	-0.706766113	0.74079959	1	
Measured Depth (ft)	-0.046307338	-0.029387561	0.150427557	1

Lastly, because correlation testing did not yield desired results, a study of the amount of indentations necessary to obtain reliable data was performed. To do this, the results of each 80 indentation data sets were analyzed by a running average method to determine at what number of indentations reliable results are obtained. Figure 61 shows a select few of these analyses based on the distribution patterns found within the data for the elastic modulus. Likewise, Figure 62 displays these results for hardness values for the same samples selected and displayed in Figure 61. The remaining results for running averages of elastic modulus and hardness, not displayed in these figures can be found in Appendices A and B respectively.

A.1

B.1
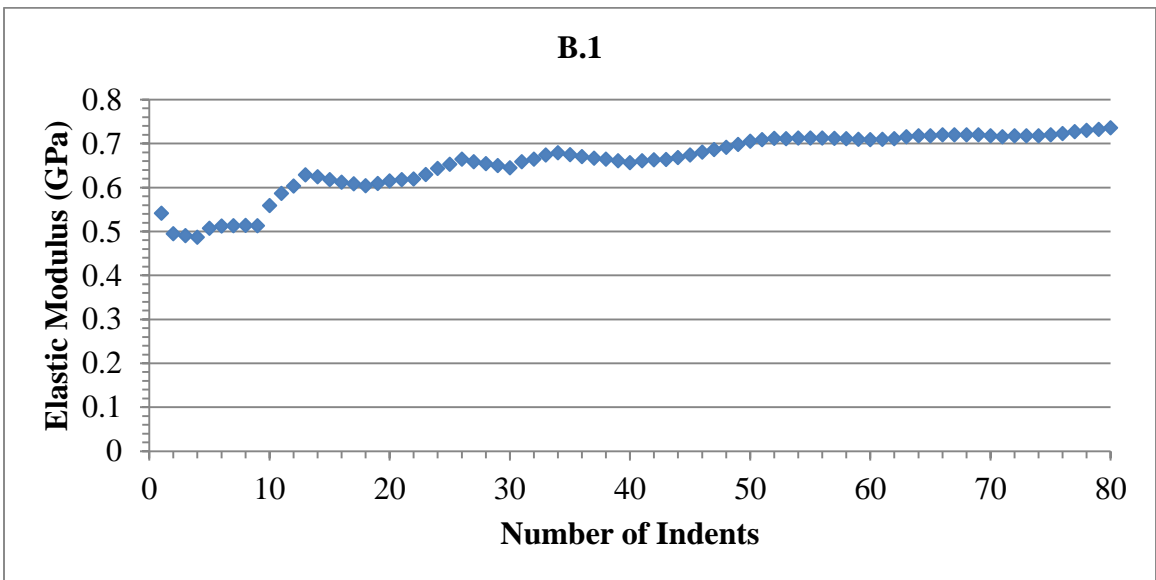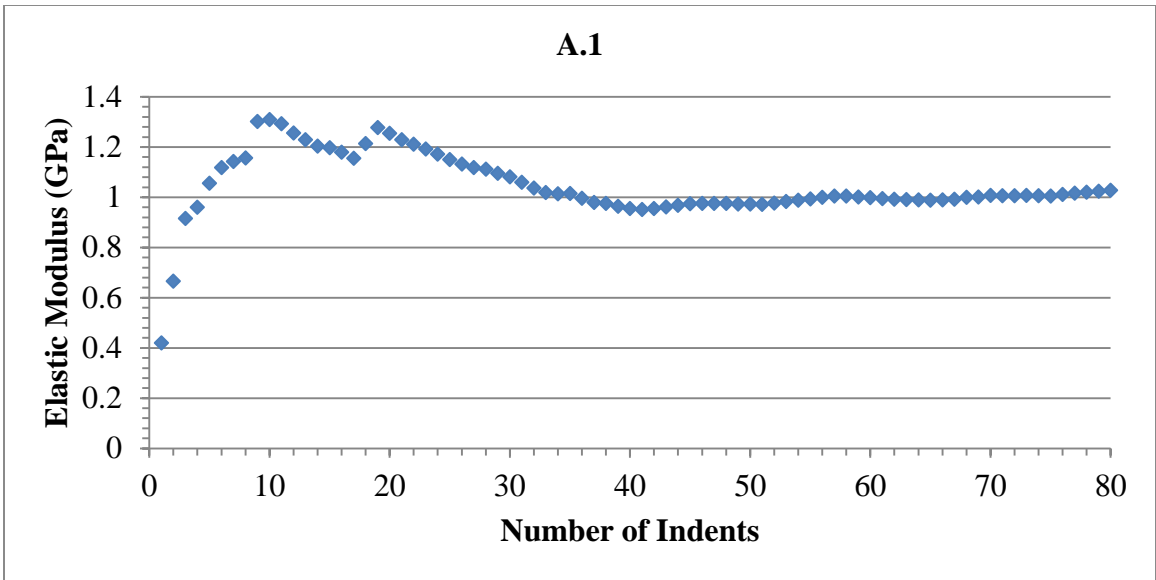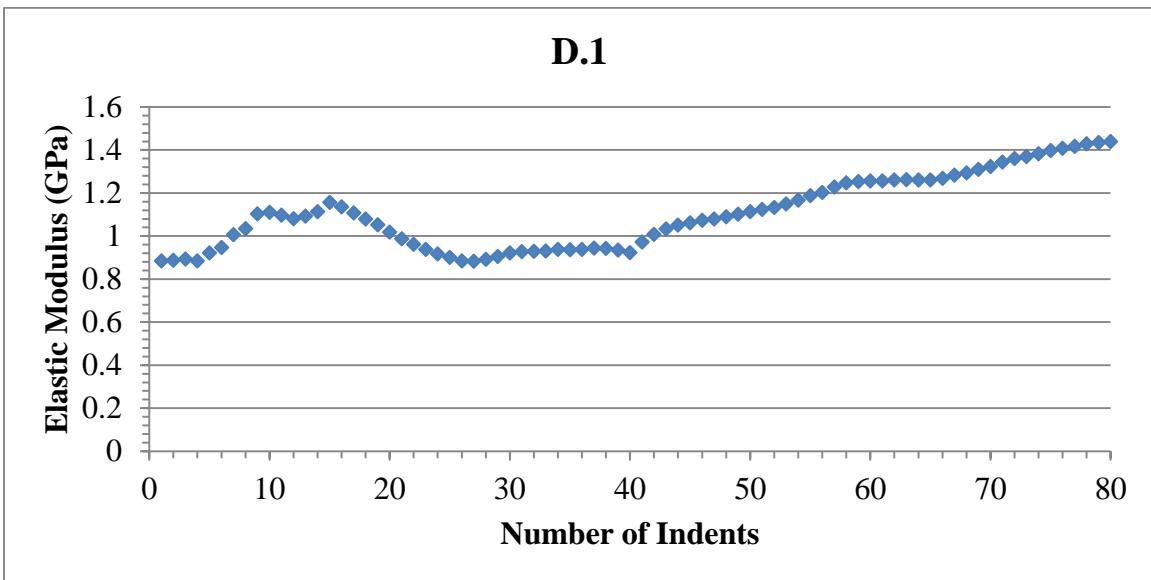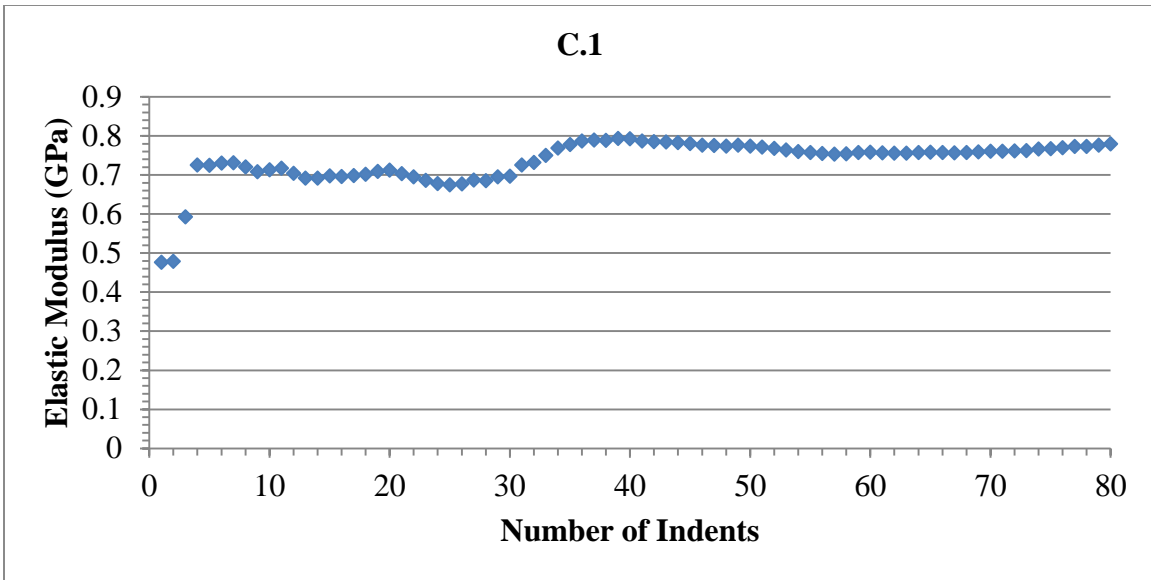
Figure 61: Running average for elastic moduli at measured depths A.1) 14300, B.1) 16800, C.1) 17800, and D.1) 21300.
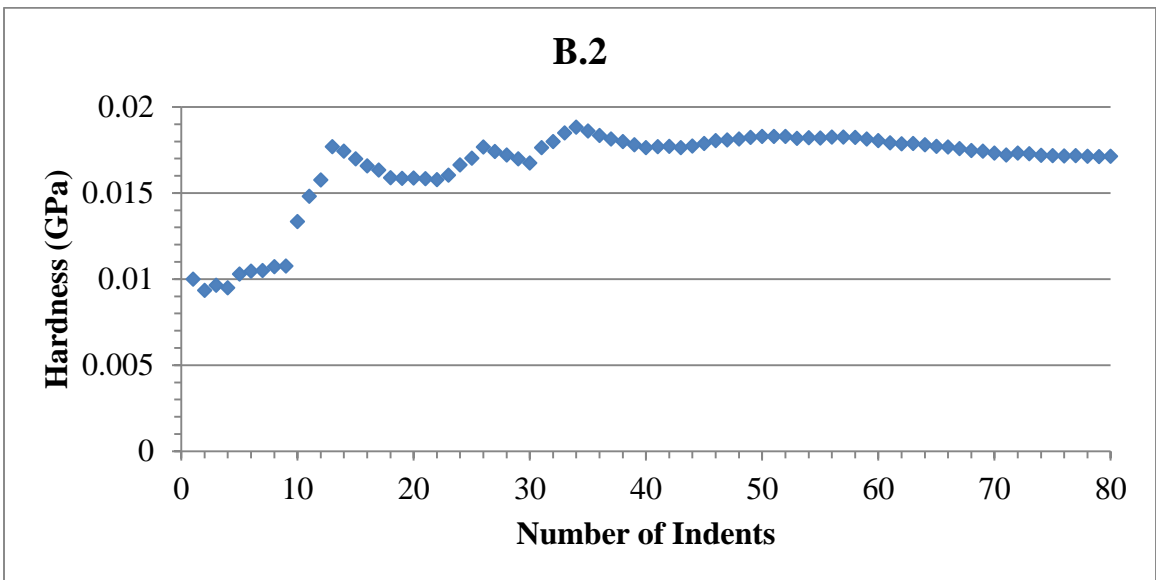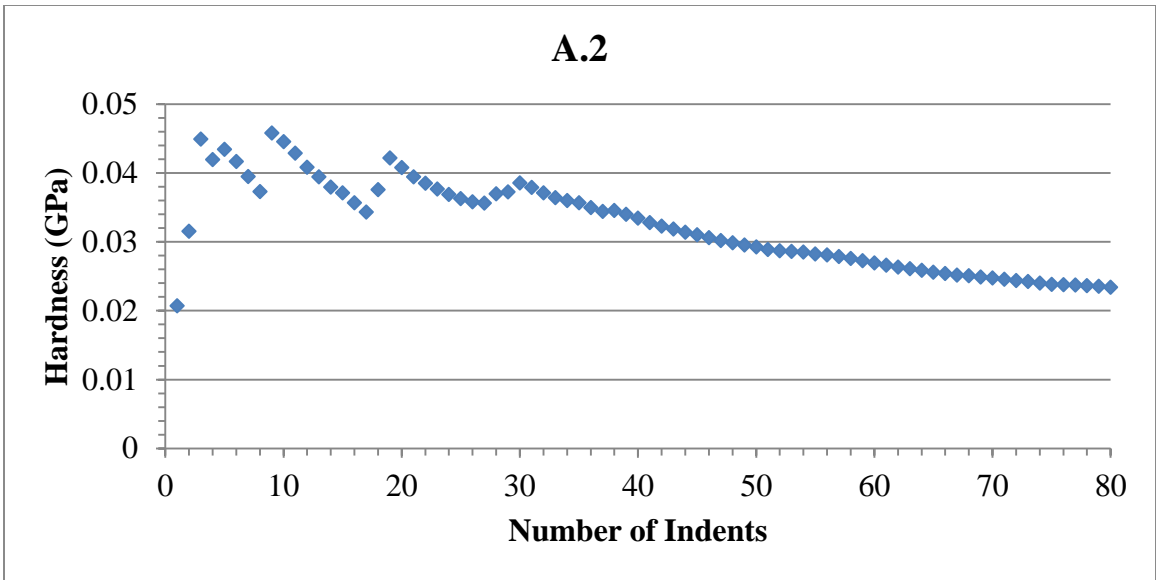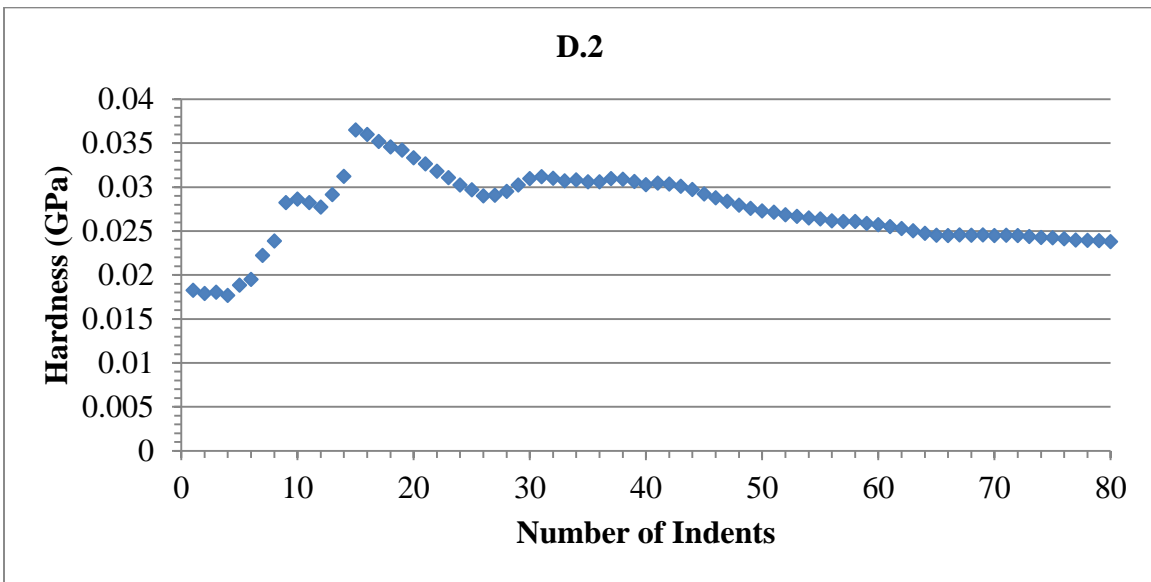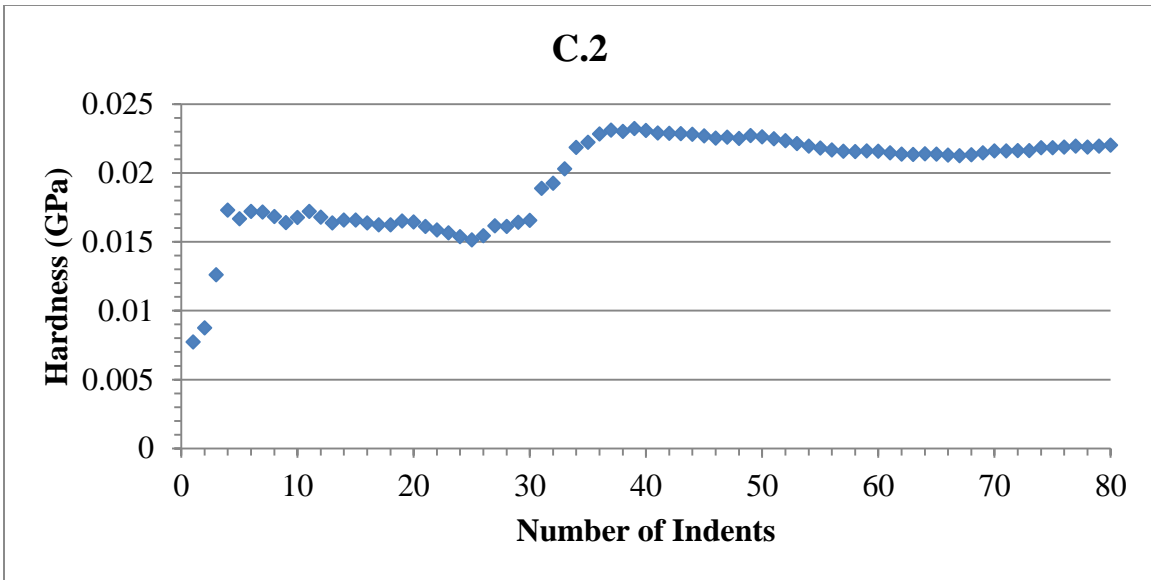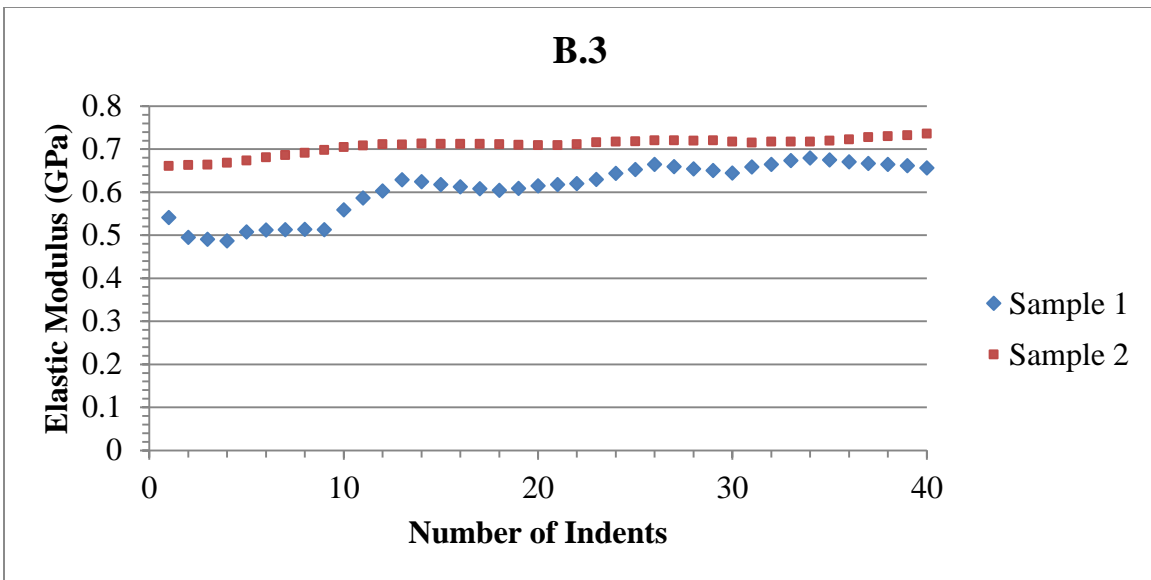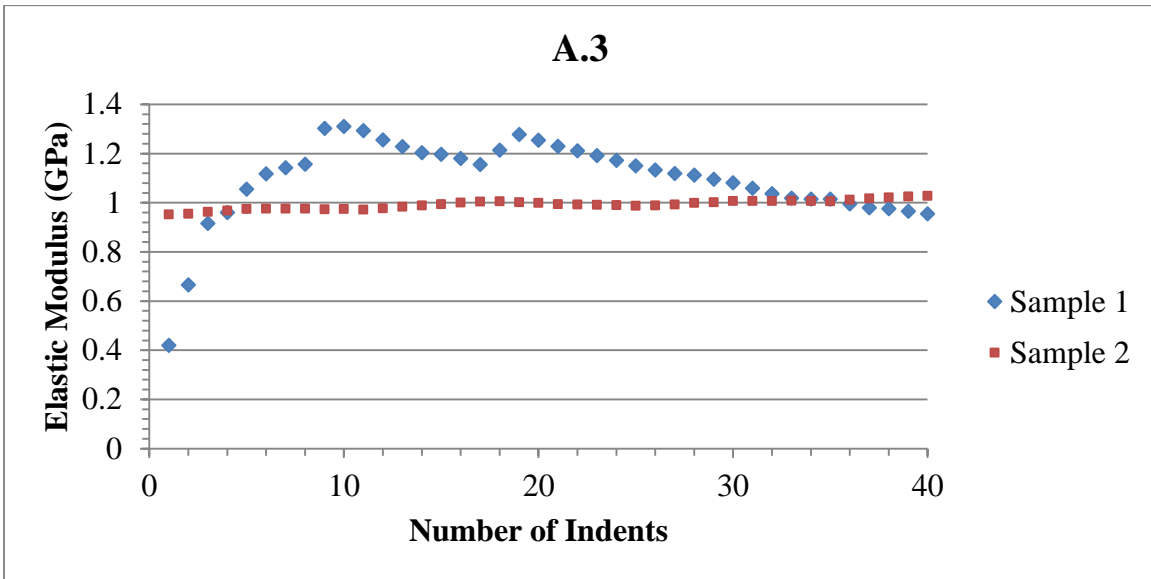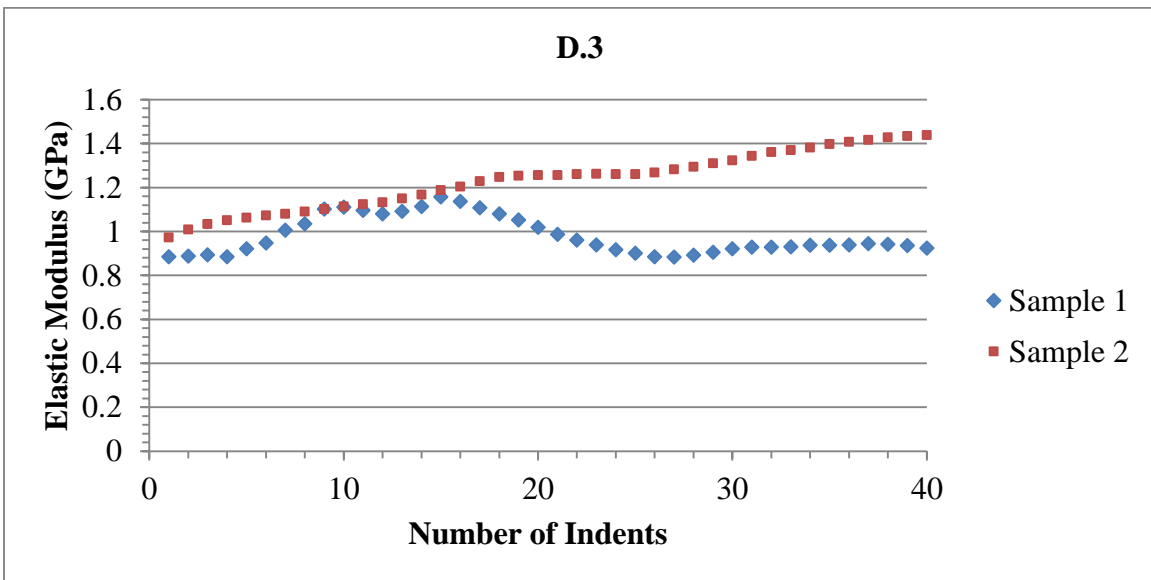
Figure 62: Running average for hardness at measured depths A.2) 14300, B.2) 16800, C.2)

17800, and D.2) 21300.

The previous two figures show that for both the hardness and elastic modulus, there is a distinct

change in the data around 40 indentations. However, this is not unexpected since 40 of the total

80 indentations are taken from separate samples. To better understand this, each set has been

broken down into running averages for each sample individually. These relationships can be seen in Figure 63 and 64.
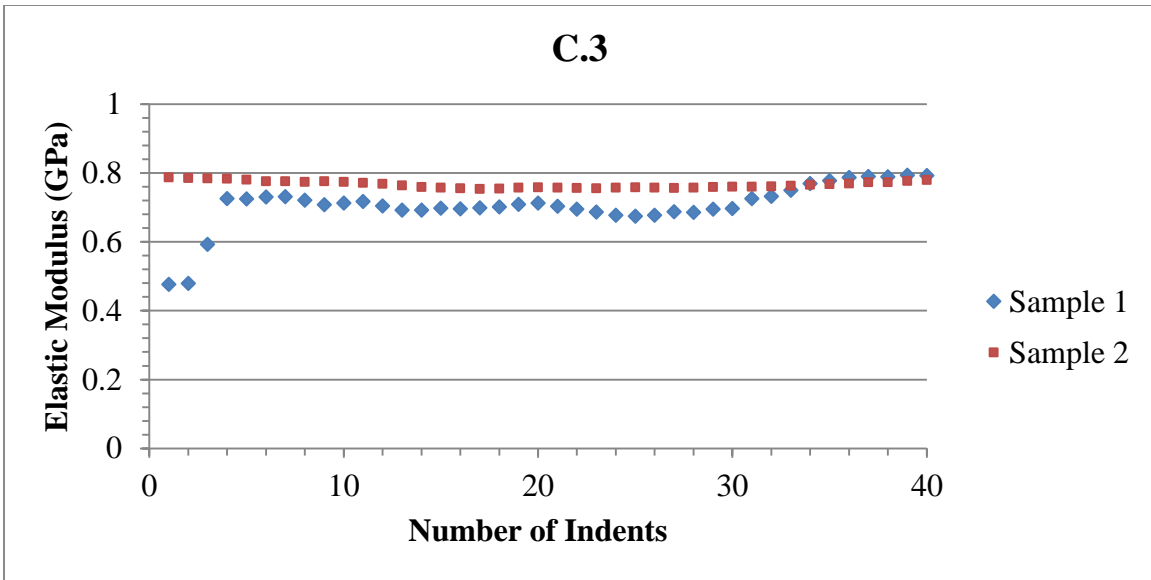
Figure 63: Running average for elastic moduli at sample depths A.3) 14300, B.3) 16800, C.3) 17800, and D.3) 21300 separated by sample number.

A.4

B.4
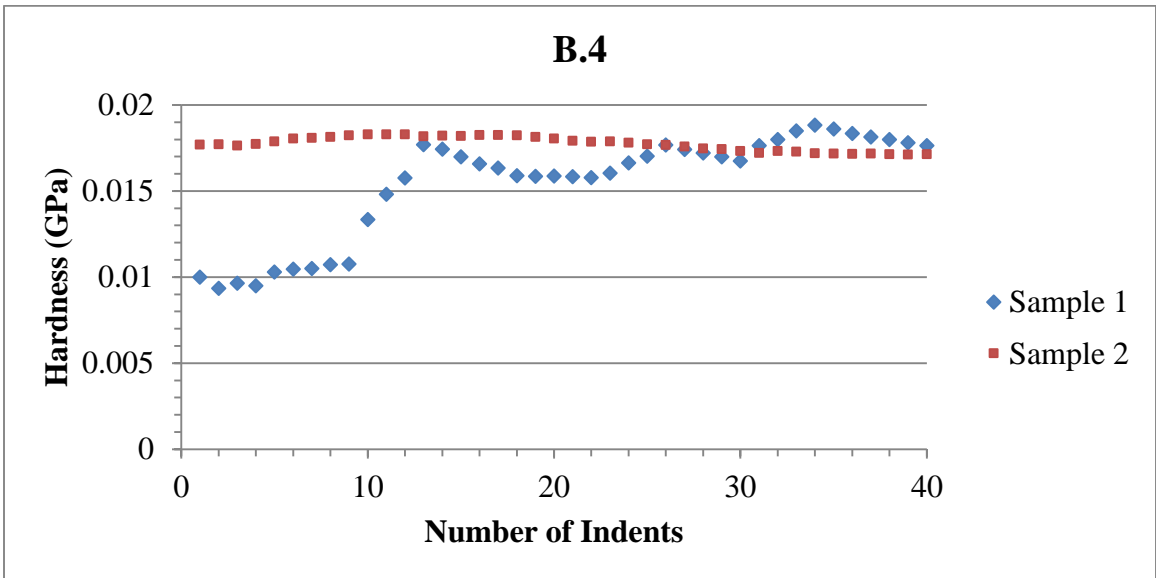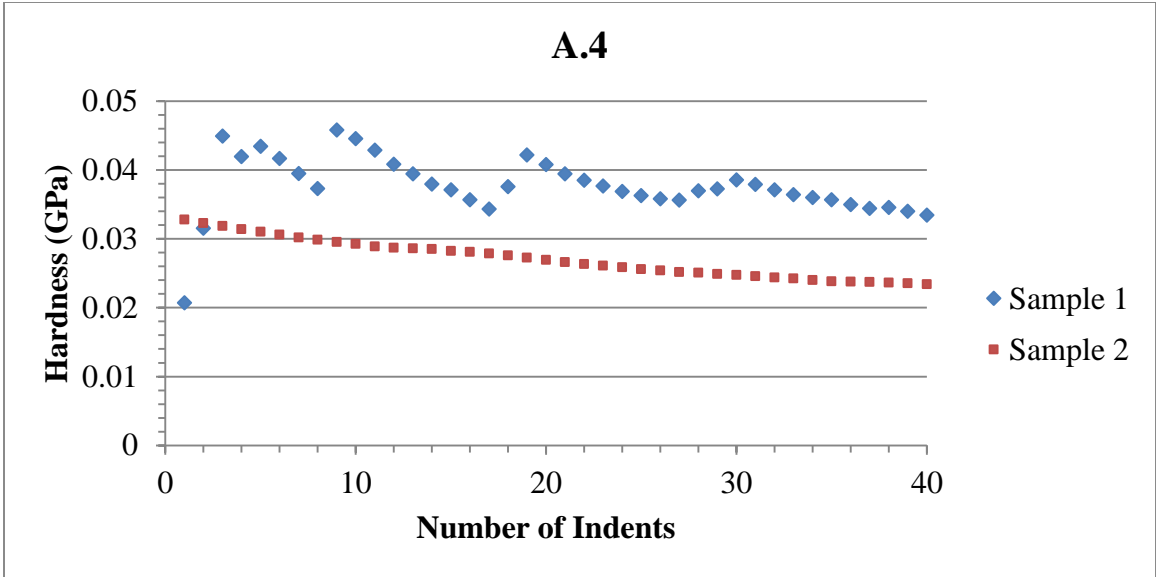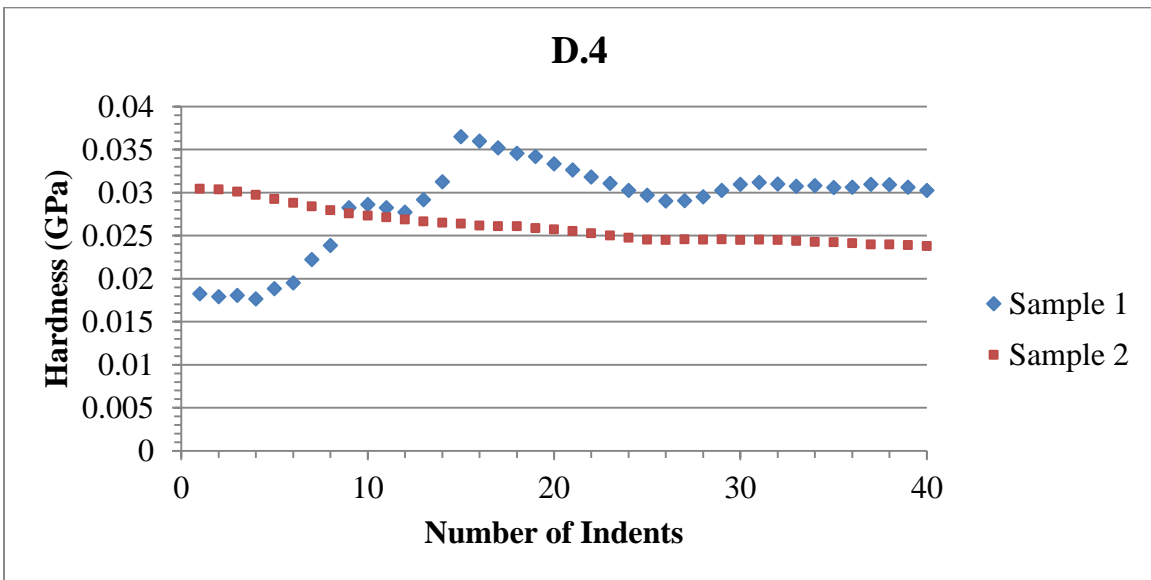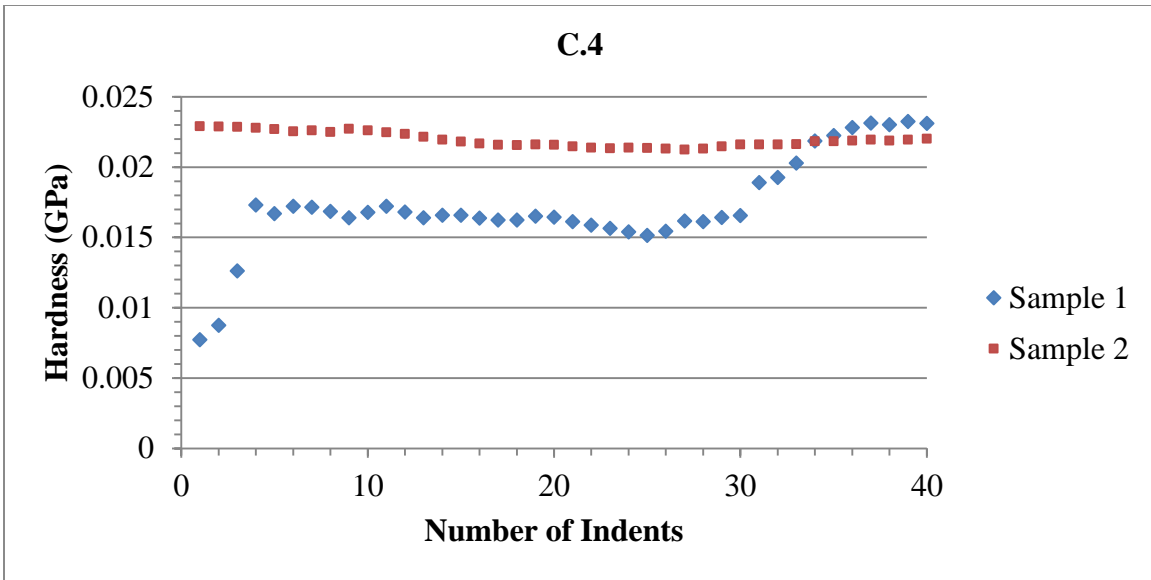
Figure 64: Running average for hardness at sample depths A.4) 14300, B.4) 16800, C.4) 17800, and D.4) 21300 separated by sample number.

Peculiarly, sample set 2 yielded much more desirable results. Though sample set 1 does not show as much consistently between each indentation as sample set 2 does, it can still be seen that for the majority of the samples tested, 40 indentations is sufficient in yielding reliable data.

As expected, the number of indentations required to yield steady results varies with change in the measured depth. This is believed to be due to the complex heterogeneity of the shale. Jumps found within the running average models are considered to be points where successive indentations were made upon two separate, or transitioning, shale composites such as kerogen to calcite or clay materials. This is most noticeable in sample set 1 of measured depth 14300.

Since the data is in good agreement with previous research findings as well as expected results, final determination of the Tuscaloosa Marine shale's mechanical properties are listed in Table 13.

Table 13: Mean values and standard deviations for maximum indentation depth, hardness and elastic modulus for TMS.

Location	Max Depth (µm)	Hardness (GPa)	Hardness (HV)	Elastic Modulus (GPa)
Tuscaloosa	25.62±8.1	0.036±0.03	3.41±2.9	1.46±0.88

Comparing the resulting values as representative values for the shale material as a whole to that of the Woodford shale, it can be seen that there is significant difference in the shale plays mechanical properties. Review of these results leads to the idea that the Tuscaloosa Marine shale, being the weaker of the two specimens, may allow for more time and cost efficient extractions of the shale for use as a renewable energy source.

3.4 Nanoindentation versus Atomic Force Microscope Indentation Results

To begin, AFM indentations were only analyzed for the Woodford shale. As the AFM indentation tip has the same tip geometry as that of a Berkovich tip, the results were calculated under the assumption that all standard Berkovich tip-geometry functions were applicable to the AFM indenter tip. These functions, from Section 1.2.2.2, were then used so that the contact area, A_c, and the maximum displacement into the sample, h_c, can be calculated for the determination of the hardness and elastic modulus produced by AFM indentation. Figure 65 and Figure 66 show the force-displacement curves obtained through AFM indentation. The force and depth values at both the beginning and the end of the unloading phases are extracted which then allows for determination of the stiffness of the material, S. Once this is obtained, with contact area already determined, both the elastic modulus and the hardness can be determined through the equations presented within the Oliver and Pharr methodology. Because tests 5 and 6 were not completed under the same trigger threshold as tests 1-4, they have been excluded from calculations of mechanical properties.
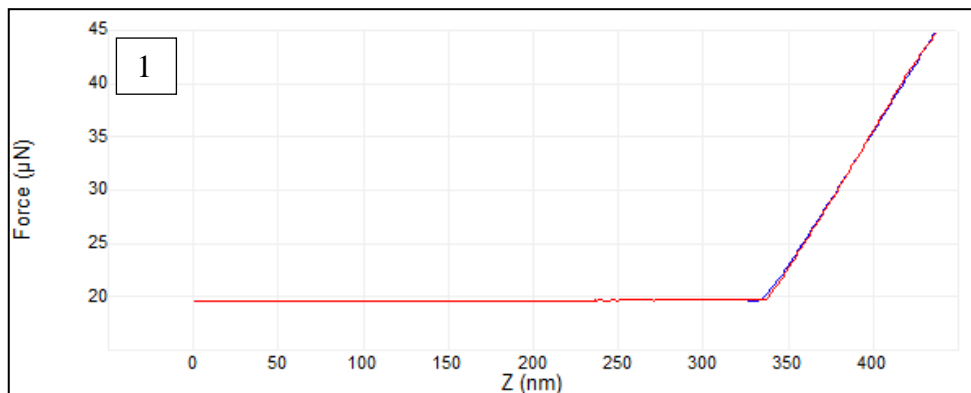
Figure 65: AFM indentation force-displacement curves (test 1 of 6).
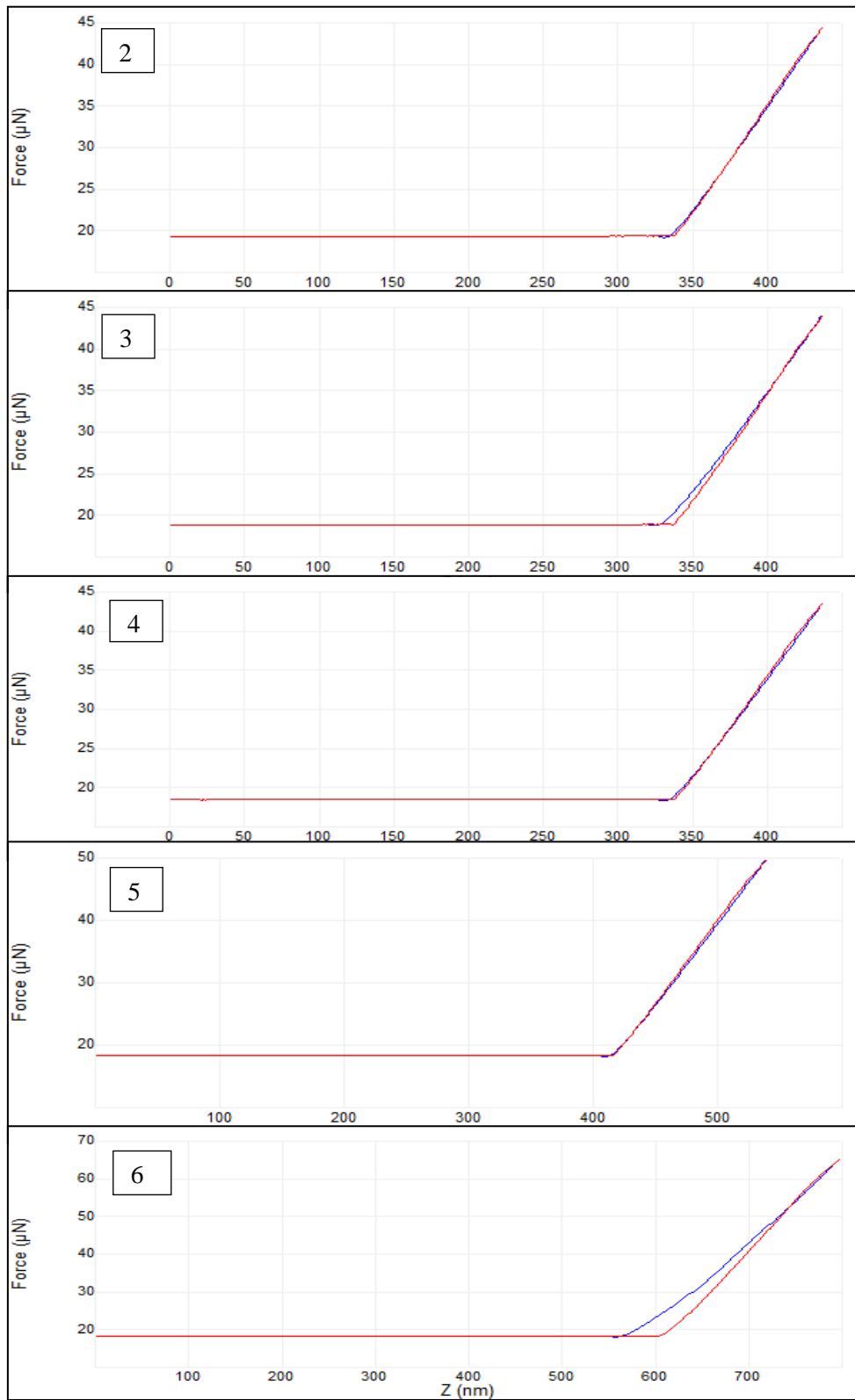
Figure 66: AFM indentation force-displacement curves (tests2-6).

This exclusion of results is done to prevent great standard deviations and misleading mean values as it is has already been discussed that the applied loading does have an effect on the results obtained. These two tests have only been included as to confirm this is also valid within AFM indentation results.

Table 14: Mean values and standard deviations for AFM indentation maximum indentation depth, hardness and elastic modulus for Woodford shale.

Location	Max Depth (µm)	Hardness (GPa)	Elastic Modulus (GPa)
Woodford	0.102±0.003	0.19±0.005	2.19±0.05

These results show very strong agreement with those found through nanoindentation, discussed previously. Although the max indentation depth is significantly lower through AFM analysis, it is to be expected as AFM only applies a fractional amount of the loading which nanoindentation does; therefore the depth in which the tip penetrates is not going to result as deep. For this reason, Figure 67 omits the comparison of maximum indentation depths and shows only the comparisons between elastic modulus and hardness values. From this it can be seen that both methods prove to provide reliable results; however it should be noted that an increased number of tests should be performed to ensure the accuracy of both indentation methods. Due to the various effects upon indentation results, a wide range of values may be missed through either method as AFM indentation will only provide a small amount of the total mechanical propterties. This is also true for nanoindentation as even though it provides a broader range of these properties, it still may not capture all of them. This is why a link is needed for the missing regions lying between the nano and micro scales.
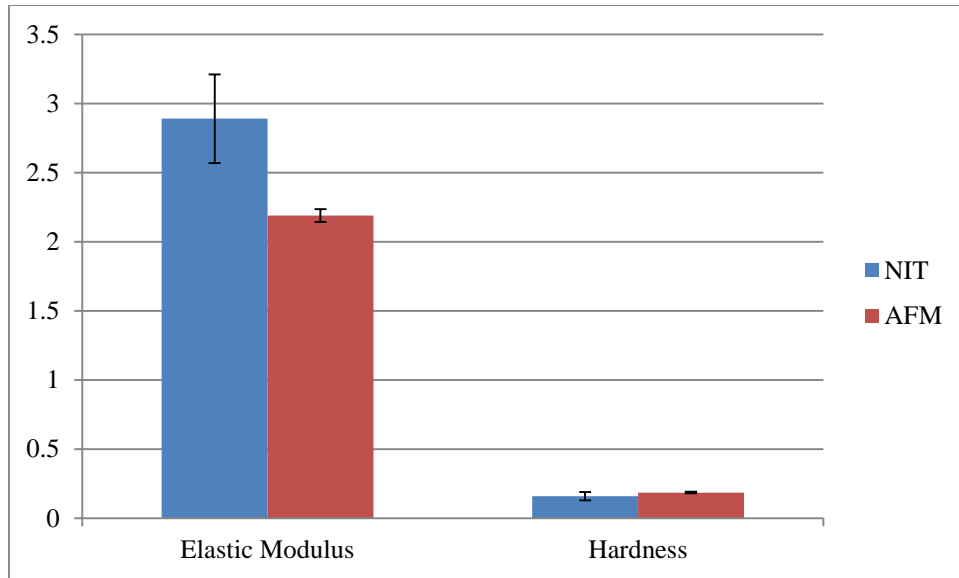
Figure 67: Nanoindentation versus AFM indentation values for Woodford shale. 1) elastic modulus, 2) hardness.

3.5 Size-Scale Effects

To answer the demand of needing a link between the nano and micro scales, peak force quantitative mechanical property mapping can be utilized. Results obtained through SPM (scanning probe microscopy) and both nano- and AFM indentation methods, can be highly effective in quantifying material mechanical properties. However, through these methods data is only provided at the exact point beneath the tips, providing singular data points across the surface one point at a time. Because shale is so highly heterogeneous, its' properties vary vastly across the surface and through most common methods of analysis, such as the few named previously, it is not always known how a component contributes to the adhesion, elastic modulus, hardness, and deformations experienced during testing. To solve this issue, QNM (quantitative material property mapping) has been developed. This method is applied experimentally similar to that of a tapping mode for AFM analysis. Figure 68 displays how this

method is applied as well as a typical illustration of the results acquired through PeakForce
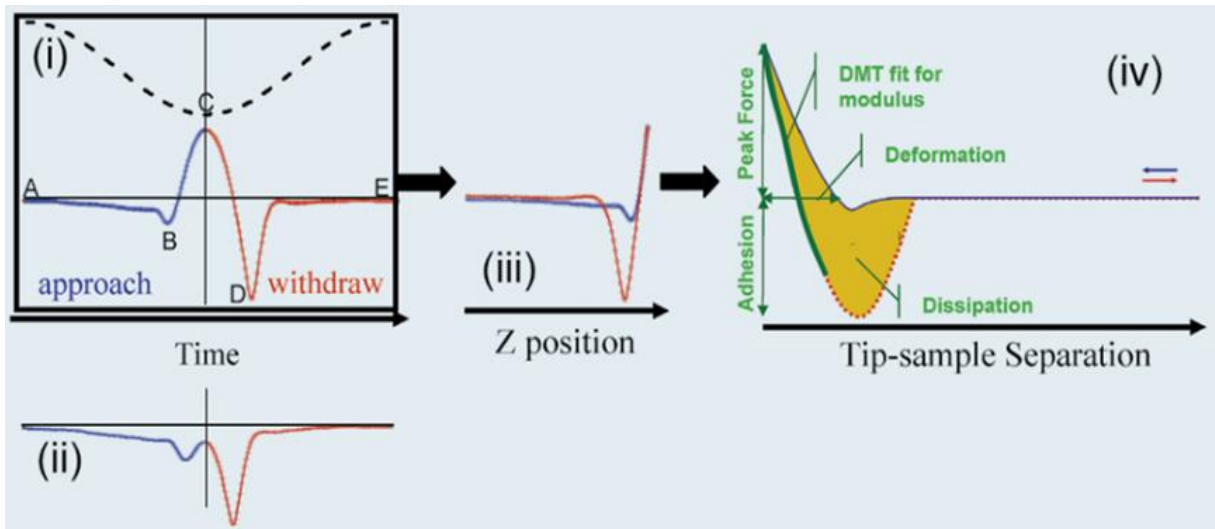
QNM methods.

Figure 68: Data aquisition for PeakForce QNM methods (Pittenger, Erina, & Su, 2012).

Preliminary investigation results of this method of analysis for Woodford shale samples

can be seen in Figure 69 and Figure 70.
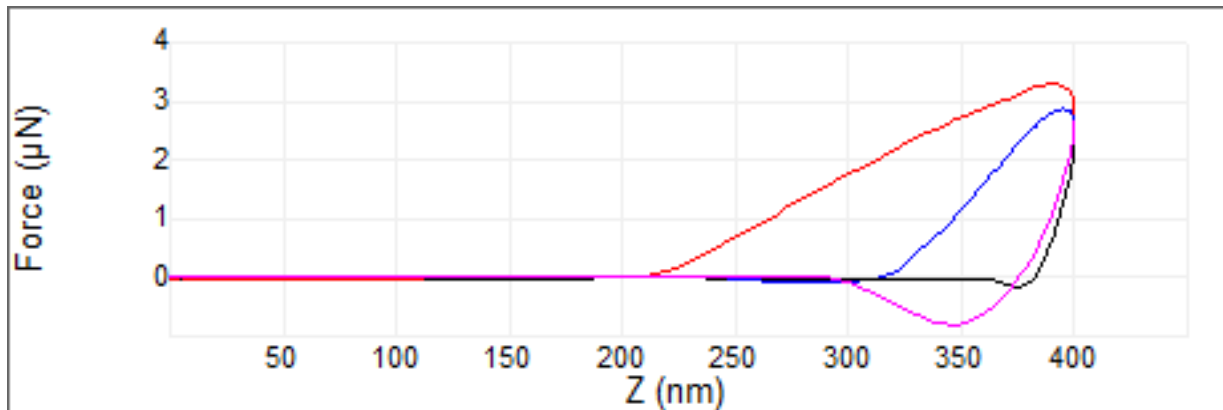
Figure 69: Cyclic force-displacement curves as obtained from PeakForce QNM analysis of

Woodford shale (courtesy Bruker Nano Inc.).
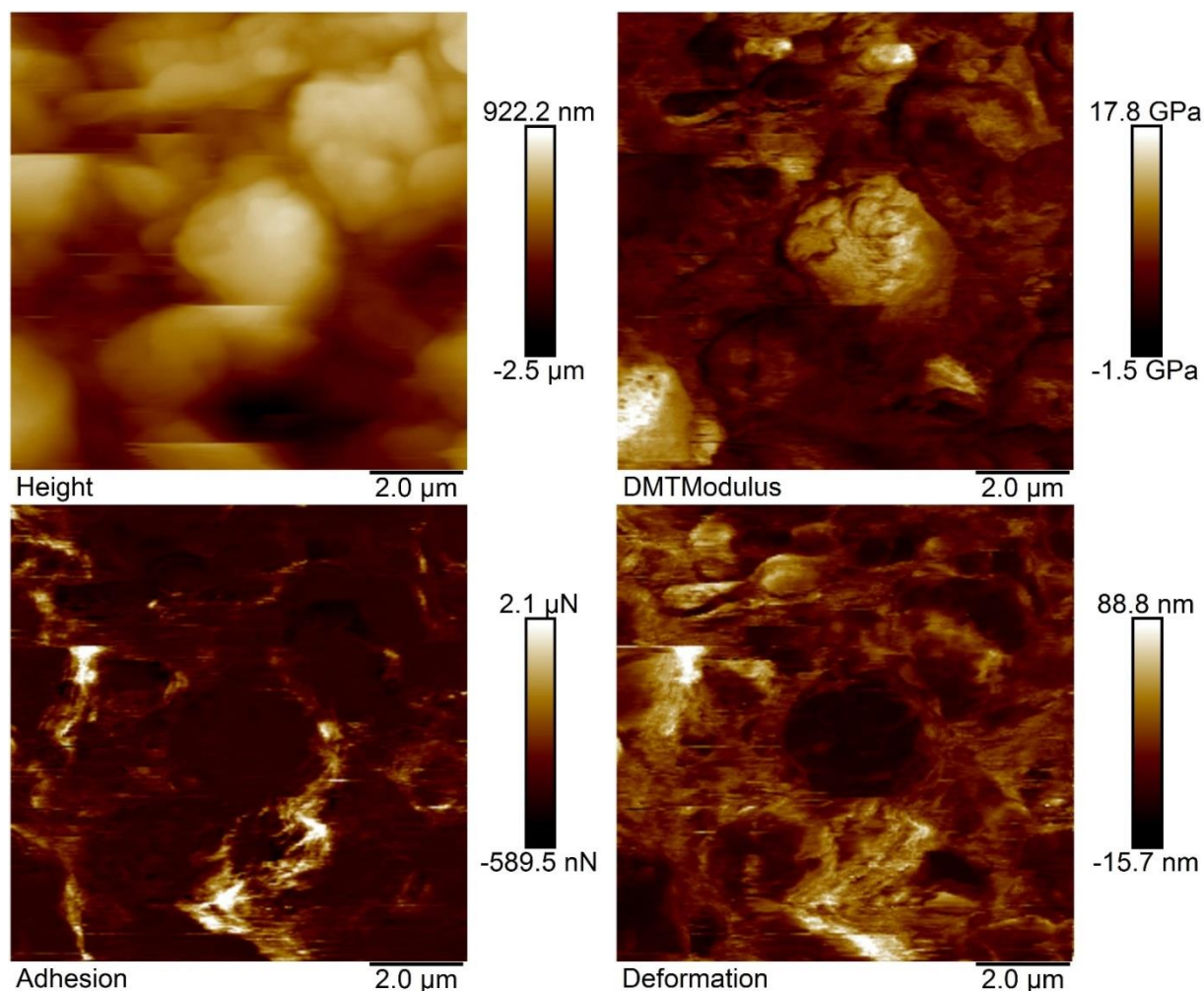
Figure 70: Typical PeakForce QNM analysis results (courtesy Bruker Nano Inc.).

Through this method of analysis, the topography, elastic modulus, adhesion, and deformations of a sample can all be analyzed in a non-destructive manner. Because of this method being non-destructive, nano and AFM testing can be completed afterwards to determine the relationships between each method. It should be noted, though, the results of this method are not to be used comparatively with those found through indentation as these tests were not conducted following proper procedures and calibrations. These results are solely to display the types of outputs obtainable for determining relationships through peak force QNM methods.

3.6 Determination of Total Organic Carbon

3.6.1 Thermogravimetric Analysis

      Initial Thermogravimetric Analysis (TGA) was conducted on a random sample of both Woodford and Tuscaloosa Marine shale. Figure 71 and Figure 72 shows the TGA result of the weight loss of Tuscaloosa Marine and Woodford shale oil respectfully, subjected to a heating rate of 10°C/min from room temperature to 700°C in a nitrogen atmosphere.
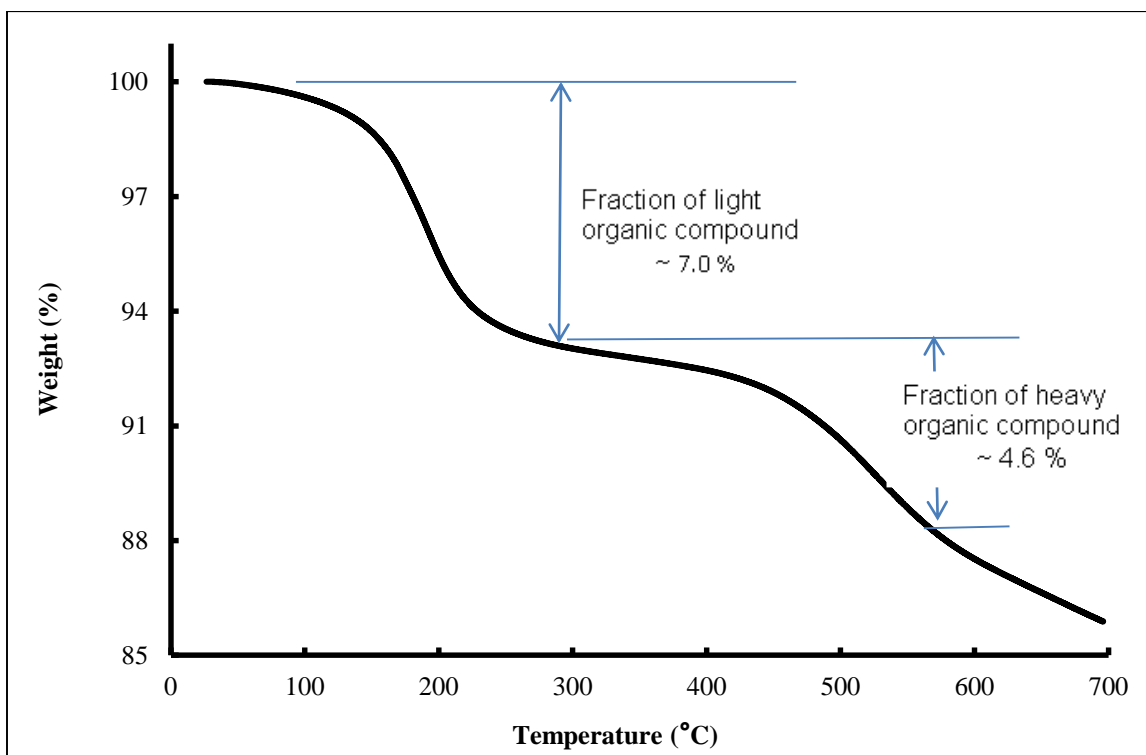
Figure 71: TGA result for Tuscaloosa Marine oil shale.
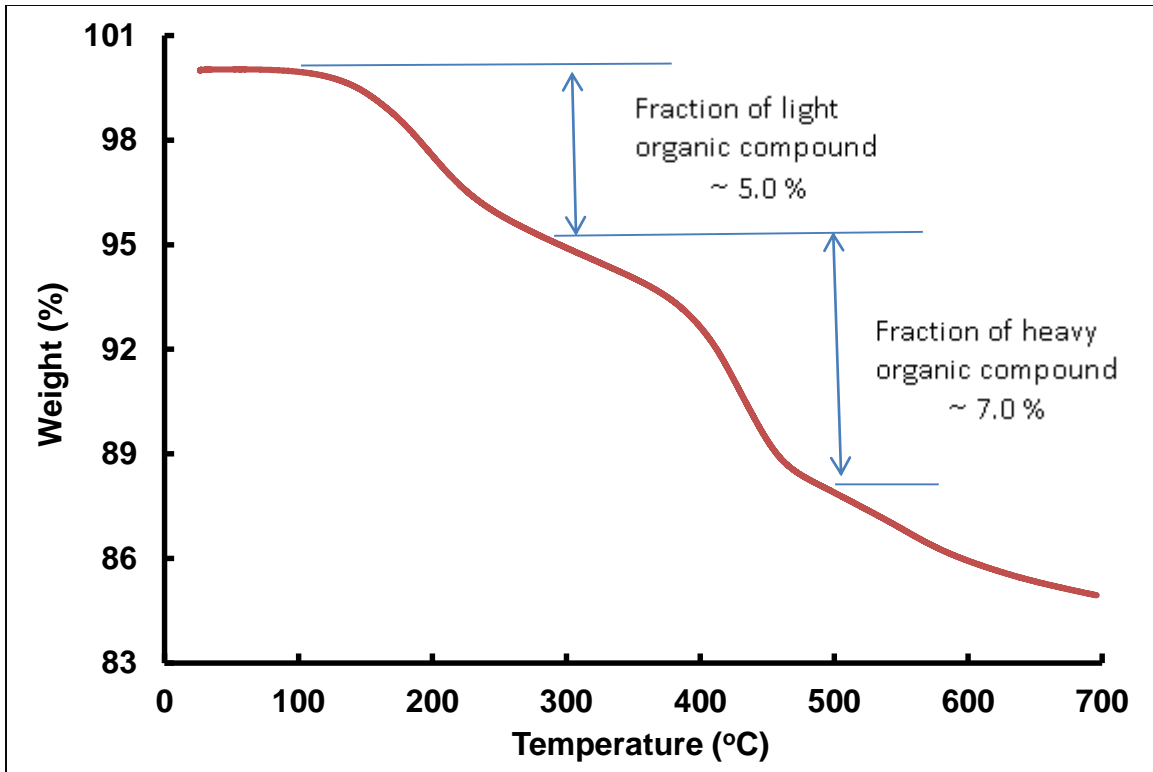
Figure 72: TGA result for Woodford oil shale.

These results show that the total organic contents are approximately twelve percent for both Tuscaloosa Marine and Woodford shale. Weight losses occurring at 200±50°C are attributed to the dematerialization of the light fraction contents as well as any remaining mineral oil trapped across the surface or in pores of the samples. It is believed that the second drop in weight occurring afterwards is due to the samples undergoing thermal cracking within the heavy fractions of the shale. Figure 73 shows a comparison of the results for the two shale samples.
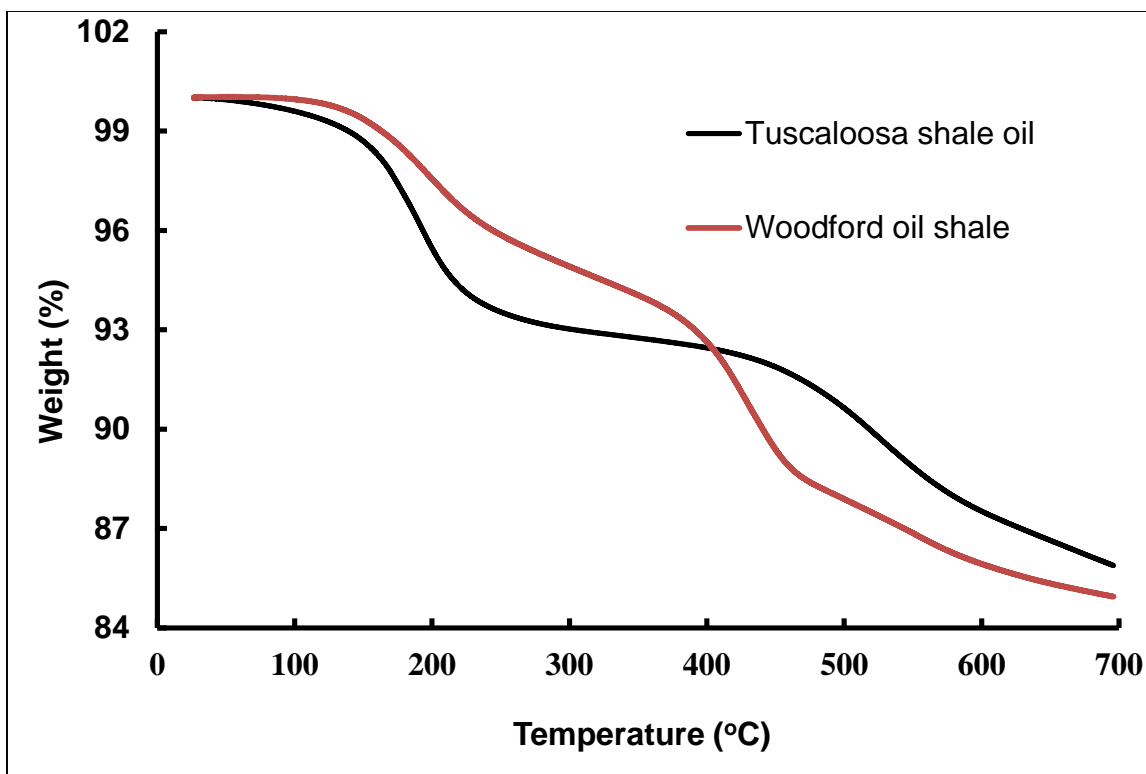
Figure 73: Comparison of TGA results for two shale samples.

The steeper curve for the Tuscaloosa Marine shale represents a narrower distribution within the materials compositions. This holds true for both the light and heavy fraction portions of the curve. It is quite clear that the light fractions begin decomposition at roughly the same temperatures. However, for the heavy fractions, the Woodford shale begins decomposing around 400±25°C, whereas the Tuscaloosa Marine shale begins around 500±50°C. This could mean the pyrolysis of the Tuscaloosa Marine may require approximately 100°C more than the Woodford shale in order to obtain oil and gas with small molecules from the heavy fractions of the shale. Also, this observation is based upon the assumption that the porosity of the two shale samples are either the same or similar to a degree in which the factors of porosity can be neglected.

Because the Tuscaloosa Marine shale showed more distinctive curve characteristics, further analysis was performed to investigate a cause of these distinguishing factors. To begin, a

sample of pure mineral oil of the type the shale is preserved in was tested to allow determination of its effect on the shale samples results. Figure 74 shows that 100% of the sample is removed around the same temperature as the light fractions of the previous shale tests.
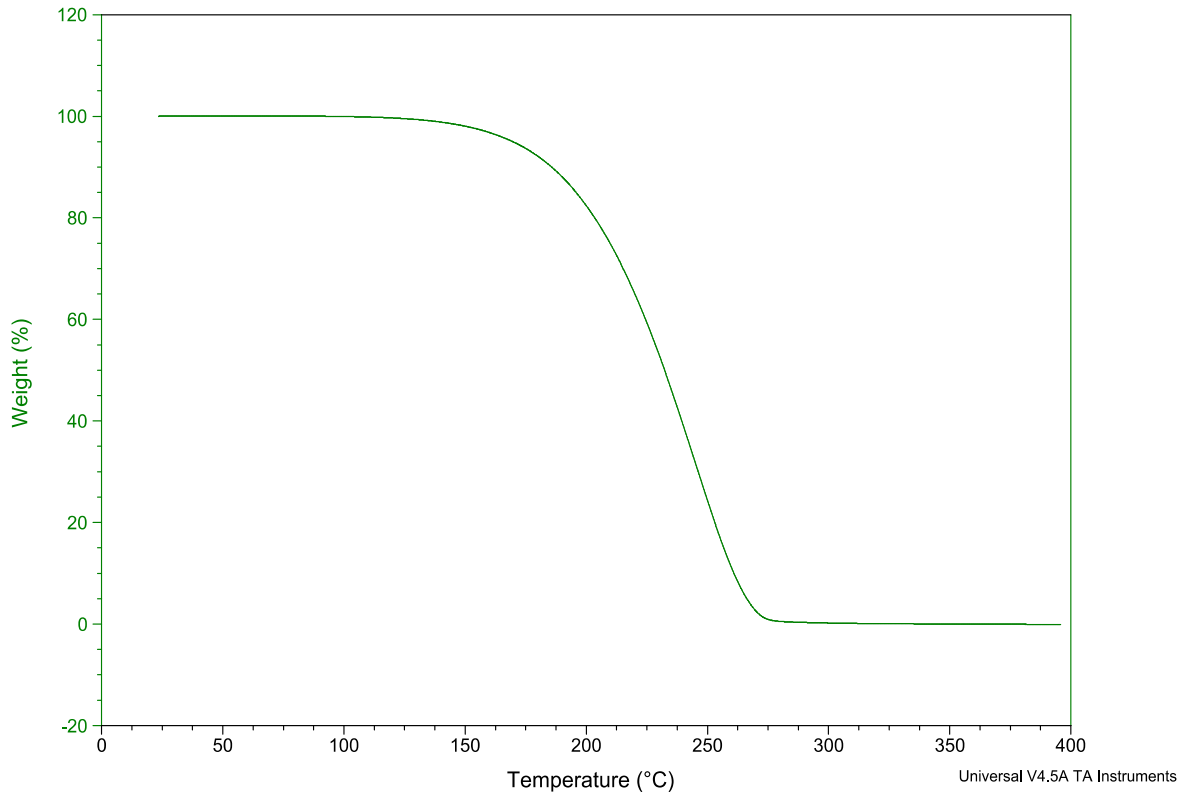
Figure 74: TGA analysis of mineral oil in which samples were stored.

Further comparisons of the effects of mineral oil were performed as Figure 75 shows the results of the mineral oil and Tuscaloosa Marine shale from a measured depth of 14300 ft.
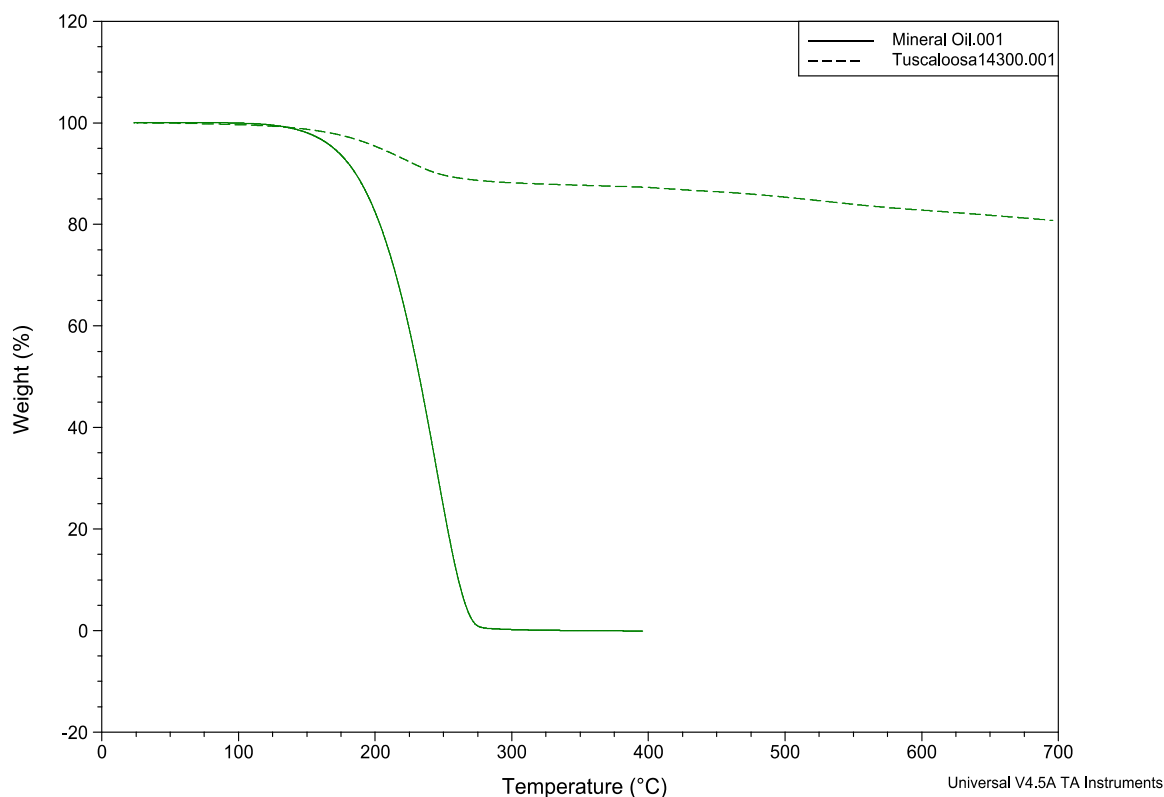
Figure 75: Comparative TGA analysis of mineral oil and Tuscaloosa Marine Shale from 14300 ft drilling length.

Additionally, tests were conducted to determine whether mineral oil affected the results of the heavy fractions. To do this, a sample was tested at a temperature ramp of 10°C/min from room temperature to 700°C. Then, the residual sample was submerged in pure mineral oil and allowed to soak for 48 hours. The sample (AT2D) was then retested under the same conditions as the initial test. Once completed, the sample was again submerged into pure mineral oil and allowed to soak for one week (~168 hours). Sample AT7D was then tested, also under the same conditions, and a comparison plot of the three tests was created as Figure 76 shows.
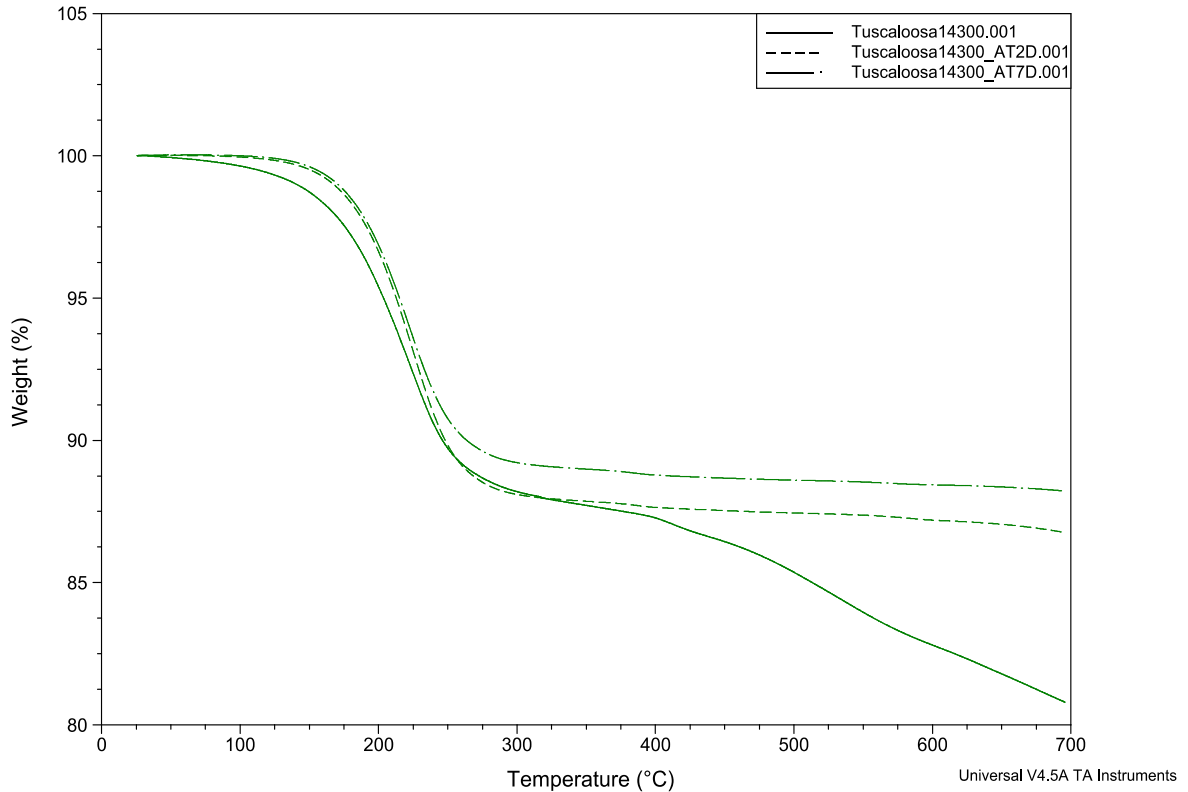
Figure 76: Comparative TGA analysis of Tuscaloosa Marine Shale at 14300 ft drilling length for initial, AT2D and AT7D tests.

The results of this method of testing verifies that the mineral oil does not affect the results obtained from the heavy fraction portion of the curves as well as confirms the mineral oil disappears along with the light fractions. The slight variation of the percent weight of samples AT2D and AT7D are attributed to any loss of material during handling and transferring from soaking containers and sample pans used for testing. Lastly, a comparison of the time-soaked samples and the mineral oil was plotted to verify visually that the samples are completely rid of mineral oil (at least the effects of) once heavy fractions begin decomposition.
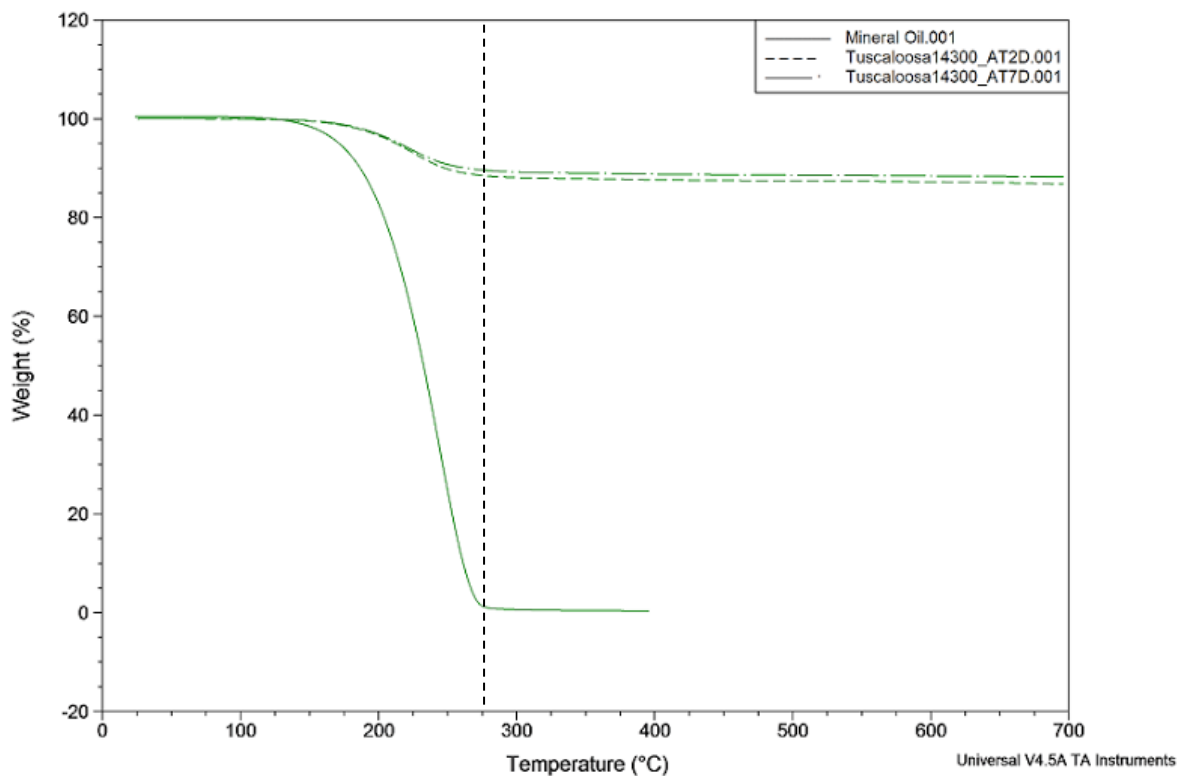
Figure 77: Comparative TGA analysis of TMS (14300ft) after burn two and seven day tests and

mineral oil.

Moving forward, the effects of temperature ramp rates were investigated. Using the initial

testing parameters of a 10°C/min temperature ramp from room temperature to 700°C as a basis

for comparison, similar testing was performed with the change to a temperature ramp of

2°C/min. The result of this analysis is seen in Figure 78. For purposes of this analysis, the

difference found between the two analyses is negligible as the resulting percent weight drops are

roughly within one percent of each other. With this in mind, the total testing time of the 2°C/min

analysis (including cool-down time ~45min) is ~6.6 hours whereas the 10°C/min only requires

~1.9 hours. Because the resulting values are within roughly one percent of each other, the

10°C/min temperature ramp testing will be performed for the remainder of the analysis to

conserve both time and resources. It should be noted, however, that for more specific

applications requiring precise temperature fluctuations, additional analyses should be performed

as a means of determining an optimized testing parameter.
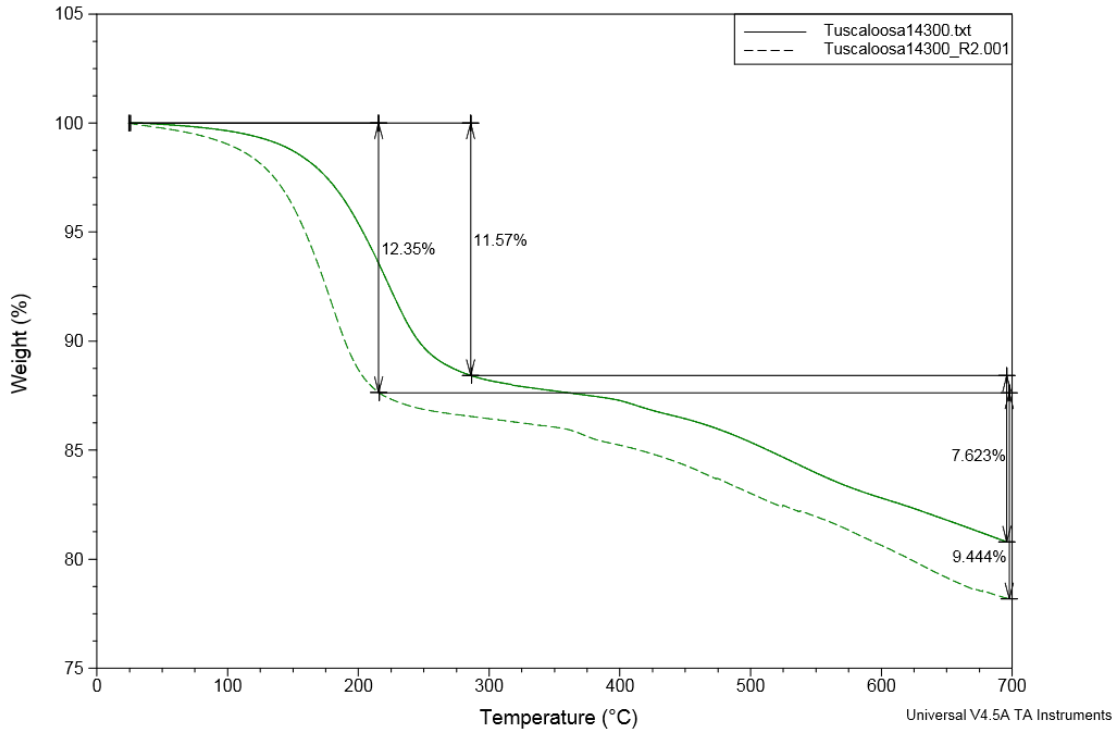
Figure 78: Comparative TGA analysis of Tuscaloosa Marine Shale from drilling length 14300 ft

under different temperature ramp rates.

Continuing, TGA tests were performed for each measured depth (14300-21300 ft in 500

ft increments) with the exception of measured depths 20300 and 20800 as additional samples

were not obtainable for this analysis. Figure 79 displays the results of these analyses.
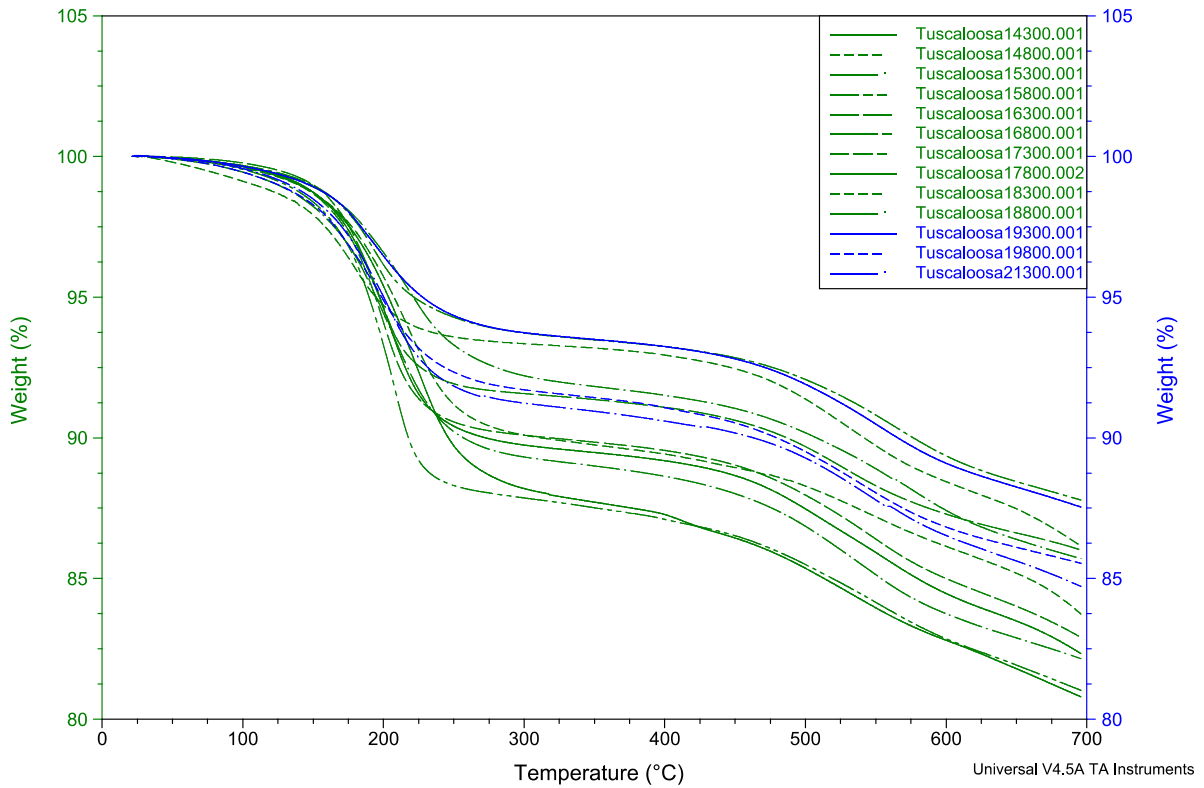
Figure 79: Comparative TGA analysis for all Tuscaloosa Marine Shale specimens from depths ranging 14300 to 21300 feet in 500 foot increments (with exception of 20300 and 20800 depths).

It is very clear that all measured depths display similar characteristics in the dematerialization of both light and heavy fractions. To better understand the results, Table 15 is composed of the mean and standard deviations for both the light and heavy fractions found within the samples. Individual plots of the decompositions respective to each sample can be found in Appendix C.

Table 15: Mean and standard deviation values of light and heavy gas fractions of Tuscaloosa Marine Shale.

	μ	σ
Light Gas/ Mineral Oil	8.77	1.93
Heavy Gas	6.89	0.63

In short, through TGA analysis, the TOC for Tuscaloosa Marine shale can be evaluated by quantifying both the light and heavy fractions found within each sample. Although porosity is not tested as a influencing factor among these results, it should be kept in mind that shale, being a highly anisotropic and heterogeneous material, can vary greatly in both porosity and composition. As mentioned previously, this analysis has been conducted under the assumption that the variation in porosity is negligible, that the resulting values are representative of the shale material wholly and not at individual measured depths. Another result of this form of analysis is that the thermal stabilities (such as the temperature which pyrolysis can be expected) and distribution of compositions can be quantified.

3.6.2 X-ray Diffraction Analysis

The final phase in characterizing the shale plays properties is to analyze their mineralogy in order to determine what each consists primarily of. With the results of this analysis, the total organic carbon can be related to that found through thermogravimetric testing, as well as creating a possibility to determine the effect of mineralogy on obtained nanoindentation results. As mentioned previously, X-ray diffraction analysis of Woodford shale was performed by K-T GeoServices Inc. and Weatherford Laboratories. After testing, Weatherford Laboratories determined the composition of the shale is primarily quartz, with close fractions of illite/mica and other minerals, followed by few additional types of clay. The weight percentages of each component can be seen in Figure 80. Additionally, it was determined that the Woodford shale has an average total organic carbon content of approximately 11.26% which is in very good agreement with the total organic carbon contents found through previous TGA testing.
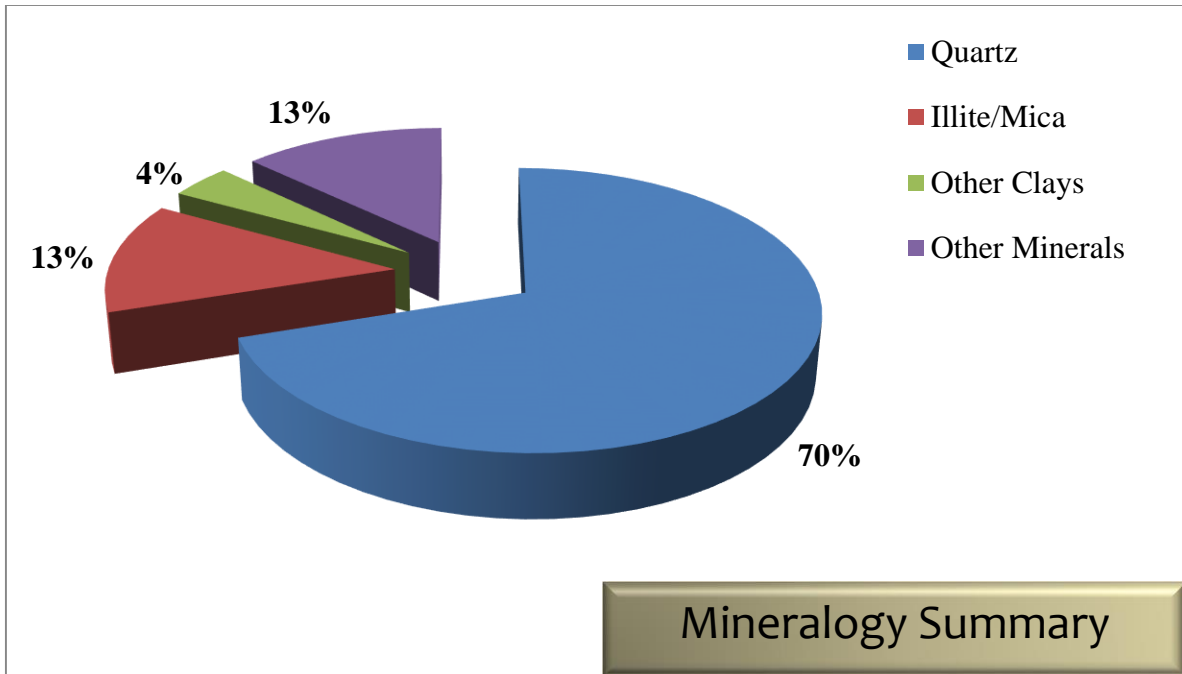
Figure 80: Summary of Woodford shale mineralogy from Weatherford Laboratories (%weight).

Because these percentages leave room for many questions about what the "other minerals" portion is composed and the same with the "other clays", K-T GeoServices Inc. further broke down the components so that both the mineralogy and phyllosilicate compositions could be analyzed. Figure 81 and 82 show the X-ray diffraction trace data acquired from testing.
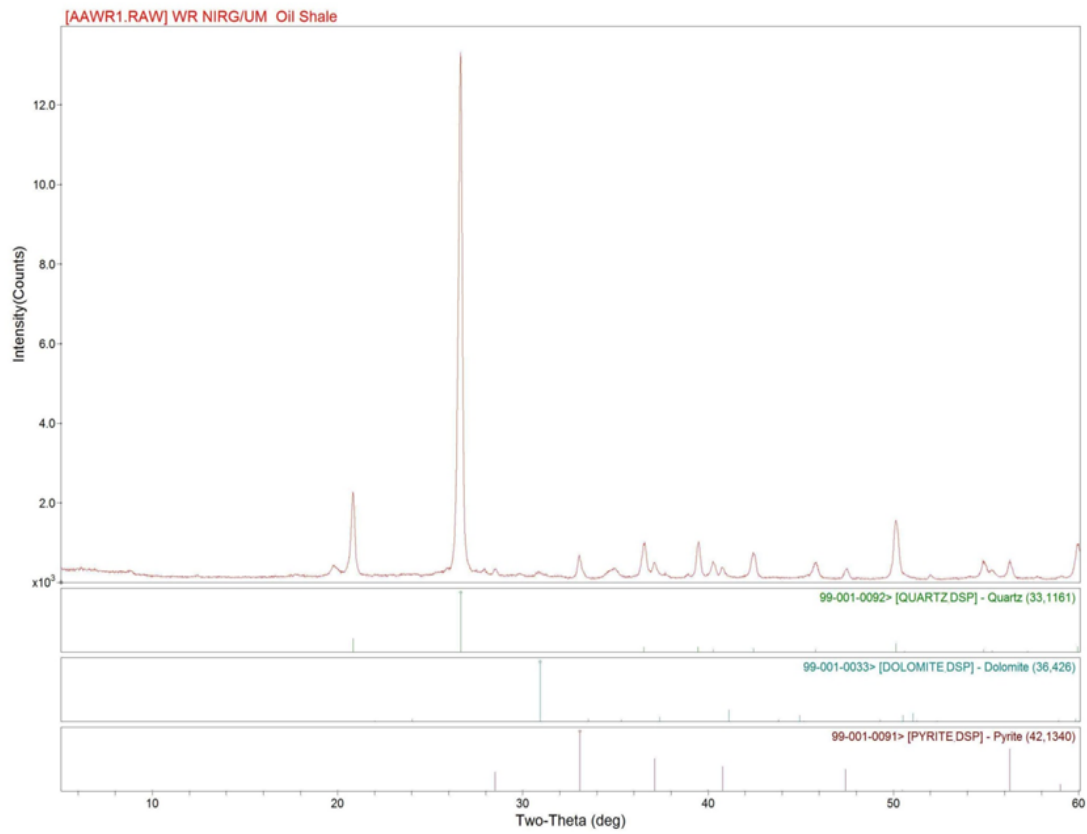
Figure 81: Bulk (Whole Rock) X-ray diffraction trace (courtesy K-T GeoServices Inc.)
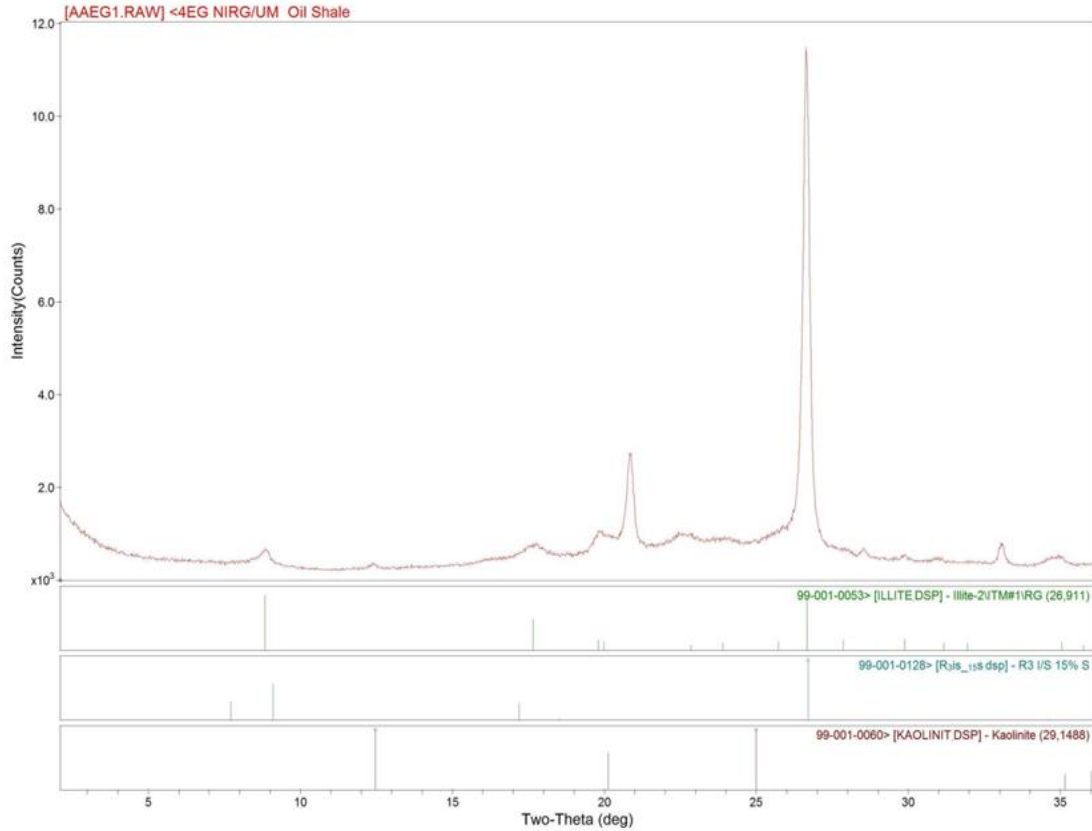
Figure 82: 4 micron ethylene glycol solvated X-ray diffraction trace (courtesy K-T GeoServices Inc.)

From the given trace data, components can be derived according to the location and magnitudes of the peaks within the data set. Once each peak has been classified, the components can then be quantified as percent weights and fractioned as Figure 83 through Figure 85 show.
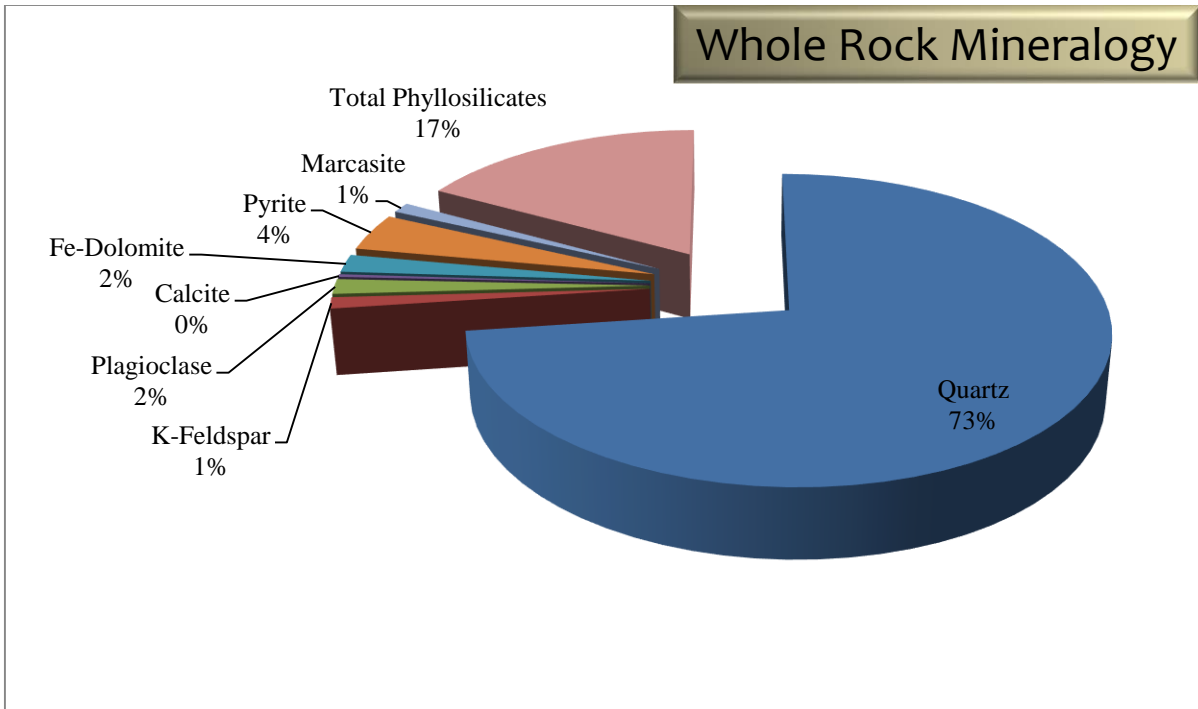
Figure 83: Whole rock mineralogy of Woodford shale from K-T GeoServices (%weight).
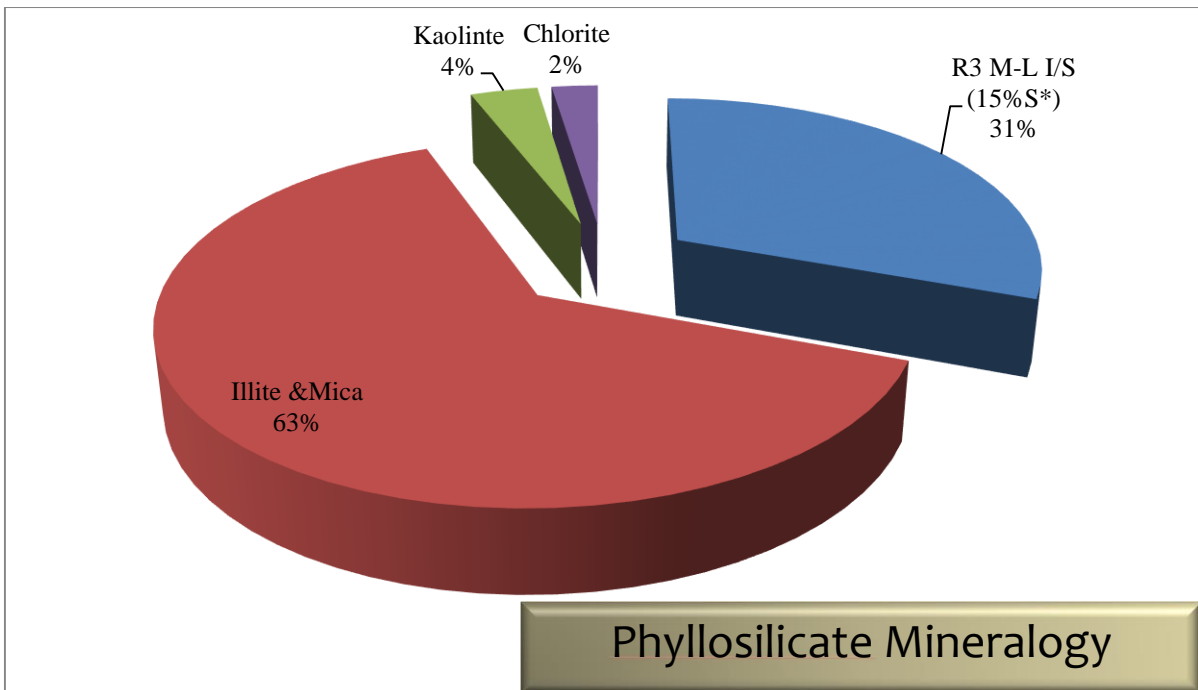
Figure 84: Phyllosilicate mineralogy of Woodford Shale from K-T GeoServices (Relative

Abundance).
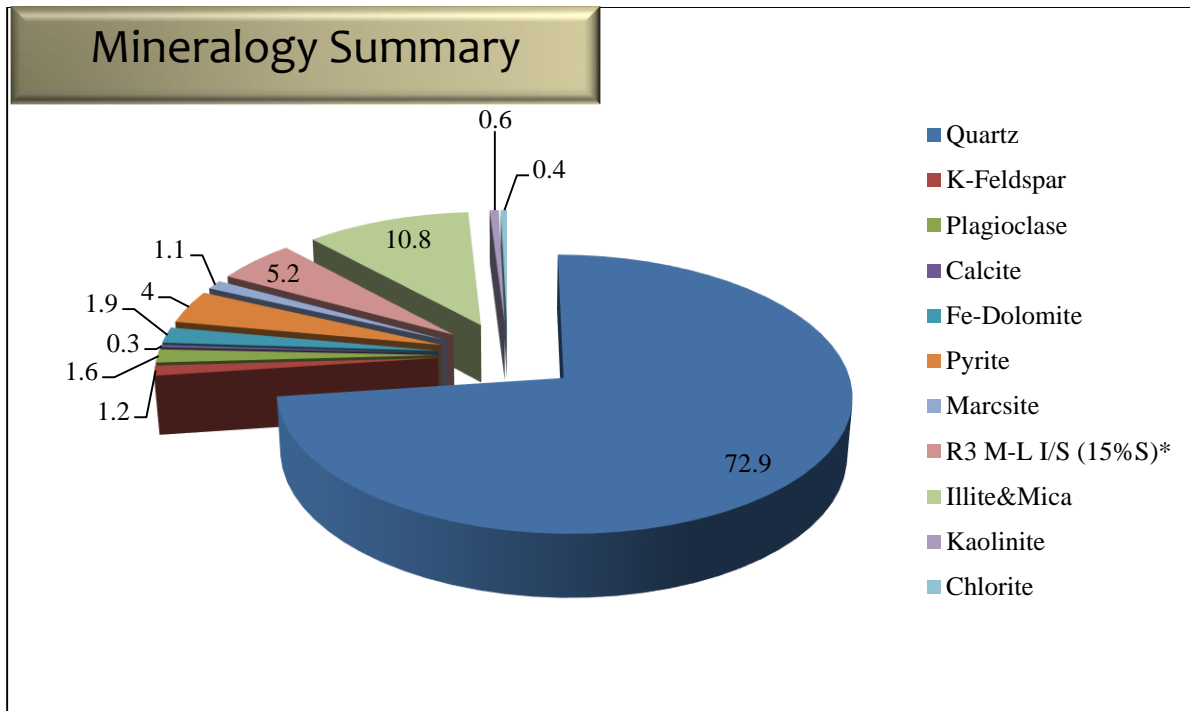
Figure 85: Summary of Woodford shale mineralogy from K-T GeoServices (%weight).

Through this it can be seen that both services are in good agreement with one another. The slight differences within the weight percentages are attributed to the level of analyses performed as well as the slight difference in sample preparation and testing methods. Lastly, both analyses are in good agreement with the results from TGA testing completed which concludes average TOC for Woodford shale is approximately 12%. Due to the extensive duration of X-ray diffraction testing and the good agreement between the results acquired through XRD and TGA tests, the Tuscaloosa Marine shale has not been tested by XRD.

CHAPTER 4: CONCLUSIONS

1. Both AFM and nano-indentation were applied successfully to obtain mechanical properties of drill-cuttings from Tuscaloosa Marine Shale.

2. Bedding orientations had a significant effect on nanoindentation results. The elastic modulus and hardness of Woodford shale tested parallel to the geological layering ranged approximately from 2.5 to 23 GPa, having an average value of 11.6±5.5 GPa, and 0.1 to 2.5 GPa with average value of 0.71±0.72 GPa respectively. Similarly, the elastic modulus and hardness of the same shale tested perpendicular to the layering ranged from approximately 2 to 16.5 GPa, with average value of 6.1±3 GPa, and 0.001 to 1.15 GPa with average value of 0.27±0.23 GPa, respectively.

3. Through multi-directional testing comparison and of nanoindentation on core plugs from Woodford shale and epoxy embedded chips of Tuscaloosa shale material, it has been concluded that nanoindentation testing methods can be used to successfully quantify the mechanical properties of shale materials through testing of chips or drill cuttings regardless of bedding orientations when the cuttings are properly mounted and polished. This reduces both the amount needed and costs associated with acquiring samples for testing purposes.

4. It was observed that increased polishing levels induce greater damage to test specimens.

5. Increased levels of TOC caused samples to have lower, average mechanical properties..

6. As TOC percentages only showed slight deviations between measured depths, a sound indicator of TOC percentage based on mechanical properties was not determined. However, organic contents within shale materials have lower elastic modulus and hardness values than that of materials such as quartz, calcite, and some clay materials. From this it will be seen that the mechanical properties obtained through nanoindentation will experience a negatively inverse relationship with TOC percentages (i.e. one increases as the other decreases).

7. Due to the natural heterogeneity of shale materials, the size-scale effects have great impact on the results obtained through indentation analyses. For standard indentation procedure, the results will ultimately be on a global scale. For nanoindentation, the results are still considered to be on a global scale, however the properties are determined to be semi-local. In the case of AFM indentation, the resulting properties are completely local. Through the use of peak force analysis, the link between AFM's local and nanoindentation's semi-local results can be made.

8. Lastly, the success of nanoindentation for calculating the average mechanical properties of oil shales makes this methodology highly attractive. The Tuscaloosa Marine shale shows great promise that while containing approximately the same TOC levels as the Woodford play, since the Tuscaloosa Marine shale is a weaker material, less resources will be required to extract the proportionally same amount of shale materials for use as a renewable energy source.

CHAPTER 5: RECOMMENDATIONS AND FUTURE WORK

1. Artificial Neural Networks has been used for determining and validating properties obtained through experimental procedures (results are not included in this thesis).

2. Further research is needed to calibrate AFM to obtain quantitative mechanical properties using peak-force analysis and to define the link between AFM and Nano-indentation results.

3. Future testing of oil shale through AFM indentation, for comparison purposes, should remain at maximum applied loads which correspond directly to nanoindentation loads as to alleviate any deviations within results due to the effects of applied loadings.

4. Retrieval of the vertical and horizontal coordinates associated with the previously received measured depth for determining trends in the shales with respect to in-situ locations.

5. A core sample of Tuscaloosa Marine shale should be obtained and analyzed as this document discusses for the completion of comparisons between drill cuttings and core plug samples.

6. Correlate the mechanical properties presented within this document to initial and cumulative production rates through the use of well log data from at least two, local wells within the TMS trend. This will allow for correlation to oil and gas extraction data.

7. Multiscale modeling (i.e. molecular dynamics, discrete element, etc.) to evaluate the effect of oil shale nano- and micro-properties on elastic transport and fracture properties

LIST OF REFERENCES

Aoudia, K., Miskimins, J., Harris, N., & Mnich, C. (2010, January 1). Statistical Analysis of the Effects of Mineralogy On Rock Mechanical Properties of the Woodford Shale And the Associated Impacts For Hydraulic Fracture Treatment Design. *American Rock Mechanics Association*.

Bennett, K., Berla, L., Nix, W., & Borja, R. (2015). Instrumented Nanoindentation and 3D Mechanistic Modeling of A Shale At Multiple Scales. *Acta Geotechnica Acta Geotech, 10*(1), 1-14.

CSM Instruments. (2007, March 23). The Influence of Surface Roughness on Instrumented Indentation Testing (IIT).

Doerner, M., & Nix, W. (1986). A Method for Interpreting the Data From Depth-Sensing Indentation Instruments. *Journal of Materials Research, 1*(4), 601-609.

Dow, W. (2011, September 27). How Plant and Animal Remains Become Oil and Gas: A Geochemical Perspective*. *Search and Discovery*(40830).

Fischer-Cripps, A. (2004). *Nanoindentation* (3rd ed.). New York: Springer.

Hay, J. (2009). Introduction To Instrumented Indentation Testing. *Experimental Techniques, 33*(6), 66-72.

Hay, J. (2013). The Revolutionary Impact of The Oliver and Pharr Technique On The Science of Hardeness Testing. *Agilent Technologies*.

Hay, J., & Sondergeld, C. (2010). Mechanical Testing of Shale by instrumented Indentation. *Agilent Technologies*.

Jauberteau, I., Nadal, M., & Jaubertau, J. (2008). Atomic Foce Microscopy Investigations on Nanoindentation Impressions of Some Metals: Effect of Piling-Up on Hardness Measurements. *Journal of Materials Science, 43*(17), 5956-5961.

John, C., Jones, B., Moncrief, J., Bourgeoiss, R., & Harder, B. (n.d.). *An Unproven Unconventional Seven Billion Barrel Oil Resource - the Tuscaloosa Marine Shale*. . BRI Bulletin.

Kadine Mohomed, P. (n.d.). *Thermogravimetric Analysis Theory, Operation, Calibration and Data Interpretation*. TA Instruments.

Kumar, V., Sondergeld, C., & Rai, C. (2015). Effect of Mineralogy and Organic Matter On Mechanical Properties of Shale. *Interpretation, 3*(3), SV9-SV13.

Louisiana Department of Natural Resources. (2016, March 16). Retrieved from Louisiana Department of Natural Resources: http://dnr.louisiana.gov/index.cfm?md=pagebuilder

Mavko, G. (2013). Rock Physics of Shale. *Lecture Presented in Stanford Rock Physics Laboratory*Micro Star Technologies. (n.d.). Nanoindenters From Micro Star Technologies. *Micro Star Technologies, 2*(3). Retrieved from http://www.microstartech.com/index/NANOINDENTERS.pdf

Oil & Natural Gas Field. (2014). *Alabama Shale- Alabama Shale Map*. Retrieved March 17, 2016, from http://oilshalegas.com/alabamashale.html

Oliver, W., & Pharr, G. (2004). Measurement of Hardness and Elastic Modulus By Instrumented Indentation: Advances In Understanding and Refinements To Methodology. *Journal of Materials Research, 19*(1), 3-20.

Pittenger, B., Erina, N., & Su, C. (2012). *Quantitative Mechanical property Mapping at the Nanoscale with PeakForce QNM*. Santa Barbara, CA: Bruker Nano Surfaces Division.

Ramirez, J. (2010). *Nanoindentation Creep Measurement*. Nanovea.

Sayers, C. (2012). The Effect of Anisotropy On The Young's Moduli and Poisson's Ratios of Shales. *Geophysical Prospecting, 61*(2), 416-426.

Schuh, C. (2006). Nanoindentation Studies of Materials. *Materials Today, 9*(5), 32-40.

Talbot, J. (2012). *Sample Preparation and Analytical Procedures.* Gunnison, CO: K-T GeoServices Inc.

Tuscaloosa Marine Shale (TMS). (n.d.). Retrieved March 17, 2016, from http://www.tuscaloosa-marine-shale.com/

Weatherford Laboratories. (2012). *X-ray Diffraction (XRD) Analysis.* Houston, TX: Weatherford Laboratories.

Zeszotarski, J., Chromik, R., Vinci, R., Messmer, M., Michels, R., & Larsen, J. (2004). Imaging and Mechanical Property Measurements of Kerogen Via Nanoindentation. *Geochimica Et Cosmochimica Acta, 68*(20), 4113-4119.

LIST OF APPENDICES

A. Running Average of Elastic Modulus Values
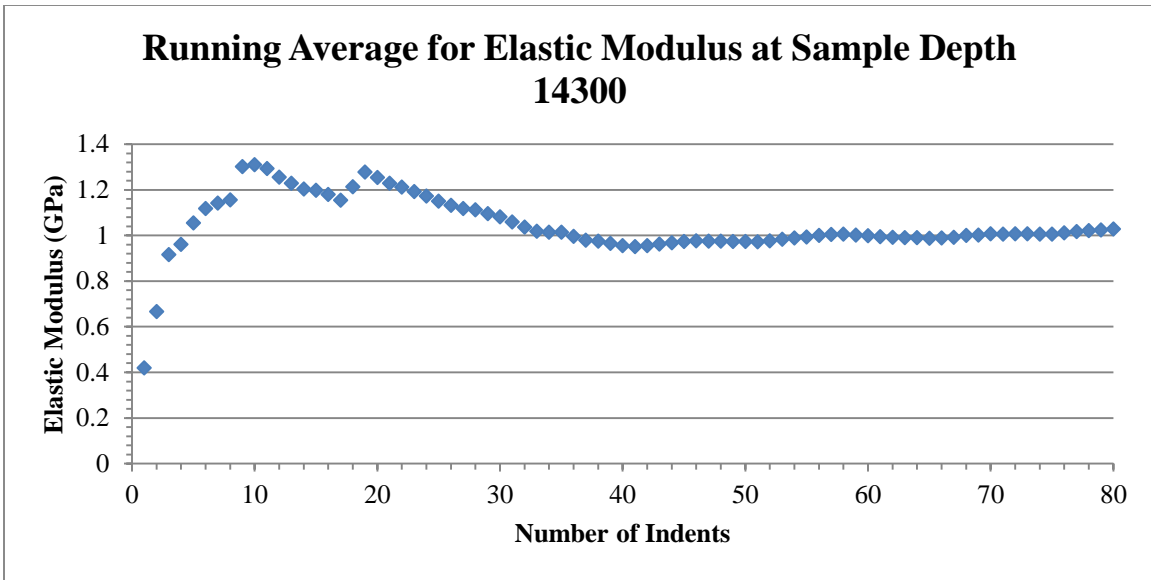
Figure A. 1: Running average for elastic moduli at measured depth 14300.
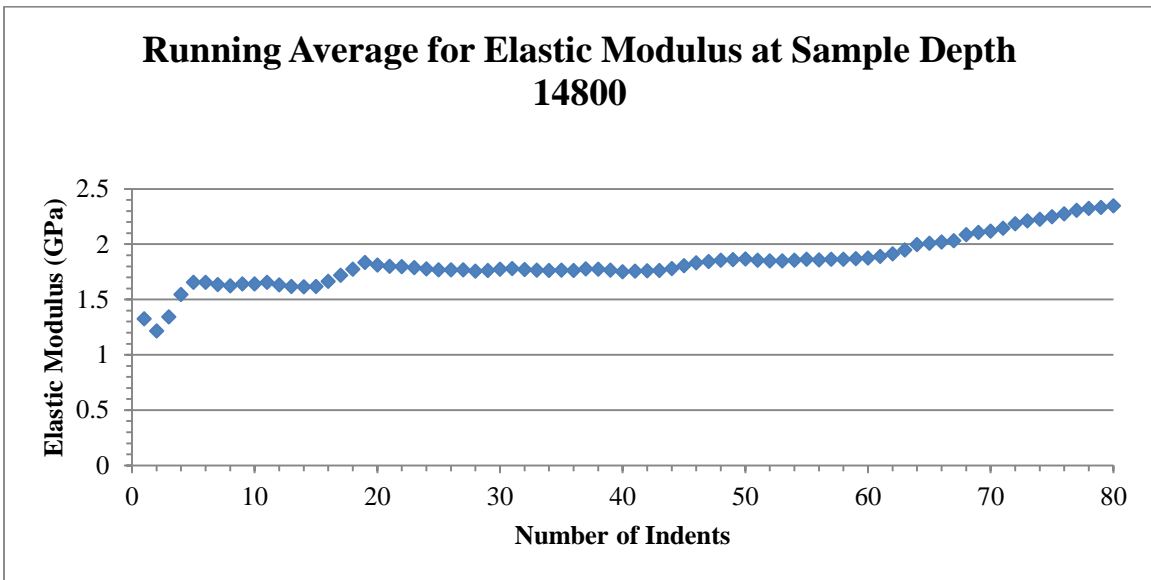
Figure A. 2: Running average for elastic moduli at measured depth 14800.
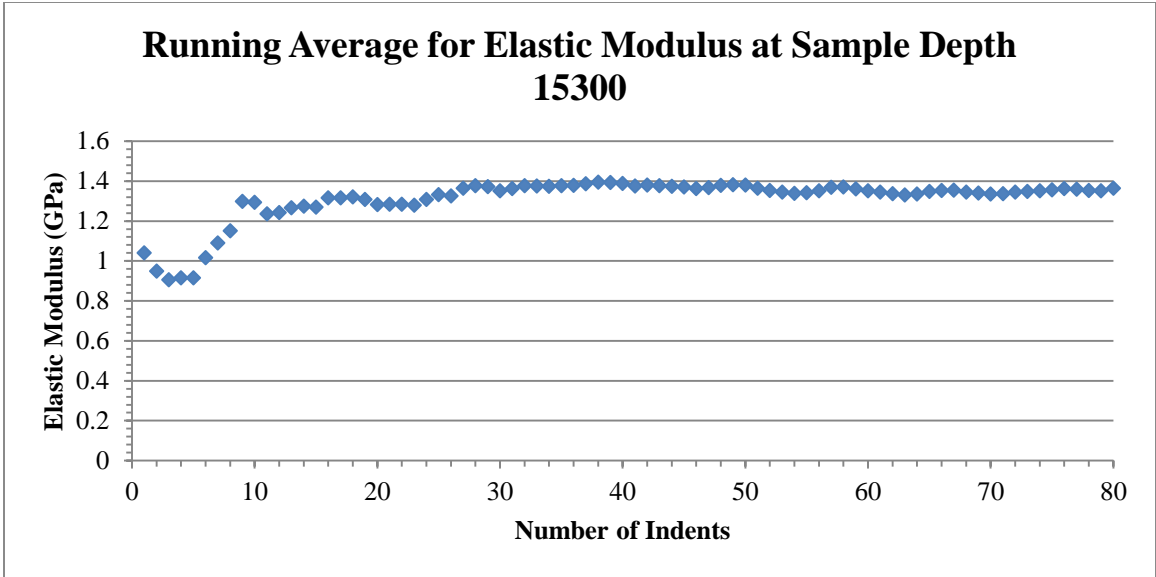
Figure A. 3: Running average for elastic moduli at measured depth 15300.
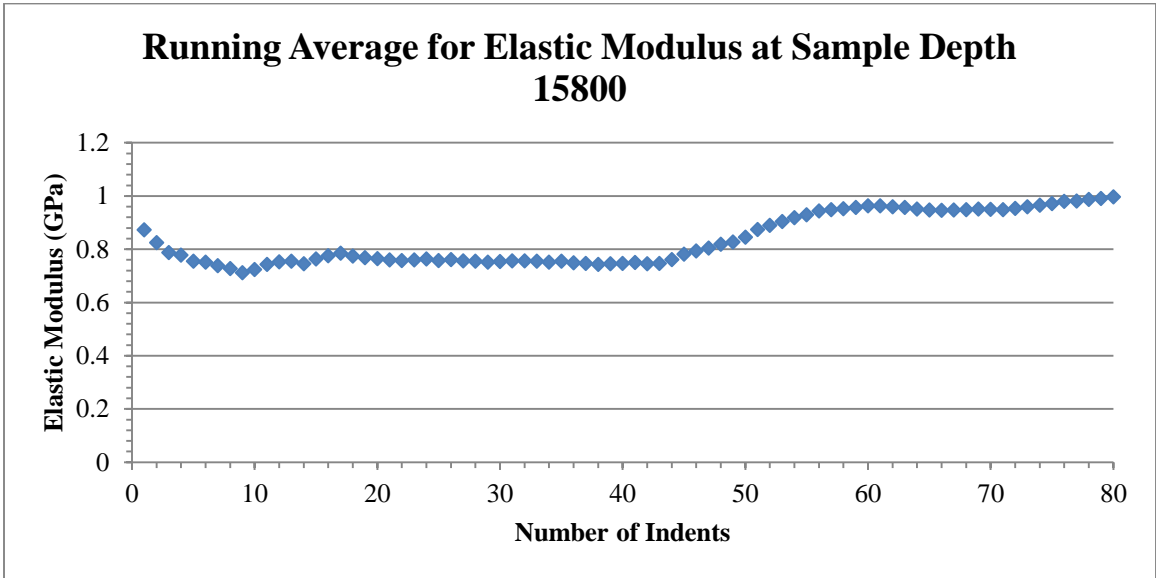
Figure A. 4: Running average for elastic moduli at measured depth 15800.
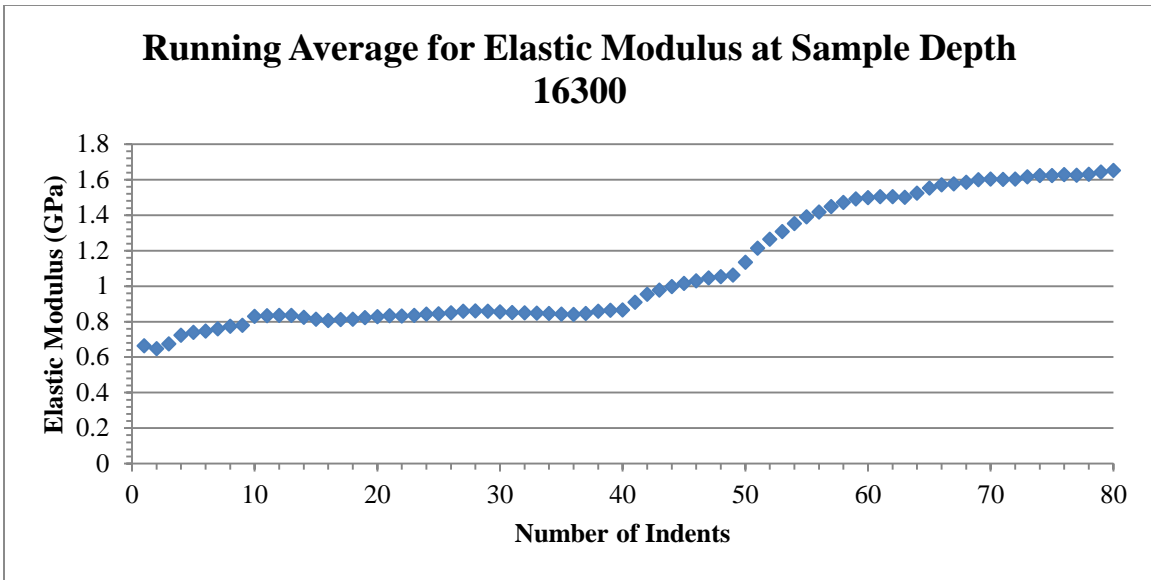
Figure A. 5: Running average for elastic moduli at measured depth 16300.
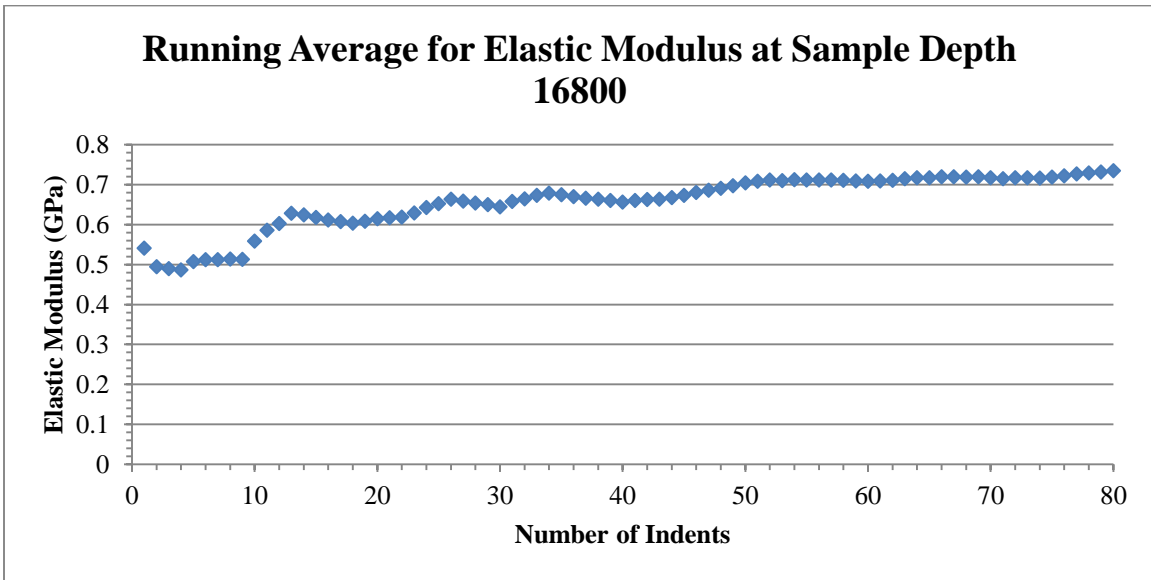
Figure A. 6: Running average for elastic moduli at measured depth 16800.
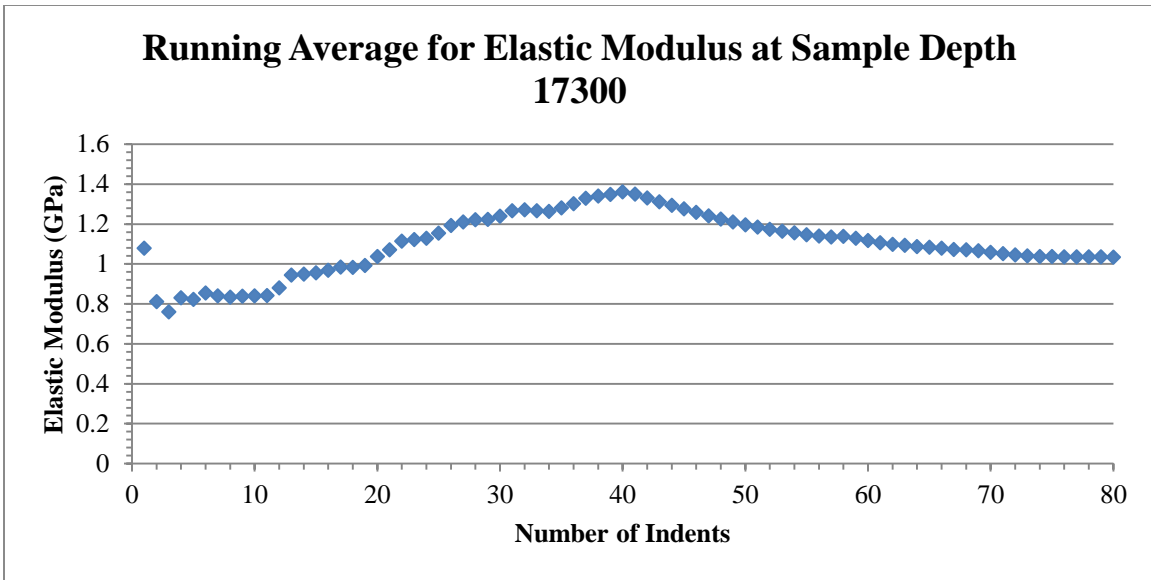
Figure A. 7: Running average for elastic moduli at measured depth 17300.
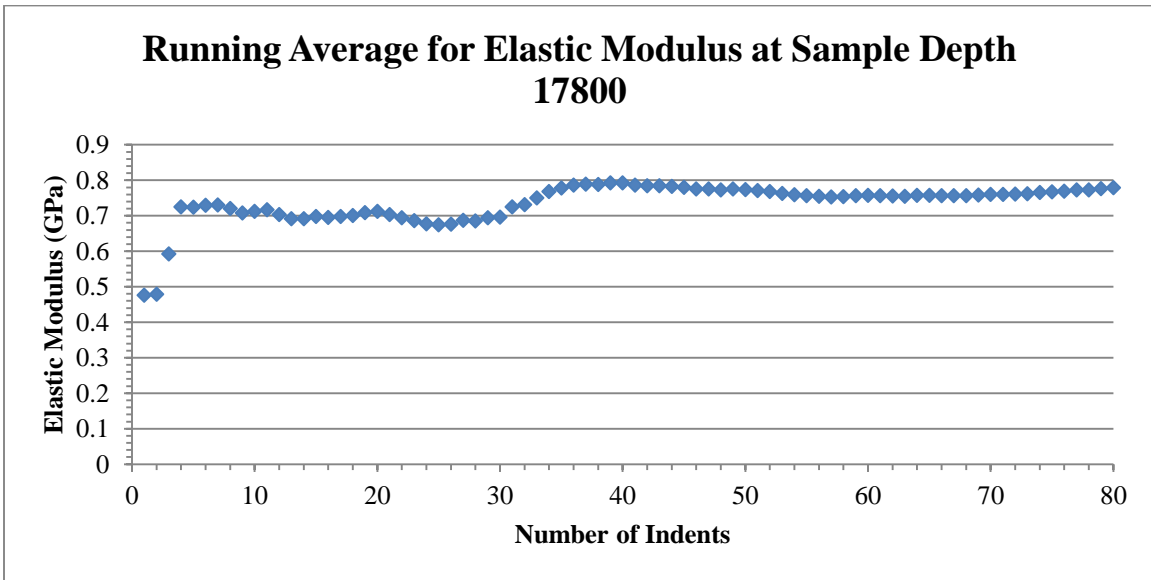
Figure A. 8: Running average for elastic moduli at measured depth 17800.
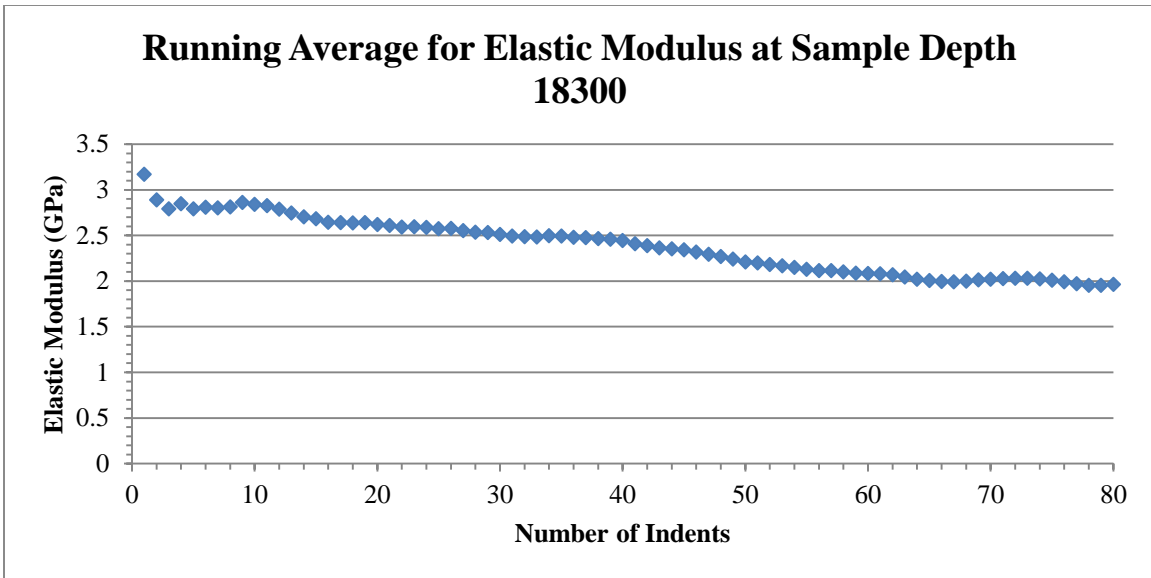
Figure A. 9: Running average for elastic moduli at measured depth 18300.
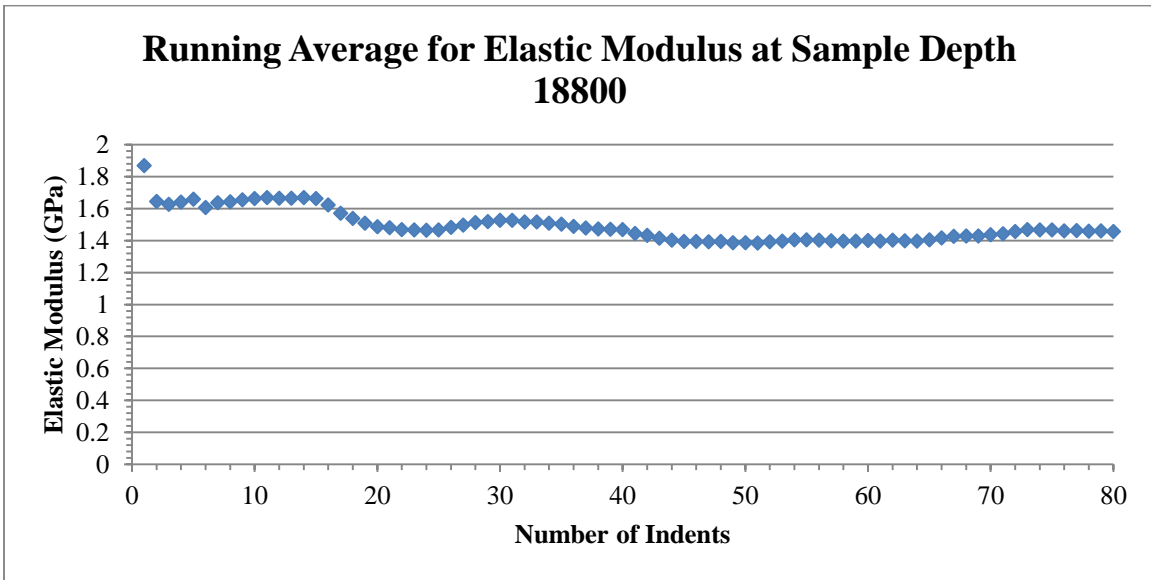
Figure A. 10: Running average for elastic moduli at measured depth 18800.
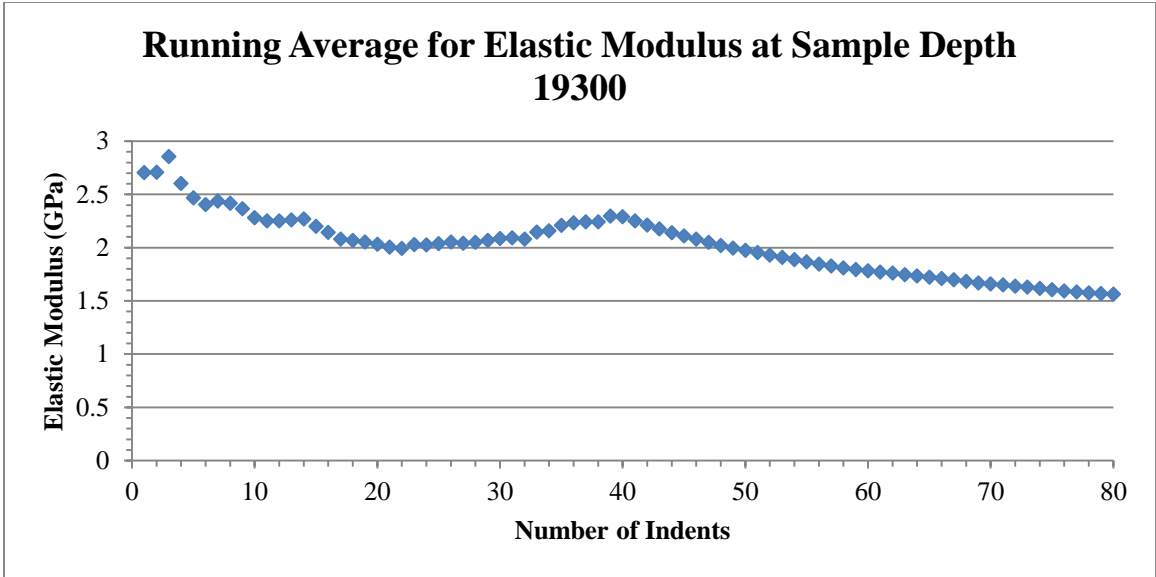
Figure A. 11: Running average for elastic moduli at measured depth 19300.
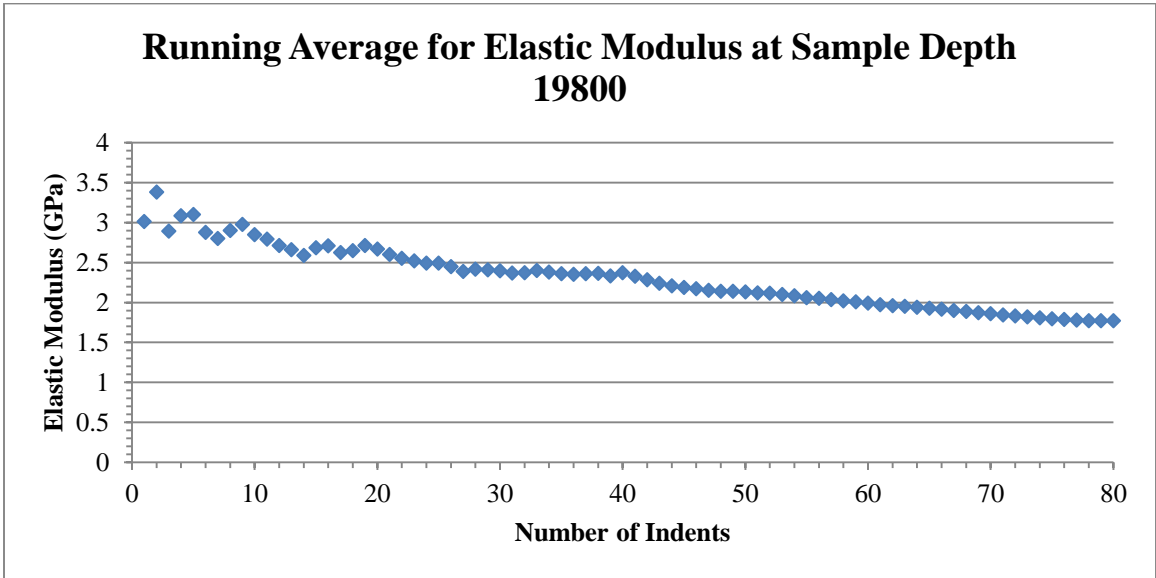
Figure A. 12: Running average for elastic moduli at measured depth 19800.
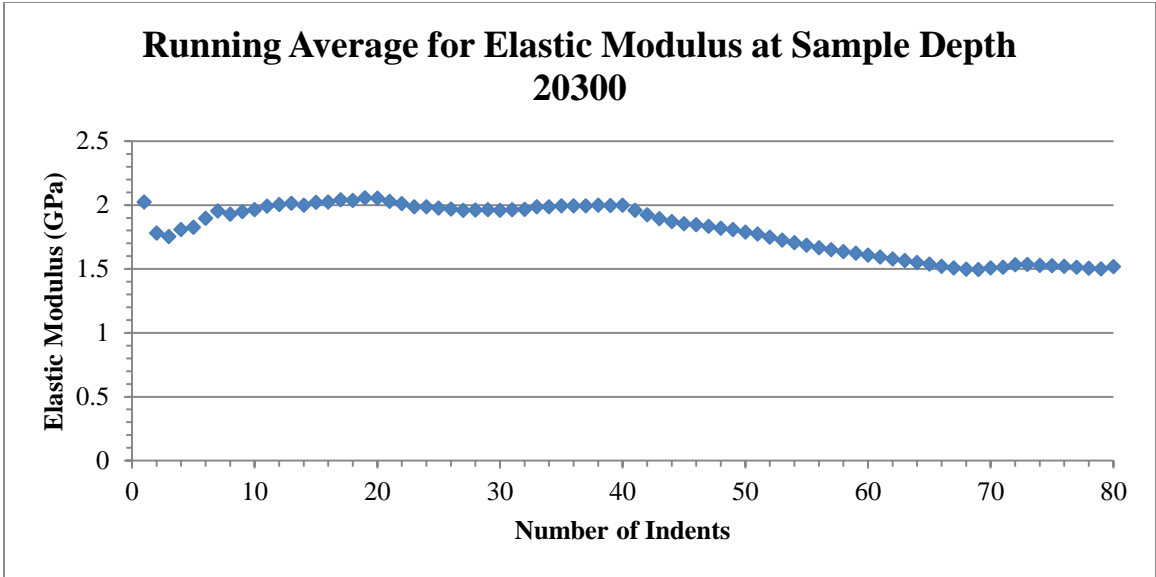
Figure A. 13: Running average for elastic moduli at measured depth 20300.
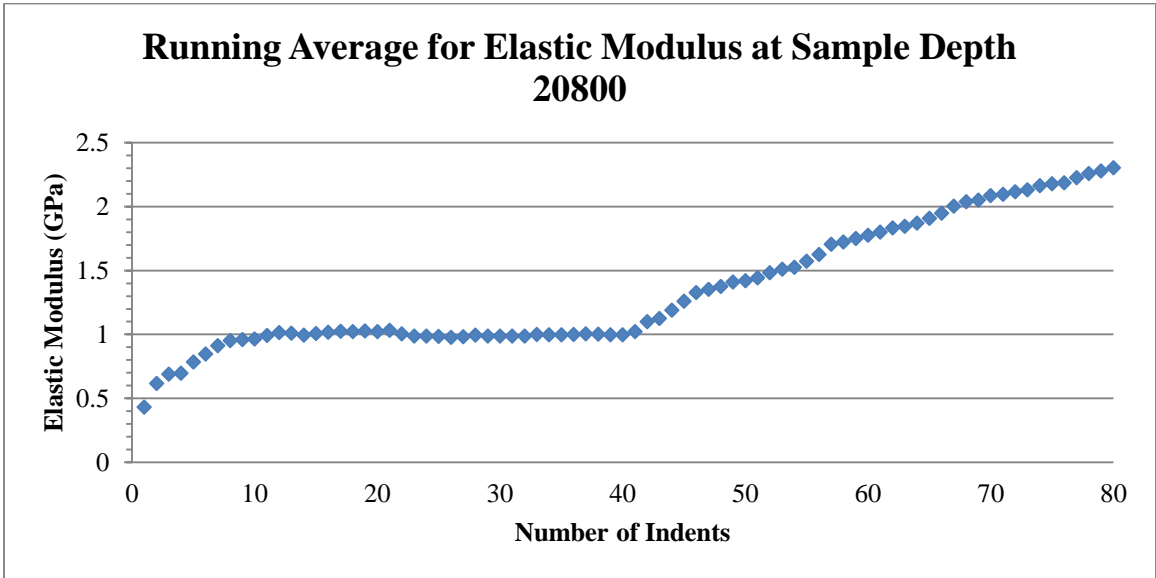
Figure A. 14: Running average for elastic moduli at measured depth 20800.
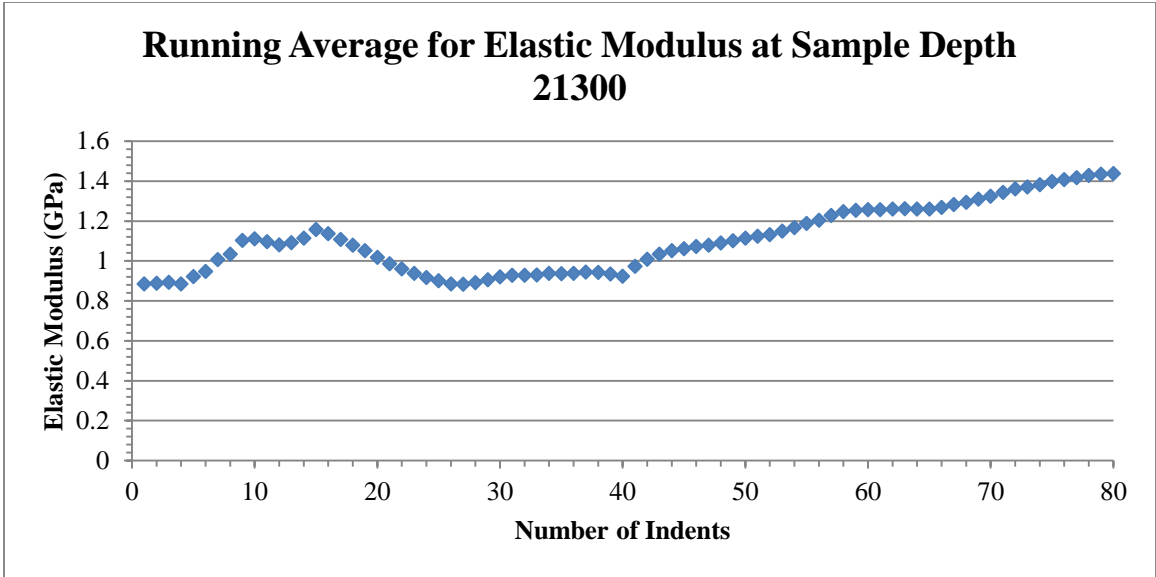
Figure A. 15: Running average for elastic moduli at measured depth 21300.
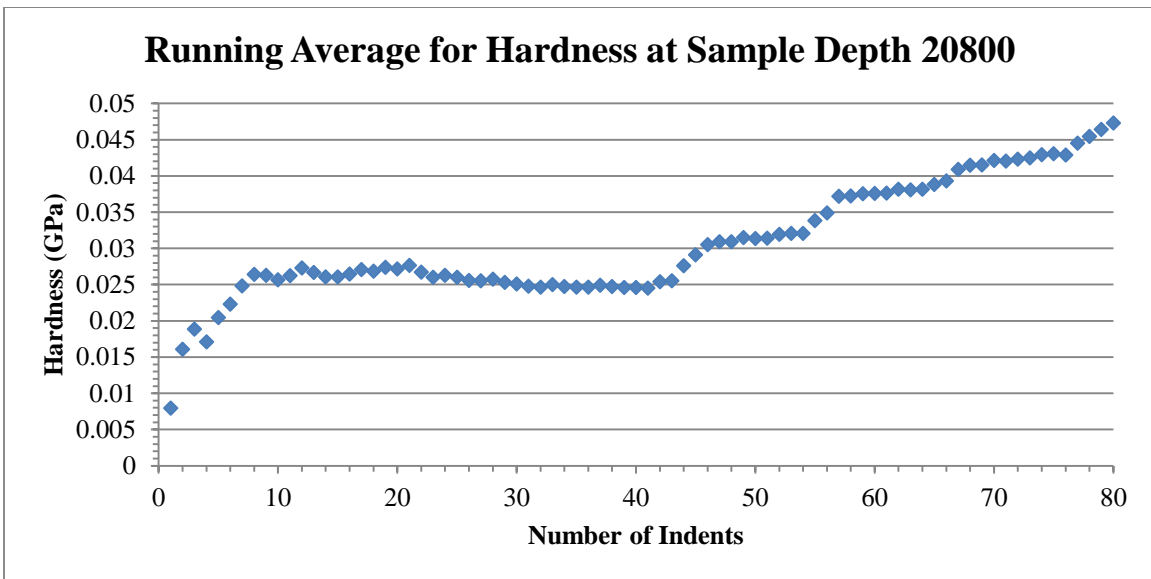
B. Running Average of Hardness Values
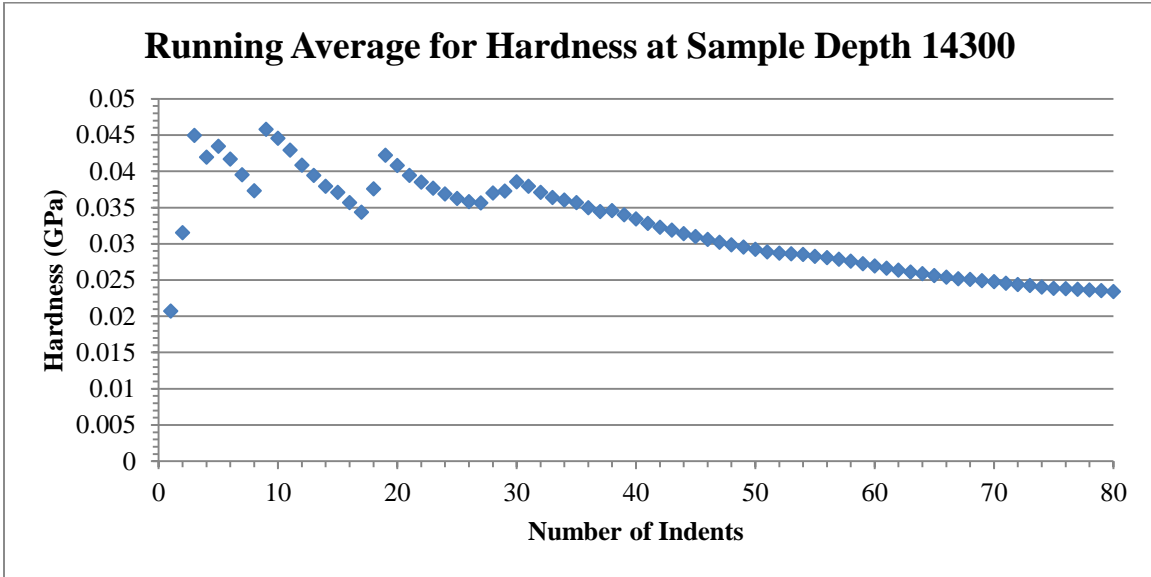
Figure B. 1: Running average for hardness at measured depth 14300.
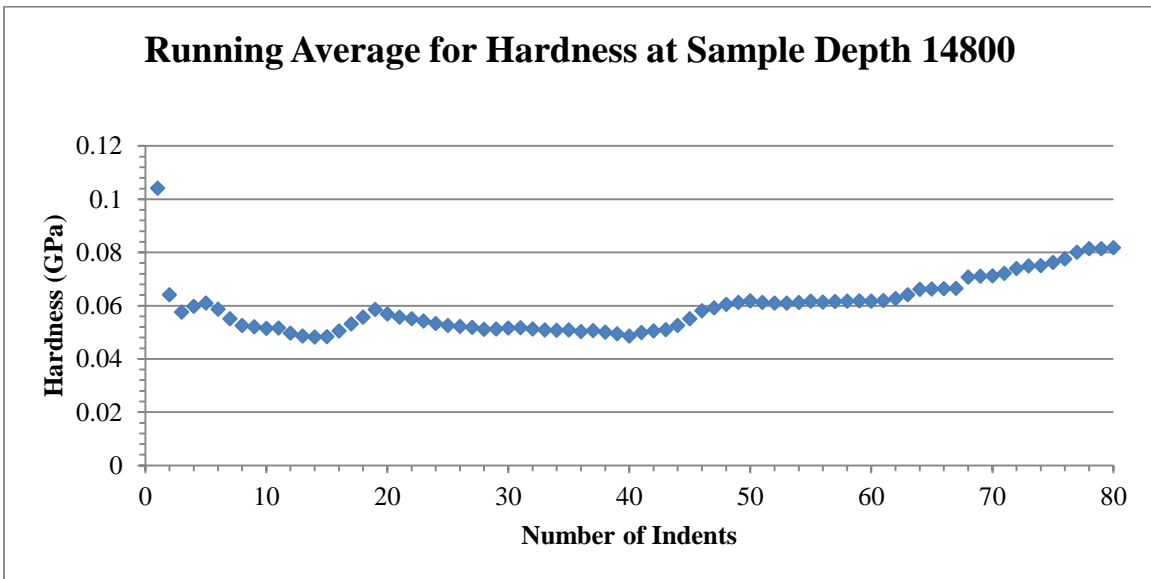
Figure B. 2: Running average for hardness at measured depth 14800.
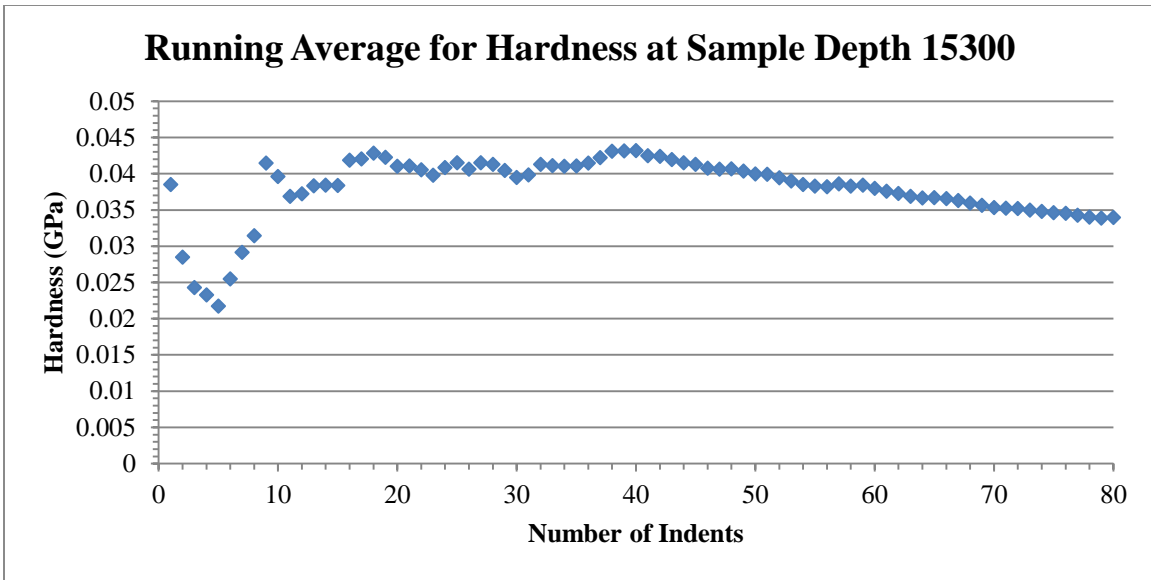
Figure B. 3: Running average for hardness at measured depth 15300.
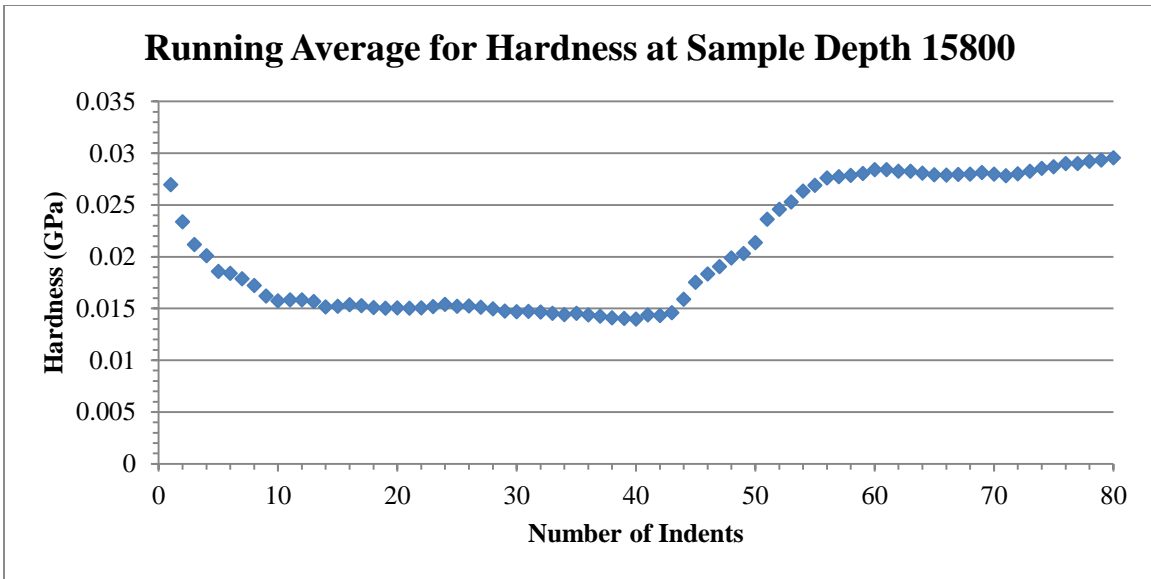
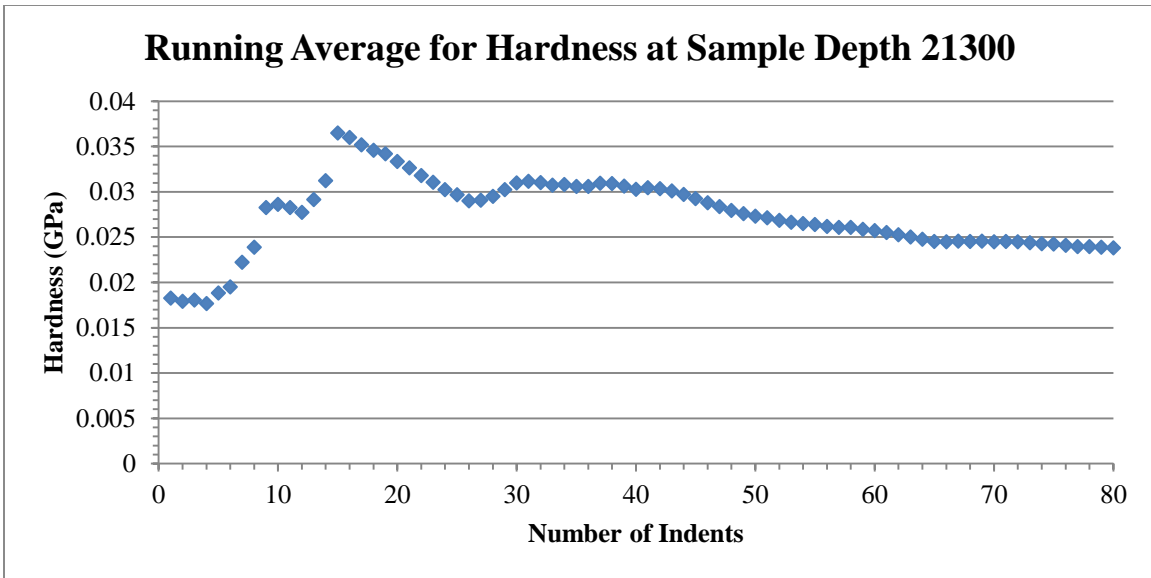**Figure B. 4:** Running average for hardness at measured depth 15800.
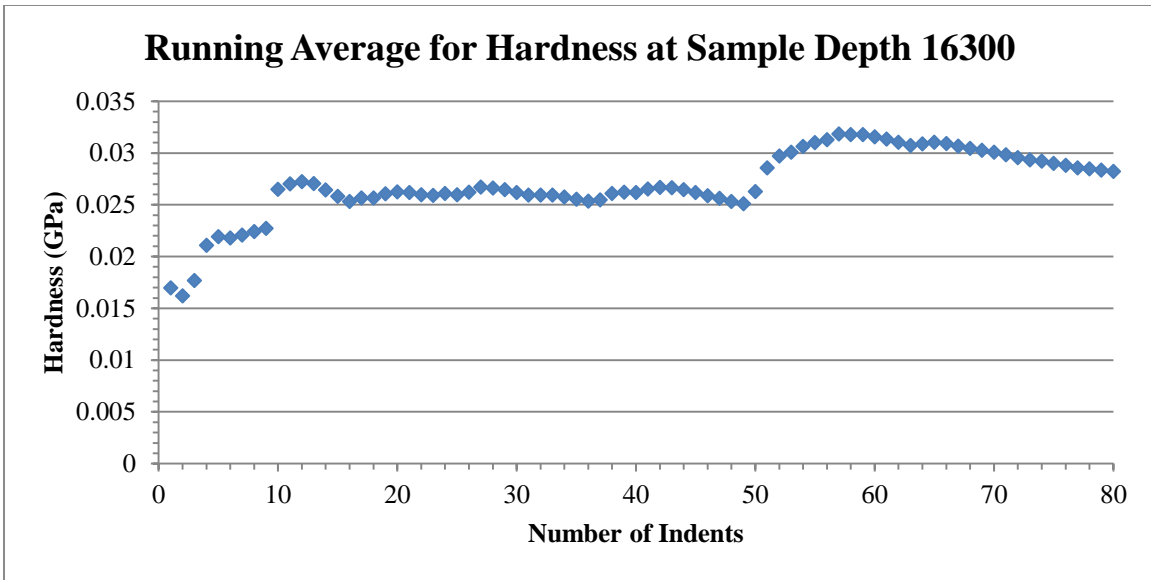
Figure B. 5: Running average for hardness at measured depth 16300.
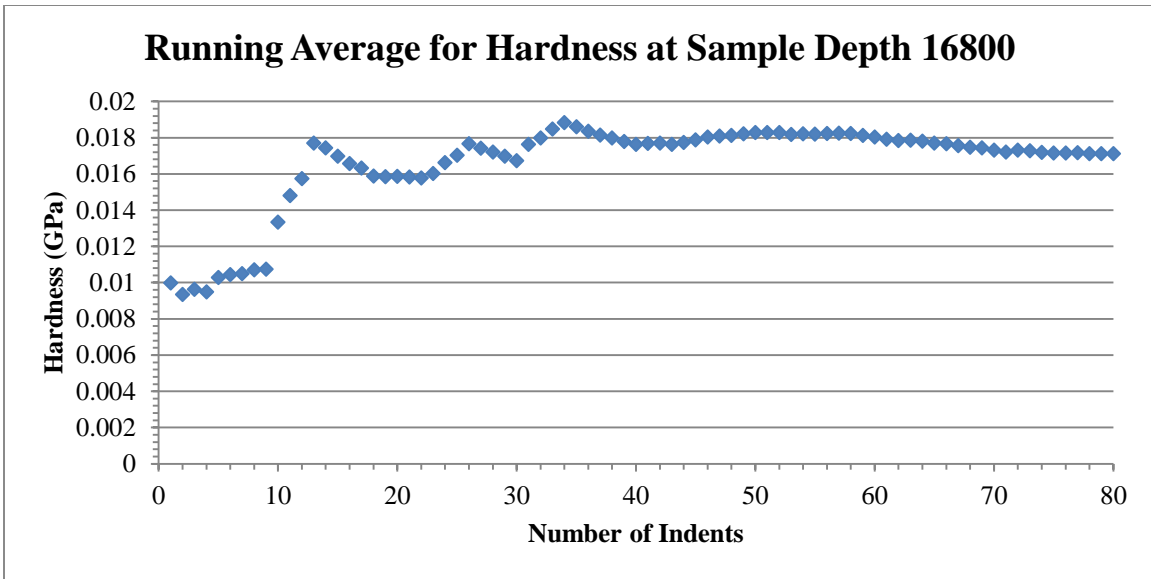
Figure B. 6: Running average for hardness at measured depth 16800.
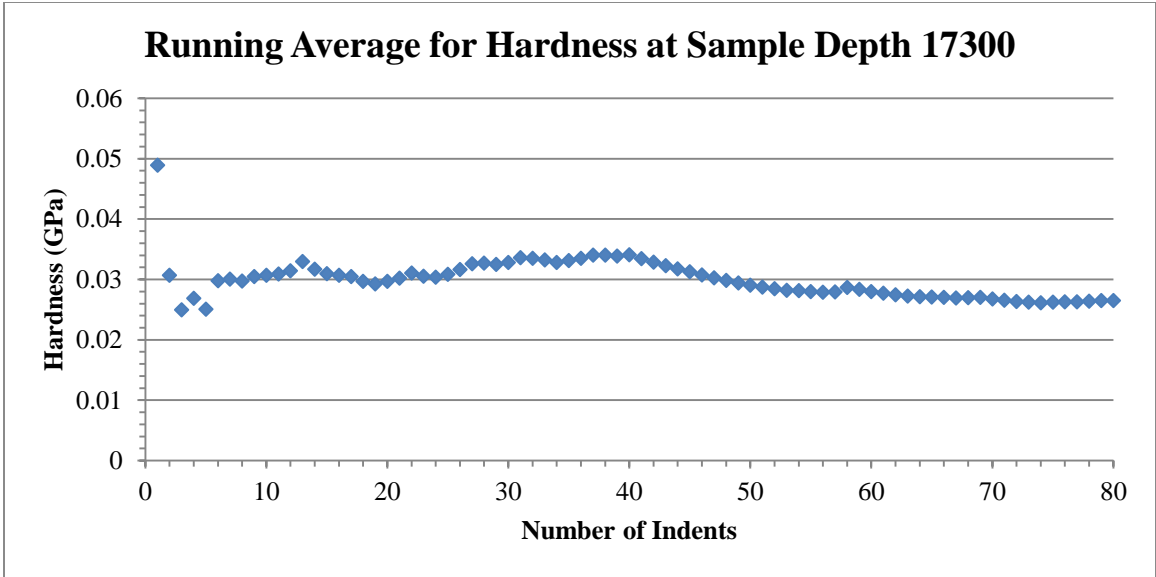
Figure B. 7: Running average for hardness at measured depth 17300.
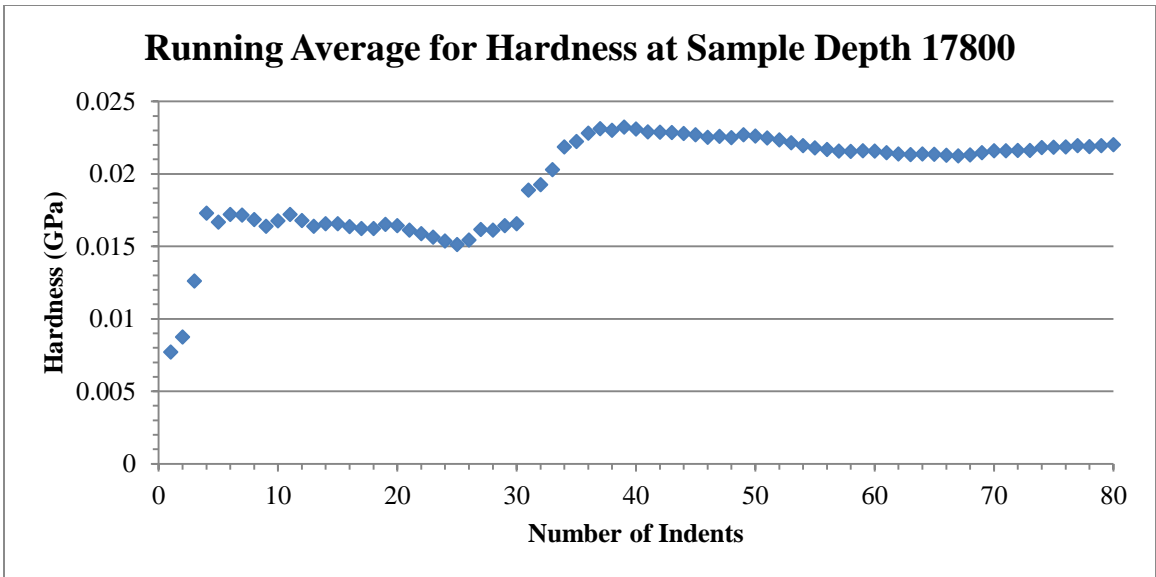
Figure B. 8: Running average for hardness at measured depth 17800.
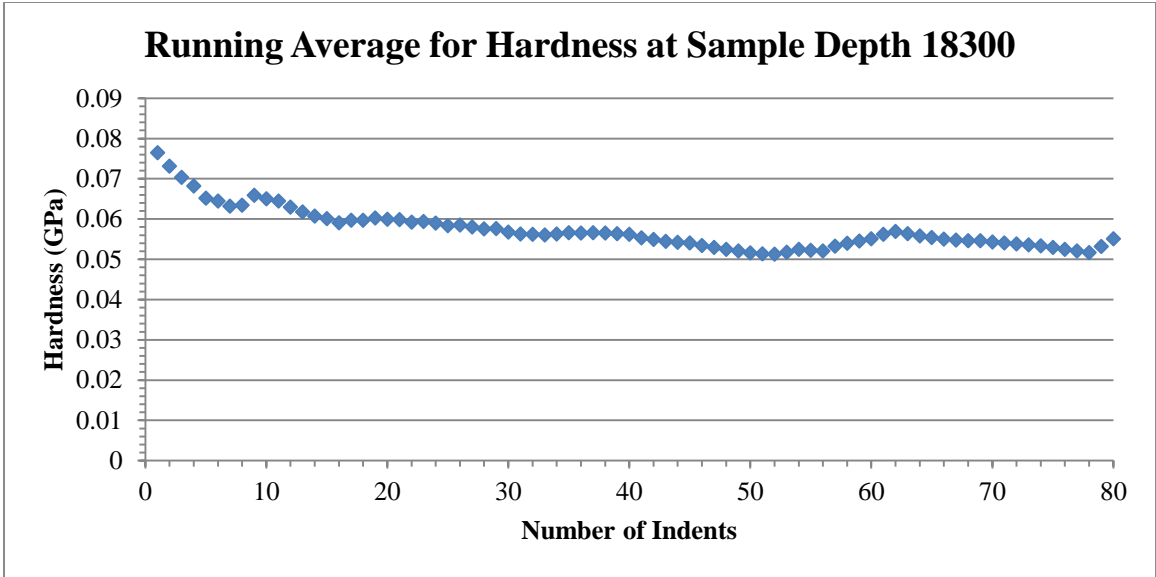
Figure B. 9: Running average for hardness at measured depth 18300.
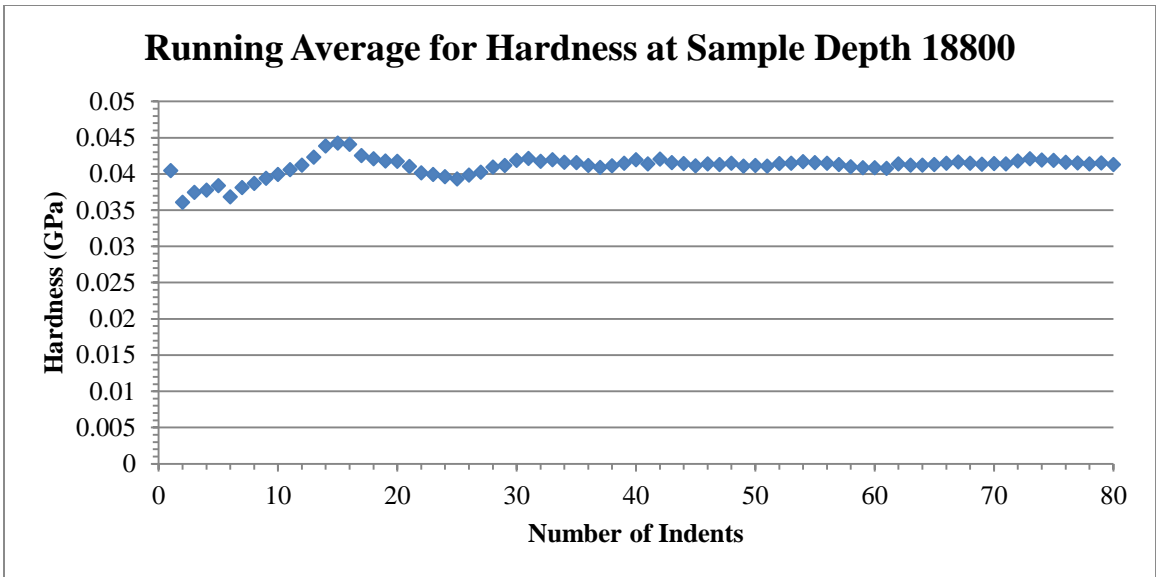
Figure B. 10: Running average for hardness at measured depth 18800.
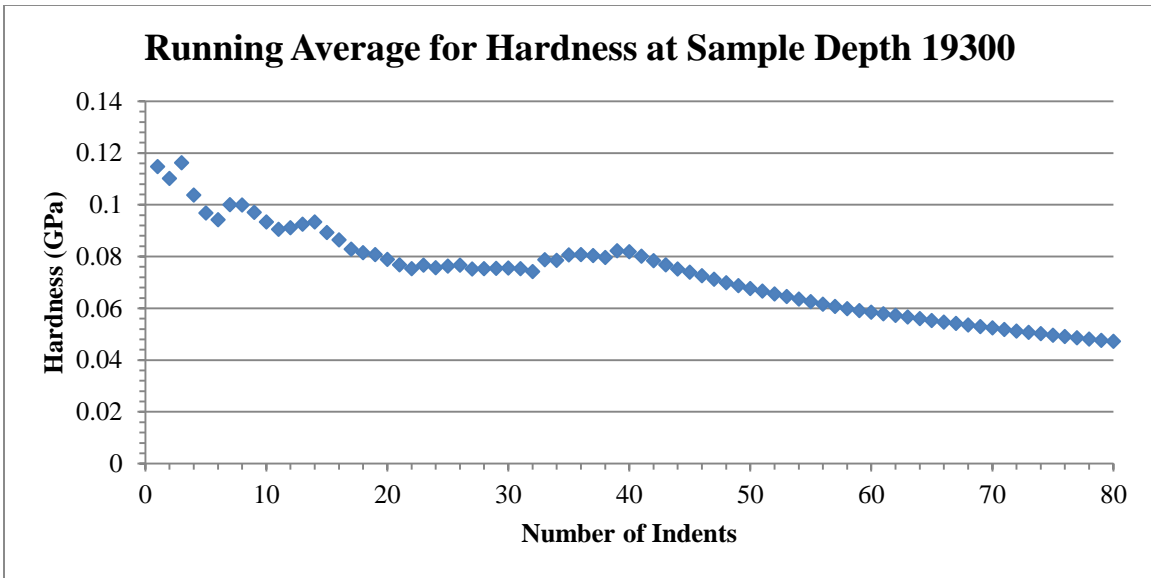
Figure B. 11: Running average for hardness at measured depth 19300.
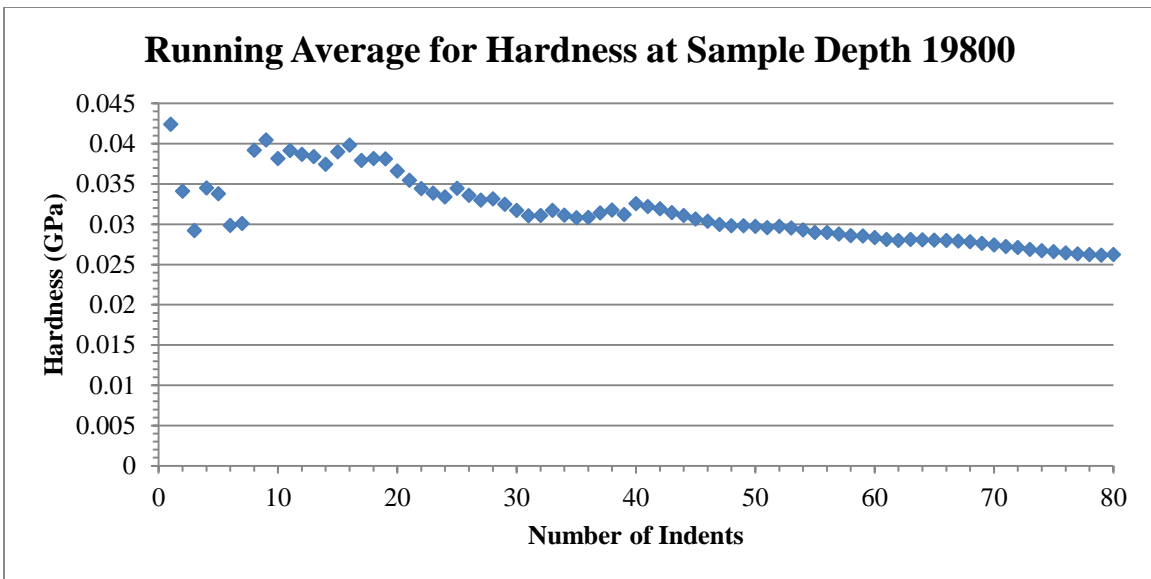
Figure B. 12: Running average for hardness at measured depth 19800.
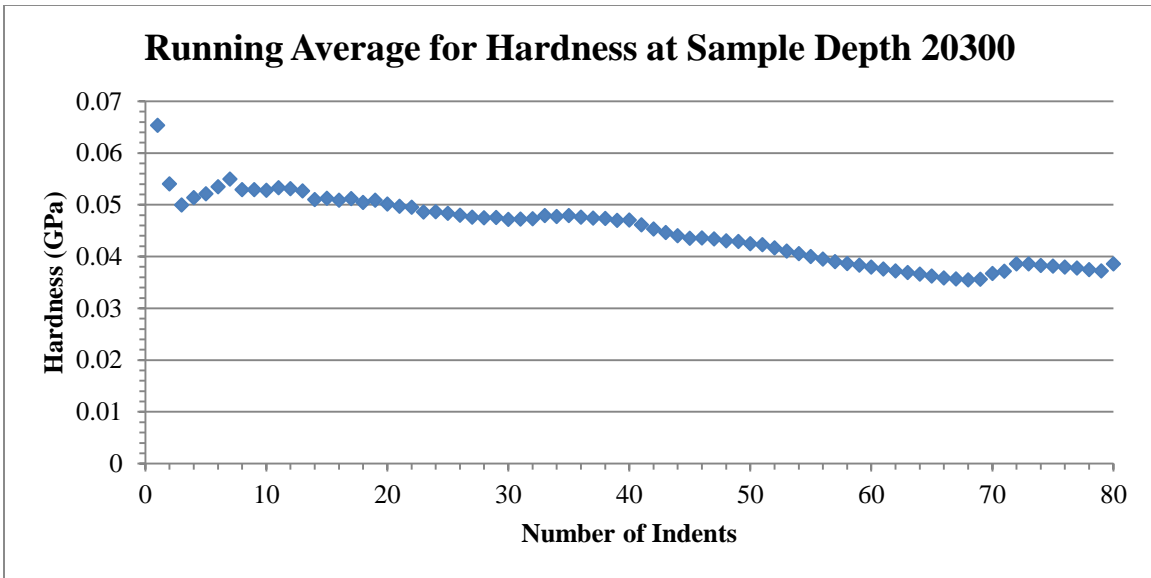
Figure B. 13: Running average for hardness at measured depth 20300.

Figure B. 14: Running average for hardness at measured depth 20800.

Figure B. 15: Running average for hardness at measured depth 21300.

C. Thermogravimetric Analysis Percent Weight Fraction Plots
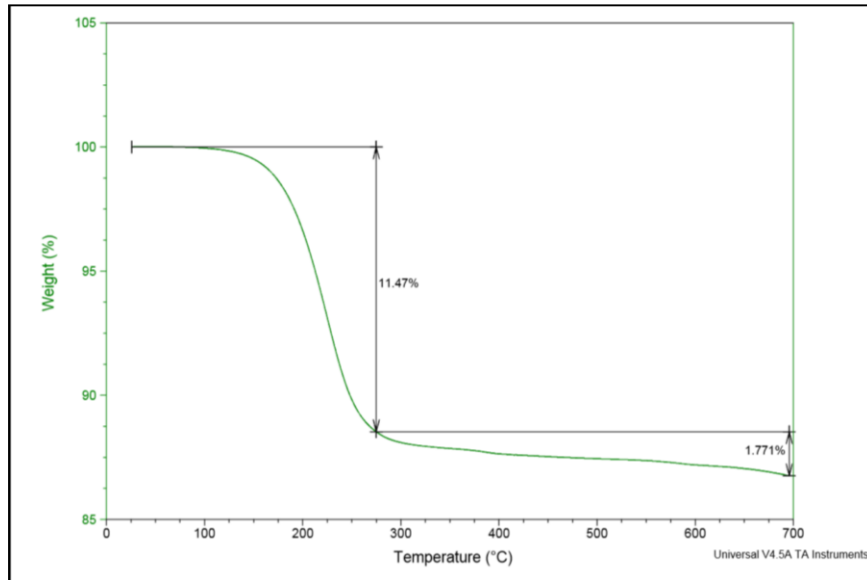
Figure C. 1: TGA results with fraction weight percentages. Measured depth 14300 retested after

48 hour soak in mineral oil.
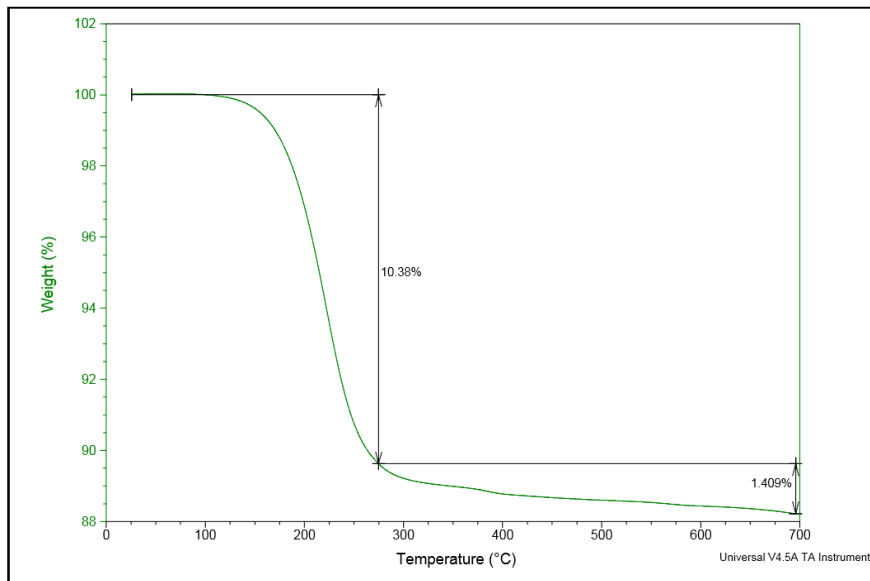
Figure C. 2: TGA results with fraction weight percentages. Measured depth 14300 retested after
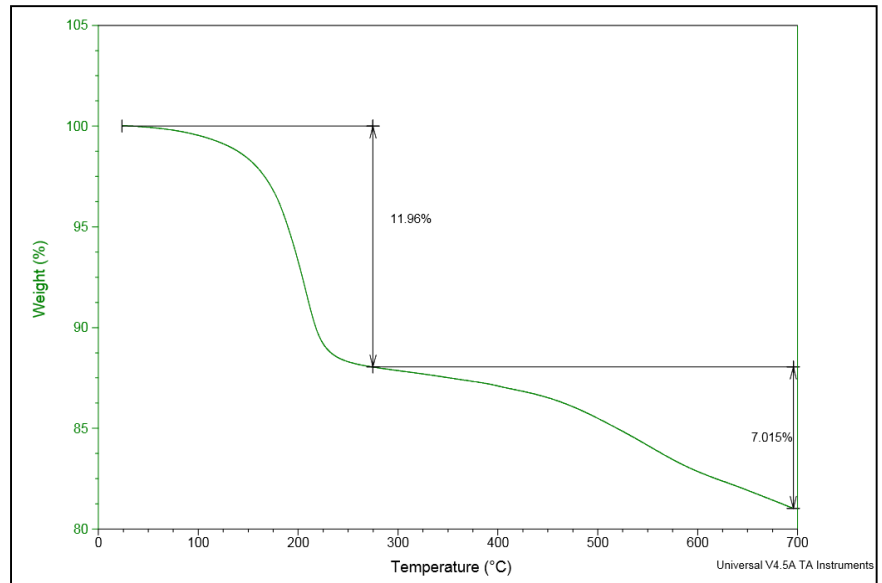
one week soak in mineral oil.
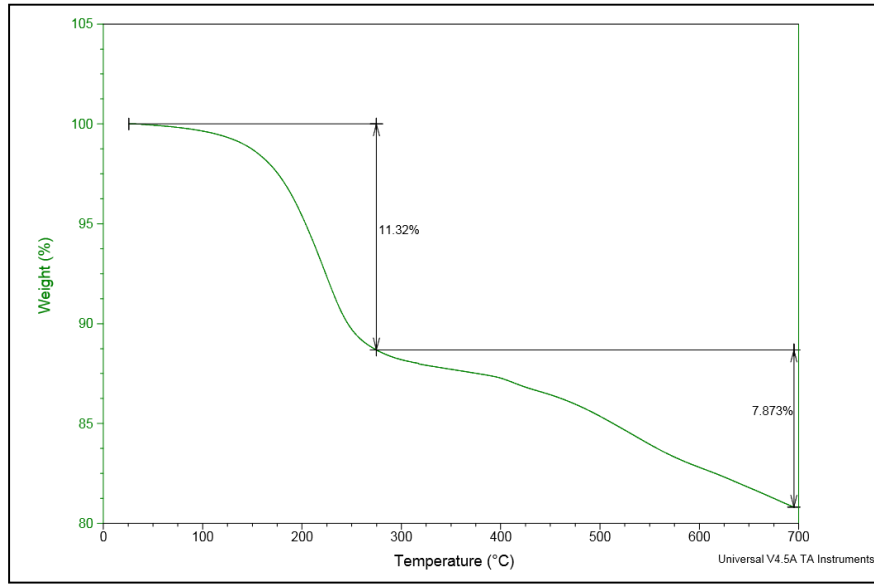
Figure C. 3: TGA results with fraction weight percentages for measured depth 14300 ft.
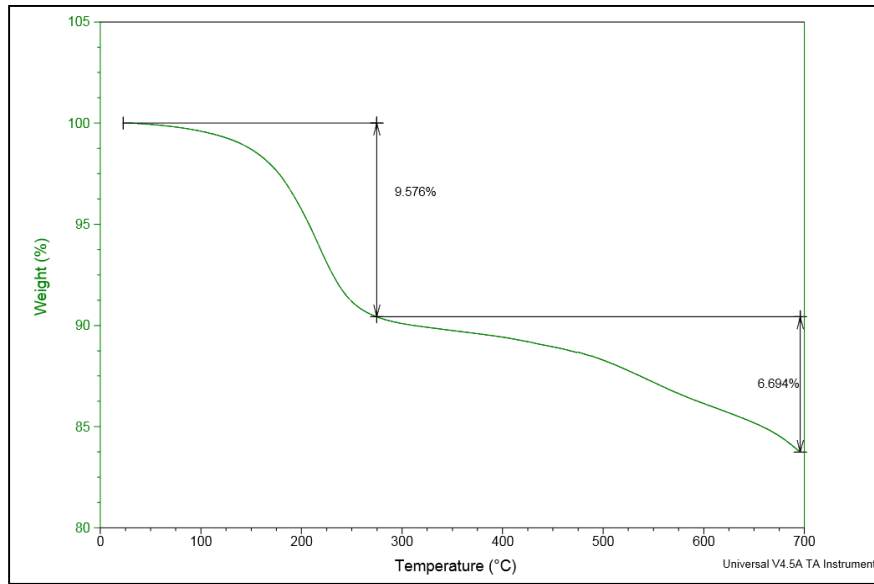
Figure C. 4: TGA results with fraction weight percentages for measured depth 14800 ft.
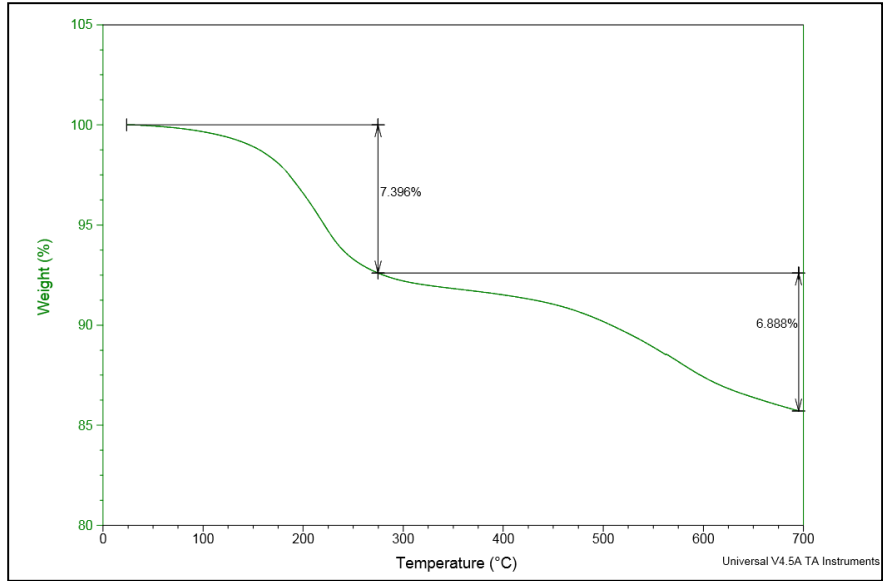
Figure C. 5: TGA results with fraction weight percentages for measured depth 15300 ft.

Figure C. 6: TGA results with fraction weight percentages for measured depth 15800 ft.
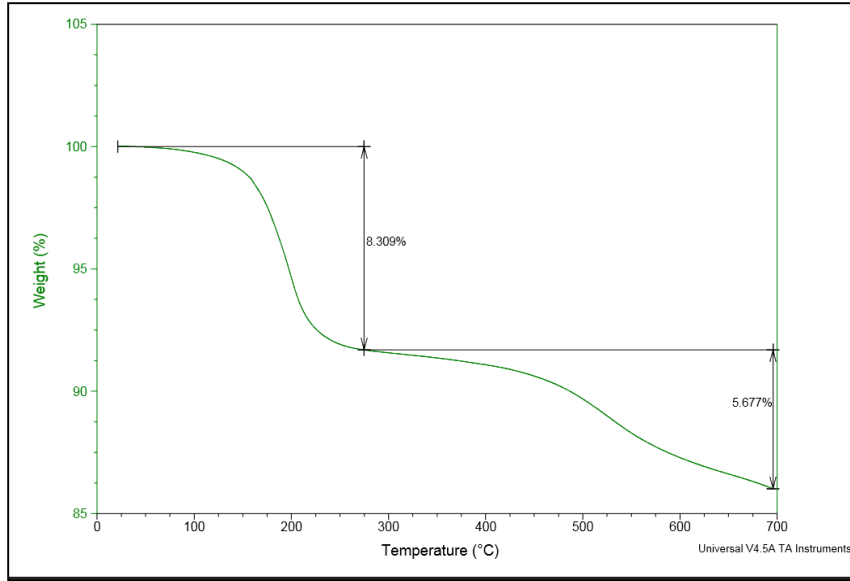
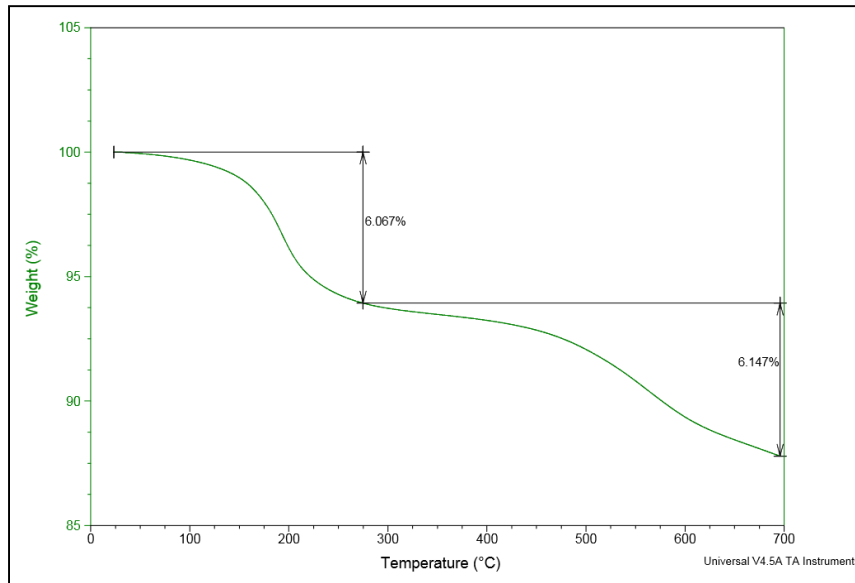**Figure C. 7:** TGA results with fraction weight percentages for measured depth 16300 ft.

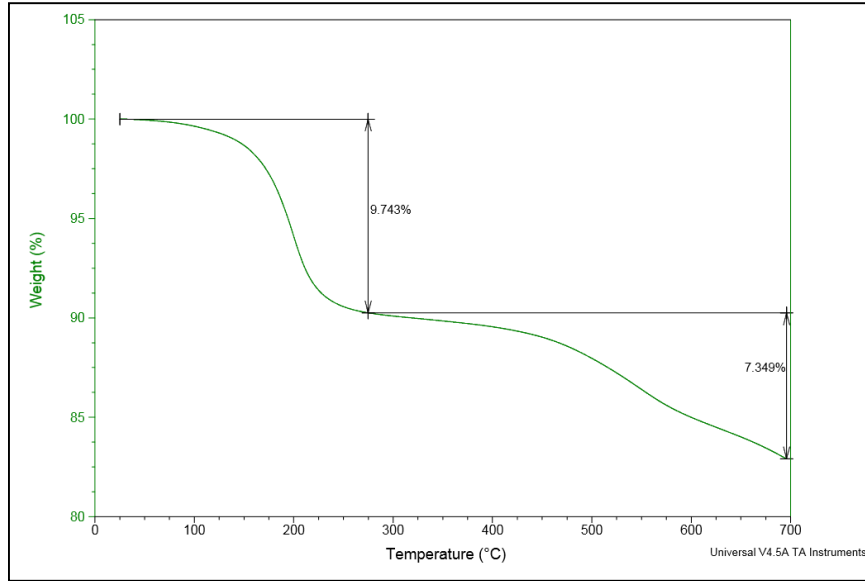**Figure C. 8:** TGA results with fraction weight percentages for measured depth 16800 ft.

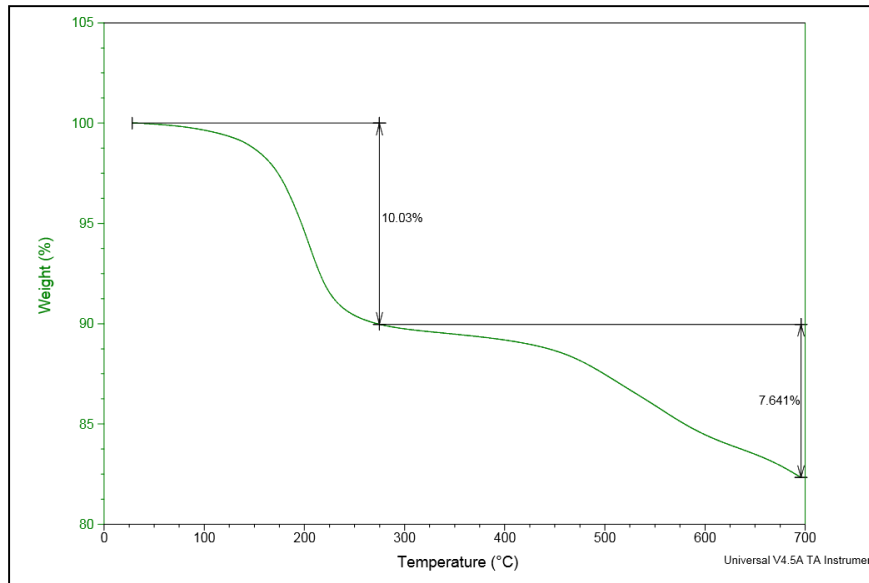**Figure C. 9:** TGA results with fraction weight percentages for measured depth 17300 ft.

Figure C. 10: TGA results with fraction weight percentages for measured depth 17800 ft.
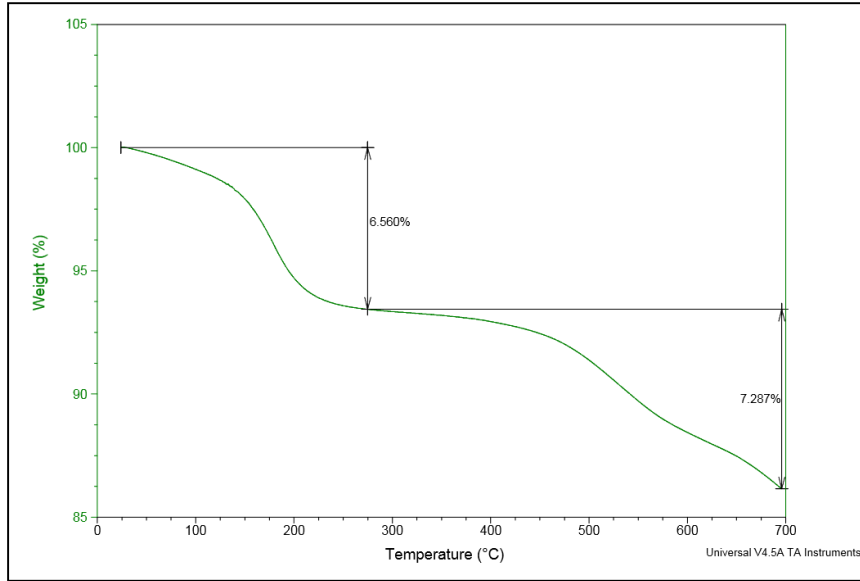
Figure C. 11: TGA results with fraction weight percentages for measured depth 18300 ft.
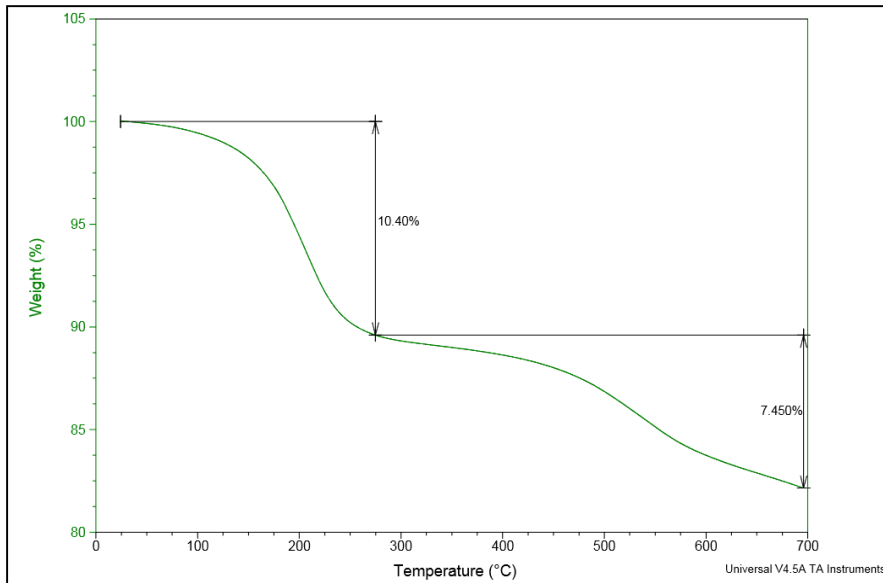

Figure C. 12: TGA results with fraction weight percentages for measured depth 18800 ft.
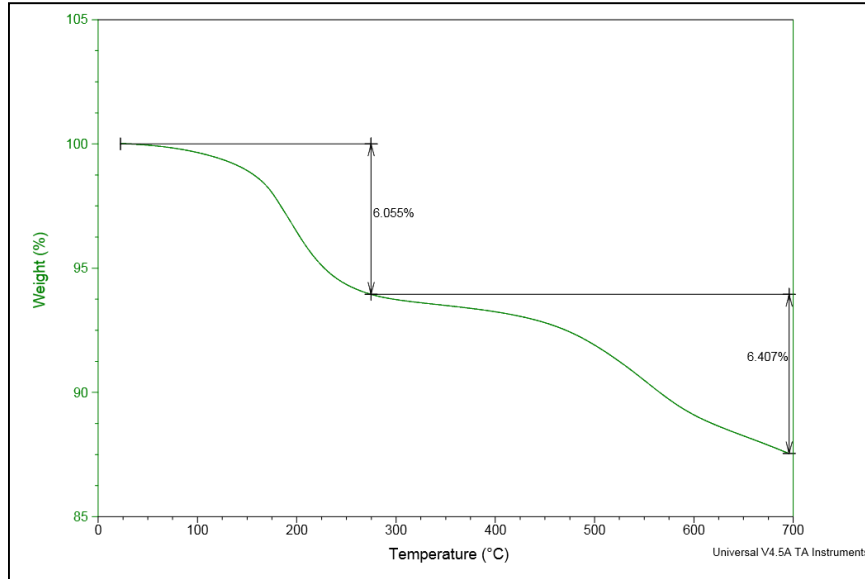
Figure C. 13: TGA results with fraction weight percentages for measured depth 19300 ft.
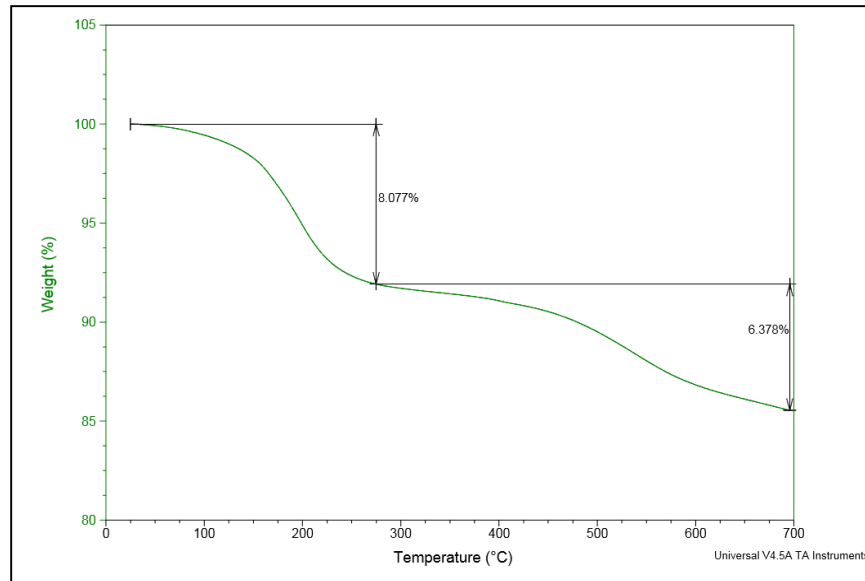

Figure C. 14: TGA results with fraction weight percentages for measured depth 19800 ft.
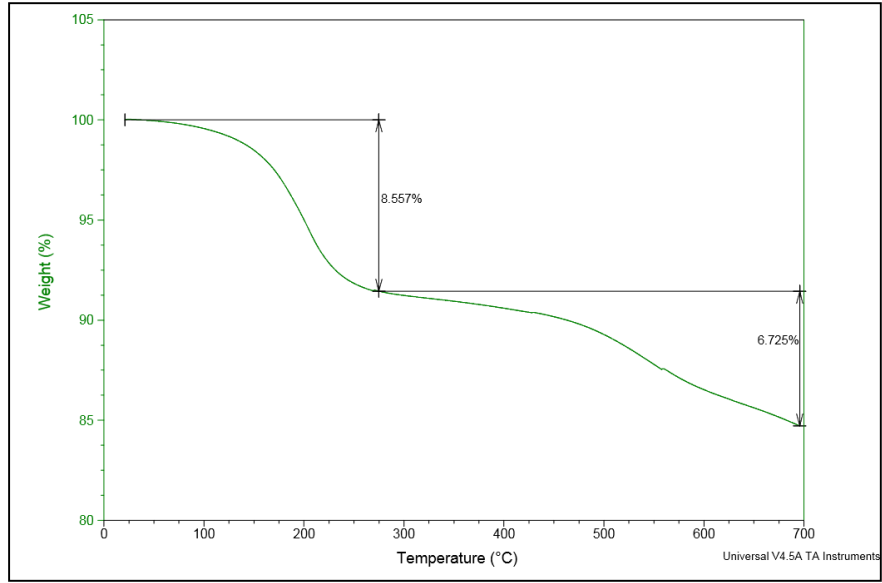
Figure C. 15: TGA results with fraction weight percentages for measured depth 21300 ft.

<div align="center">**VITA**</div>

Zachary N. Miller, E.I.

Education
- University of Mississippi, *M.S. in Engineering Science,* May 2016
    Thesis: Multi-Scale Nanoindentation for Characterization of Oil Shales
-University of Mississippi, *Bachelor of Science in Civil Engineering,* December 2014

Work Experience

-Graduate Research:

-January 2015 – May 2016	Position: Graduate Assistant Researcher
Nano-Infrastructure	Thesis: Multi-scale Nanoindentation for
Dr. Ahmed Al-Ostaz	Characterization of Oil Shales

-Undergraduate Research:

-August 2013 – December 2014	Position: Ballistics Assistant
Nano-Infrastructure	Duties: Create and test epoxy-resin coatings to
Dr. Ahmed Al-Ostaz	protect materials from blast impact
Dr. Hunain Alkhateb	

-CE 207 Laboratory (Surveying): Teaching Assistant (2014-2016)

-Cajun Constructors (*2010-2014)*:

- June 2014- August 2014	Position: Carpenter
Florida Ave Canal	Duties: General Carpenter Duties; Install and check
concrete New Orleans, LA	formwork for canal rebuild

- December 2013 – January 2014	Position: Quality Assurance
SPR DEGAS Relocation	Duties: Assisted lead Q.C. building turnover
Hackberry, LA	packages, built progress tracking
	spreadsheets

Affiliations/Activities
American Society of Civil Engineers – President Ole Miss Chapter: April 2014- April 2015
                        – V.P. Ole Miss Chapter: April 2013- April 2014
Engineers Without Borders – Ole Miss Chapter (2011- 2016)
Institute of Transportation Engineers – Ole Miss Chapter (2013- 2016)